

Resonances in fluid-filled cracks of complex geometry and application to very long period (VLP) seismic signals at Mayotte submarine volcano

Chao Liang¹, Junjun Peng¹, Jean-Paul Ampuero², Nathan Shauer³, and Kaoshan Dai¹

¹Institute for Disaster Management and Reconstruction (IDMR), Sichuan University

²Institut de Recherche pour le Développement

³LabMeC-FECFAU-State University of Campinas

September 13, 2023

Abstract

Fluid-filled cracks sustain a slow guided wave (Krauklis wave or crack wave) whose resonant frequencies are widely used for interpreting long period (LP) and very long period (VLP) seismic signals at active volcanoes. Significant efforts have been made to model this process using analytical developments along an infinite crack or numerical methods on simple crack geometries. In this work, we develop an efficient hybrid numerical method for computing resonant frequencies of complex-shaped fluid-filled cracks and networks of cracks and apply it to explain the ratio of spectral peaks in the VLP signals from the Fani Maoré submarine volcano that formed in Mayotte in 2018. By coupling triangular boundary elements and the finite volume method, we successfully handle complex geometries and achieve computational efficiency by discretizing solely the crack surfaces. The resonant frequencies are directly determined through eigenvalue analysis. After proper verification, we systematically analyze the resonant frequencies of rectangular and elliptical cracks, quantifying the effect of aspect ratio and crack stiffness ratio. We then discuss theoretically the contribution of fluid viscosity and seismic radiation to energy dissipation. Finally, we obtain a crack geometry that successfully explains the characteristic ratio between the first two modes of the VLP seismic signals from the Fani Maoré submarine volcano in Mayotte. Our work not only reveals rich eigenmodes in complex-shaped cracks but also contributes to illuminating the subsurface plumbing system of active volcanoes. The developed model is readily applicable to crack wave resonances in other geological settings, such as glacier hydrology and hydrocarbon reservoirs.

Hosted file

973796_0_supp_11373799_s0ccsg.docx available at <https://authorea.com/users/548660/articles/666006-resonances-in-fluid-filled-cracks-of-complex-geometry-and-application-to-very-long-period-vlp-seismic-signals-at-mayotte-submarine-volcano>

1 **Resonances in fluid-filled cracks of complex geometry**
2 **and application to very long period (VLP) seismic**
3 **signals at Mayotte submarine volcano**

4 **Chao Liang**¹, **Junjun Peng**¹, **Jean-Paul Ampuero**², **Nathan Shauer**³,
5 **Kaoshan Dai**¹

6 ¹Institute for Disaster Management and Reconstruction (IDMR), Sichuan University, 610207, Chengdu,
7 China

8 ²Géoazur, Université Côte d'Azur (UCA), IRD, CNRS, Observatoire de la Côte d'Azur, 06560, Valbonne,
9 France

10 ³LabMeC-FECFAU-State University of Campinas, R. Josiah Willard Gibbs 85, Cidade Universitaria,
11 Campinas, 13083-839, SP, Brazil

12 **Key Points:**

- 13 • Hybrid method combining BEM and FVM efficiently computes resonant frequen-
14 cies of complex-shaped fluid-filled cracks
- 15 • Elliptical crack shares similar modes with rectangular crack but a crack network
16 produces more complex resonances
- 17 • A dumbbell-shaped crack explains ratio of first two modes (~ 2.5) in the VLP seis-
18 mic signal at Mayotte submarine volcano

Corresponding author: Chao Liang, chao.liang@scu.edu.cn

Corresponding author: Kaoshan Dai, kdai@scu.edu.cn

Abstract

Fluid-filled cracks sustain a slow guided wave (Krauklis wave or crack wave) whose resonant frequencies are widely used for interpreting long period (LP) and very long period (VLP) seismic signals at active volcanoes. Significant efforts have been made to model this process using analytical developments along an infinite crack or numerical methods on simple crack geometries. In this work, we develop an efficient hybrid numerical method for computing resonant frequencies of complex-shaped fluid-filled cracks and networks of cracks and apply it to explain the ratio of spectral peaks in the VLP signals from the Fani Maoré submarine volcano that formed in Mayotte in 2018. By coupling triangular boundary elements and the finite volume method, we successfully handle complex geometries and achieve computational efficiency by discretizing solely the crack surfaces. The resonant frequencies are directly determined through eigenvalue analysis. After proper verification, we systematically analyze the resonant frequencies of rectangular and elliptical cracks, quantifying the effect of aspect ratio and crack stiffness ratio. We then discuss theoretically the contribution of fluid viscosity and seismic radiation to energy dissipation. Finally, we obtain a crack geometry that successfully explains the characteristic ratio between the first two modes of the VLP seismic signals from the Fani Maoré submarine volcano in Mayotte. Our work not only reveals rich eigenmodes in complex-shaped cracks but also contributes to illuminating the subsurface plumbing system of active volcanoes. The developed model is readily applicable to crack wave resonances in other geological settings, such as glacier hydrology and hydrocarbon reservoirs.

1 Introduction

Slow guided waves that propagate along fluid-filled cracks, named crack waves or Krauklis waves, can be used for inferring the geometries of subsurface cracks and the fluid properties in a wide range of geological settings (Krauklis, 1962; Ferrazzini & Aki, 1987; Paillet & White, 1982; B. Chouet, 1986; Korneev, 2008; Tang & Cheng, 1989; Lipovsky & Dunham, 2015). In volcanology, crack wave resonances along magma-filled sills and dikes have been used for interpreting long period (LP, 0.5-2 s) and very long period (VLP, 2 to 100 s) seismic signals at many volcanos, including Mount Redoubt (B. A. Chouet et al., 1994), Aso (Kawakatsu et al., 2000; Niu & Song, 2020), Galeras (Cruz & Chouet, 1997), Asama (Fujita & Ida, 2003), Kusatsi-Shirane (Kumagai et al., 2003; Nakano & Kumagai, 2005), Etna (Lokmer et al., 2008), and Erebus (Aster, 2019). Crack waves (and

51 their induced tube waves in wellbores) are used for diagnosing the fracture geometries
 52 in unconventional hydrocarbon reservoirs (Henry et al., 2002; Tary et al., 2014; Lipovsky
 53 & Dunham, 2015; Liang et al., 2017). The resonating or humming signals in glaciers have
 54 also been attributed to crack waves (Métaxian et al., 2003; Stuart et al., 2005; Gräff et
 55 al., 2019; McQuillan & Karlstrom, 2021). Natural cracks in the subsurface are complex
 56 in shape and usually form an inter-connected network. Therefore, efficient methods for
 57 computing resonant modes of single cracks and networks of cracks are necessary for in-
 58 terpreting frequencies measured in the field.

59 Since its first discovery by Krauklis (1962), crack waves have been studied analytically
 60 (Aki et al., 1977; Ferrazzini & Aki, 1987; Korneev, 2008; Lipovsky & Dunham, 2015),
 61 experimentally (Tang & Cheng, 1988; Nakagawa et al., 2016; Cao et al., 2021), and nu-
 62 merically by various methods (e.g., B. Chouet, 1986; Yamamoto & Kawakatsu, 2008;
 63 Frehner & Schmalholz, 2010; O’Reilly et al., 2017; Liang et al., 2020; Shauer et al., 2021;
 64 Jin et al., 2022). Analytically derived dispersion relations are useful for understanding
 65 the propagation behavior but are meant for an infinitely long crack and do not account
 66 for the restriction of the finite crack tip. The finite difference method (FDM) is normally
 67 based on cartesian grids in 2D (Fehler & Aki, 1978) or 3D (B. Chouet, 1986; Liang et
 68 al., 2020) and limited to a tabular crack shape. Maeda and Kumagai (2013) and Maeda
 69 and Kumagai (2017) performed a large number of numerical simulations on rectangu-
 70 lar cracks using a FDM simulator developed by B. Chouet (1986). With that, they ob-
 71 tained a set of empirical fitting formulas for resonant frequencies given the crack aspect
 72 ratio α and stiffness ratio $C_L = K_f L / (G w_0)$, where K_f is the fluid bulk modulus, G
 73 the solid shear modulus, L the crack length and w_0 the crack aperture. However, such
 74 relations only apply to longitudinal or transverse modes on rectangular cracks (Maeda
 75 & Kumagai, 2013, 2017). Notably, O’Reilly et al. (2017) simulated a non-planar fluid-
 76 filled crack using FDM on a curvilinear grid and adopted a lubrication-type approxima-
 77 tion in the fluid (Lipovsky & Dunham, 2015), neglecting fluid acoustics in the crack width
 78 direction while resolving the narrow viscous boundary layer close to the crack wall. This
 79 treatment removes the time step restriction introduced by extremely fine mesh size in
 80 the crack width direction and accelerates the computation. However, their work was lim-
 81 ited to 2D geometries. The finite element method (FEM) is more flexible for handling
 82 complex crack geometries and has been used to study crack waves in 2D (Frehner & Schmal-
 83 holz, 2010; Frehner, 2013) and 3D (Shauer et al., 2021). Particularly, Shauer et al. (2021)

84 produced the first simulation of an elliptical fluid-filled crack using the generalized finite
85 element method (GFEM). However, similar to FDM, FEM needs to discretize the vol-
86 ume, which results in a large number of elements and high computational cost. On the
87 other hand, the boundary element method (BEM) reduces the simulation space from a
88 domain to boundary surfaces, drastically decreasing the number of degrees of freedom,
89 and has been used to study waves in fluid-filled cracks (Yamamoto & Kawakatsu, 2008;
90 Pointer et al., 1998; Jin et al., 2022) and other inclusions (Zheng et al., 2016; Sun et al.,
91 2020). However, previous BEM simulations are either in two dimensions or focus on the
92 wave diffraction instead of analyzing the resonant frequencies. Currently, the study of
93 resonant frequencies of complex-shaped fluid-filled cracks and crack networks in three
94 dimensions remain unknown.

95 In this work, we propose an efficient hybrid numerical method to simulate crack
96 wave resonance in complex-shaped cracks or crack networks filled with an inviscid fluid,
97 by coupling the boundary element method (BEM) for the solid response and the finite
98 volume method (FVM) for acoustics in the fluid. By using triangular elements in both
99 BEM and FVM on the crack surfaces, we successfully handle complex crack shapes and
100 intersections. We restrict our attention to the low frequency limit where the crack wave
101 is much slower than the solid body waves, such that the solid response can be approx-
102 imated as quasi-static (Korneev, 2008; Lipovsky & Dunham, 2015; Liang et al., 2020).
103 An eigenvalue analysis is performed to extract the resonant modes directly in the fre-
104 quency domain, circumventing errors from time discretization and spectral analysis of
105 the time domain simulation data. We first verify our method by comparing results with
106 analytical solutions in the rigid wall limit and with numerical solutions from existing meth-
107 ods for both a rectangular (B. Chouet, 1986; Maeda & Kumagai, 2017) and elliptical cracks
108 (Shauer et al., 2021). An example is then provided to demonstrate the simulation ca-
109 pability for intersecting cracks. The effect of crack aspect ratio and stiffness ratio on res-
110 onant frequencies (longitudinal, transverse, and mixed modes) is systematically inves-
111 tigated for both rectangular and elliptical cracks. Although our current model does not
112 include viscous or radiation loss, we provide some theoretical discussion on these effects
113 under simple assumptions (boundary layer limit and quasi-dynamic approximation). Fi-
114 nally, we present a crack shape compatible with the first two spectral peaks of VLP seis-
115 mic signals from the Fani Maoré, Mayotte submarine volcano and discuss the potential
116 of the methodology for future applications in volcanology and other geological settings.

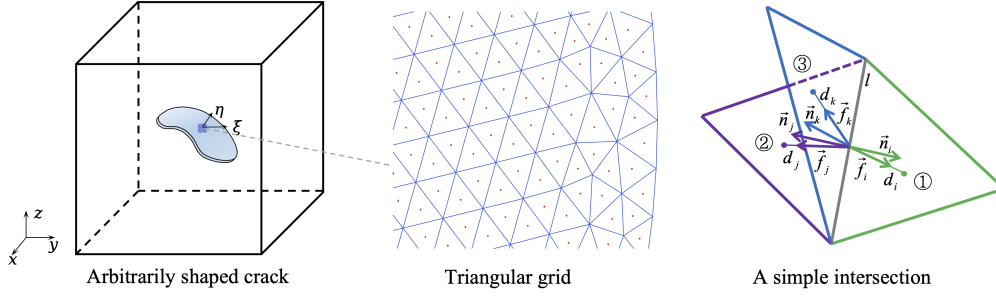


Figure 1. Schematics of an arbitrarily-shaped fluid-filled crack, its spatial discretization (with unknown variables placed in the element centroids, red dots), and a zoom-in view at an intersection between two cracks.

2 Methods

In this section, we present the governing equations, discretization, and eigenmode analysis for computing the resonant frequencies.

2.1 Governing equations

We consider the oscillation of inviscid fluids in complex-shaped thin cracks embedded in a 3D homogeneous linear elastic solid (Figure 1). The initial opening of the crack is w_0 , which is assumed to be a constant and much smaller than the wavelength λ . We adopt a similar lubrication approximation as B. Chouet (1986), Yamamoto and Kawakatsu (2008) and O'Reilly et al. (2017), and treat the fluid pressure and velocities as uniform in the crack thickness direction, reducing the crack from a 3D body to a 2D surface S . Following O'Reilly et al. (2017), we consider a small crack curvature so that its effect on the fluid momentum balance is negligible. Thus, the mass and momentum balance of the fluid on the crack surface are written as

$$\frac{1}{w_0} \frac{\partial w}{\partial t} + \frac{1}{K_f} \frac{\partial p}{\partial t} + \frac{\partial v_\xi}{\partial \xi} + \frac{\partial v_\eta}{\partial \eta} = 0, \quad (1)$$

$$\rho_f \frac{\partial v_\xi}{\partial t} + \frac{\partial p}{\partial \xi} = 0, \quad (2)$$

$$\rho_f \frac{\partial v_\eta}{\partial t} + \frac{\partial p}{\partial \eta} = 0, \quad (3)$$

where ρ_f and K_f are fluid density and bulk modulus, w is the crack opening perturbation, p is the fluid pressure perturbation, t is time, and ξ and η are two locally perpen-

134 dicular coordinates tangent to the crack surface, v_ξ and v_η are the fluid velocities in the
 135 ξ and η directions, respectively. Eliminating v_ξ and v_η in (1) using (2)-(3), we have

$$\rho_f \left(\frac{1}{w_0} \frac{\partial^2 w}{\partial t^2} + \frac{1}{K_f} \frac{\partial^2 p}{\partial t^2} \right) - \Delta p = 0, \quad (4)$$

136 where $\Delta = \frac{\partial^2}{\xi^2} + \frac{\partial^2}{\eta^2}$ is the tangential Laplace operator along the crack surface. The
 137 coupling between fluid and solid is encapsulated in the relation between the crack open-
 138 ing perturbation w and pressure perturbation p , which must balance the solid normal
 139 stress perturbation σ_n on the crack wall (assumed positive in compression). Since we fo-
 140 cus on the low frequency limit, the solid response is approximately quasi-static (Korneev,
 141 2008; Lipovsky & Dunham, 2015; Liang et al., 2020), and p for a linear elastic solid can
 142 be expressed as (Segall, 2010):

$$p(x) = \int_S K(x, \xi) w(\xi) dA, \quad (5)$$

143 where $K(x, \xi)$ is the Green's function that relates a unit open dislocation impulse at ξ
 144 to the normal stress change at x . The expressions of K in an elastic whole space and half
 145 space are available analytically for a uniform dislocation on both rectangular elements
 146 (Okada, 1985, 1992) and triangular elements (Nikkhoo & Walter, 2015).

147 2.2 Discretization

148 We discretize the crack surfaces into N_e triangular elements. The unknown aver-
 149 age pressures $\bar{\mathbf{p}}$ and openings $\bar{\mathbf{w}}$, placed at element centroids (as shown in Figure 1), are
 150 related by

$$\bar{\mathbf{p}} = \mathbf{K} \bar{\mathbf{w}}, \quad (6)$$

151 where \mathbf{K} is a N_e by N_e matrix and $K(i, j)$ denotes the fluid pressure (or solid normal
 152 stress) change at the centroid of the i -th element caused by a unit open dislocation on
 153 the j -th element. We use the full space Green's function in this study but one can also
 154 use the half space solution.

155 We then discretize the tangential Laplacian operator by a finite volume scheme with
 156 a two-point flux (TPF) approximation following Karimi-Fard et al. (2004), which has
 157 been widely used for diffusive flows through a discrete fracture network in hydrocarbon
 158 reservoirs (e.g., Li & Lee, 2008; Moinfar et al., 2013; Xu et al., 2017; Berre et al., 2019).
 159 This scheme is only first-order accurate and is thus rarely used in wave propagation prob-
 160 lems due to the strong numerical diffusion in time domain simulations (e.g., Durran, 2013).

161 However, it is a sufficient scheme for our problem as we focus on resolving only the spa-
 162 tial distribution of eigenmodes in the frequency domain and the low order of accuracy
 163 can be remedied by using more elements. Here, we briefly present the key derivation steps
 164 and the readers are referred to Karimi-Fard et al. (2004) for a detailed description.

165 We consider an arbitrary planar triangular element i with a surface S_i and bound-
 166 ary edges l_{ij} , where j is the index of the neighboring elements. Each i and j pair forms
 167 a hydraulic connection. When multiple cracks intersect, multiple connections share the
 168 same edge. We integrate equation (4) over each element i 's surface, leading to:

$$\rho_f A_i \left[\frac{1}{w_0} \frac{\partial^2 \bar{w}_i}{\partial t^2} + \frac{1}{K_f} \frac{\partial^2 \bar{p}_i}{\partial t^2} \right] = \int_{S_i} \Delta p ds, \quad (7)$$

169 where

$$\bar{p}_i = \frac{1}{A_i} \int_{S_i} p ds, \quad (8)$$

170

$$\bar{w}_i = \frac{1}{A_i} \int_{S_i} w ds, \quad (9)$$

171 are the average pressure and opening of element i , respectively. Applying the divergence
 172 theorem to the right hand side of equation (7), we have:

$$\int_{S_i} \Delta p ds = \int_{S_i} \vec{\nabla} \cdot \vec{\nabla} p ds = \int_l \frac{\partial p}{\partial n} dl = - \sum_{j=1}^{n_c} D_{i \rightarrow j} Q_{i \rightarrow j}, \quad (10)$$

173 where $\partial p / \partial n$ is the pressure gradient normal to the boundary edges, n_c is the total num-
 174 ber of connections in contact with element i , $Q_{i \rightarrow j}$ is the flux going out from element
 175 i to element j . Since $Q_{i \rightarrow j} = -Q_{j \rightarrow i}$, we only store $Q_{i \rightarrow j}$ for each (i, j) pair and its
 176 positive flux direction is pre-defined by an indicator function $I_{i \rightarrow j} = -I_{j \rightarrow i} = 1$. $D_{i \rightarrow j}$
 177 is the discrete divergence operator and $D_{i \rightarrow j} = I_{i \rightarrow j} = 1$.

178 The assumption of the TPF scheme is to approximate the flux term in the follow-
 179 ing form (equation (7) in Karimi-Fard et al. (2004)):

$$Q_{i \rightarrow j} = I_{i \rightarrow j} T_{ij} (p_i - p_j), \quad (11)$$

180 where p_i and p_j are pressures defined at the centroids of the two neighboring elements.

181 T_{ij} is the scalar transmissibility and is expressed as

$$T_{ij} = \frac{\alpha_i \alpha_j}{\sum_{k=1}^{n_c} \alpha_k}, \quad (12)$$

182

$$\alpha_k = \frac{l_{ij}}{d_k} \vec{n}_k \cdot \vec{f}_k, \quad (13)$$

183 where l_{ij} is the length of the connecting edge, d_k and \vec{f}_k are the length and unit direc-
 184 tional vector from midpoint of the edge to the centroid of element k , \vec{n}_k is a unit nor-
 185 mal vector perpendicular to the edge and pointing towards element k , as shown in Fig-
 186 ure 1. Fluxes on the crack boundaries are set to zero. Combining equations (10) and (11),
 187 we have:

$$\int_{S_i} \Delta p ds = - \sum_{j=1}^{n_c} D_{i \rightarrow j} I_{i \rightarrow j} T_{ij} (p_i - p_j). \quad (14)$$

188 It is apparent that changing the positive flux direction from $i \rightarrow j$ to $j \rightarrow i$ flips the
 189 sign of both $D_{i \rightarrow j}$ and $I_{i \rightarrow j}$ and thus results in the same Laplacian term. Substituting
 190 equation (14) into equation (7) and rewriting in the matrix form, we have the spatially
 191 discretized equation without external forcing:

$$\rho_f \left(\frac{1}{w_0} \mathbf{K}^{-1} + \frac{1}{K_f} \right) \frac{\partial^2 \bar{\mathbf{p}}}{\partial t^2} = -\mathbf{A}^{-1} \mathbf{D} \mathbf{Q} = -\mathbf{A}^{-1} \mathbf{D} \mathbf{T} \bar{\mathbf{p}}, \quad (15)$$

192 where \mathbf{A} is a diagonal matrix of size N_e by N_e denoting the area of each element, $\mathbf{Q} =$
 193 $\mathbf{T} \bar{\mathbf{p}}$ is the flux vector whose size is the total number of connections N_c , \mathbf{T} is the trans-
 194 missibility matrix (including the indicator function) of size N_c by N_e that maps the vec-
 195 tor $\bar{\mathbf{p}}$ to \mathbf{Q} , and \mathbf{D} is the divergence matrix of size N_e by N_c that maps \mathbf{Q} to the net flux
 196 out of each element. The structure of matrices \mathbf{D} and \mathbf{T} for a system of three intersect-
 197 ing crack elements are described in Appendix A.

198 We further introduce the following dimensionless quantities:

$$\mathbf{K}^* = \mathbf{K}/(G/L), \mathbf{A}^* = \mathbf{A}/L^2, w = w^*/w_0, t^* = t/(L/c_l), \bar{\mathbf{p}}^* = \bar{\mathbf{p}}/(\rho_f c_l^2), \quad (16)$$

199 where G is the solid shear modulus, L is a representative length of the crack and $c_l =$
 200 $\sqrt{Gw_0}/(\rho_f L)$ is a representative crack wave speed. Different non-dimensionalization strate-
 201 gies exist, such as the one by B. Chouet (1986) which normalizes wave speeds by the solid
 202 compressional wave speed c_p . We choose c_l instead, because in the long wavelength limit,
 203 where compliance of the crack dominates, this choice conveniently results in a fundamen-
 204 tal frequency of the order of unity. The nondimensionalised equation is

$$\left(\frac{1}{C_L} \mathbf{I} + (\mathbf{K}^*)^{-1} \right) \frac{\partial^2 \bar{\mathbf{p}}^*}{\partial t^{*2}} = -\mathbf{A}^{*-1} \mathbf{D} \mathbf{T} \bar{\mathbf{p}}^*, \quad (17)$$

205 where $C_L = K_f L / G w_0$ is the key dimensionless parameter, named crack stiffness ra-
 206 tio by B. Chouet (1986). The crack wave limit is achieved with $C_L \gg 1$, where the crack
 207 is much more compliant than the fluid. C_L can be related to the representative crack
 208 wave speed c_l by $C_L = c_f^2 / c_l^2$, where c_f is the fluid acoustic wave speed. The crack topol-

209 ogy (for instance, the aspect ratio α for a rectangular or elliptical crack) and solid Pois-
 210 son's ratio ν_s are encapsulated into the dimensionless stiffness matrix \mathbf{K}^* . The solid Pois-
 211 son's ratio is set to 0.25 throughout this manuscript, unless otherwise mentioned.

212 **2.3 Eigenmode analysis**

213 We directly obtain the resonant frequencies through eigenmode analysis in the fre-
 214 quency domain. The spatially discretized dimensionless equation is written as

$$\frac{\partial^2 \bar{\mathbf{p}}^*}{\partial t^{*2}} = -\mathbf{B} \bar{\mathbf{p}}^*, \quad (18)$$

215 where

$$\mathbf{B} = \left(\frac{1}{C_L} \mathbf{I} + (\mathbf{K}^*)^{-1} \right)^{-1} \mathbf{A}^{*-1} \mathbf{D} \mathbf{T}. \quad (19)$$

216 The nondimensionalised Fourier transform is defined as

$$\hat{u}(\omega^*) = \int_{-\infty}^{+\infty} u(t^*) e^{i\omega^* t^*} dt^*, \quad (20)$$

217 where

$$\omega^* = \omega / (c_l / L), \quad (21)$$

218 is the dimensionless angular frequency. The dimensionless frequency is

$$f^* = \omega^* / (2\pi) = f / (c_l / L). \quad (22)$$

219 Taking the Fourier transform of equation (18), we have:

$$(\omega^*)^2 \hat{\mathbf{p}} = \mathbf{B} \hat{\mathbf{p}}, \quad (23)$$

220 where $(\omega^*)^2$ and $\hat{\mathbf{p}}$ are the eigenvalues and eigenvectors of the real matrix \mathbf{B} . Since we
 221 deal with inviscid fluids, we only seek real positive eigenvalues, which correspond to un-
 222 damped oscillatory modes. The resulting eigenvectors determine the spatial distribution
 223 of the pressure on the crack surface. Solving the resonant frequencies in dimensionless
 224 form is advantageous, because one can easily scale the solution to other parameters, such
 225 as crack length, crack width and solid stiffness, given the same dimensionless parame-
 226 ters, C_L , ν_s and crack topology.

227 **3 Verification and examples**

228 In this section, we first verify our implementation by comparing our results to an-
 229alytical solutions in the rigid solid limit and numerical solutions from existing studies.

230 We then present an example of simple intersecting crack geometry to demonstrate the
 231 utility of our method.

Table 1. The error between the theoretical and numerical resonant frequencies for the first 16 modes

Mode	Theoretical value	Numerical value	Error (%)
1	0.5000	0.5004	0.074
2	0.8333	0.8325	0.105
3	0.9718	0.9706	0.127
4	1.0000	1.0008	0.078
5	1.3017	1.3018	0.009
6	1.5000	1.5010	0.066
7	1.6667	1.6647	0.118
8	1.7159	1.7172	0.072
9	1.7401	1.7370	0.175
10	1.9437	1.9413	0.122
11	2.0000	2.0014	0.068
12	2.1667	2.1693	0.123
13	2.2423	2.2409	0.060
14	2.5000	2.4954	0.184
15	2.5000	2.5010	0.042
16	2.5495	2.5426	0.270

232 **3.1 Comparison with analytical solutions in a rigid solid**

233 We compute the \mathbf{K} matrix using the subroutines developed by Nikkhoo and Wal-
 234 ter (2015), which have been extensively used by other studies. The bulk part that needs
 235 to be validated is the FVM discretization of the Laplacian term. For that, we set solid
 236 rigidity to infinity and compare the numerical results to the analytical solution of the
 237 resonant frequencies of linear acoustic waves in a 2D rectangular domain with zero-flux
 238 boundaries (Rona, 2007). The solution is in a dimensionless form with a rectangular do-
 239 main of size 1 by 0.5 and a wave speed of 1. The comparison results for the first 16 modes
 240 are tabulated in Table 1. The excellent agreement between our numerical results and the

241 analytical solutions, with relative differences smaller than 0.2%, verifies our FVM dis-
 242 cretization of the Laplacian term.

243 **3.2 Comparison to numerical solutions by existing studies**

244 We compare solutions by our method (BEM+FVM) to those by B. Chouet (1986),
 245 Maeda and Kumagai (2017) and Shauer et al. (2021). With B. Chouet (1986) and Maeda
 246 and Kumagai (2017), we compare resonant frequencies of longitudinal modes for a rect-
 247 angular crack for various values of C_L (5, 15, 25, 50, 75, 100). With the GFEM by Shauer
 248 et al. (2021), we compare solutions of multiple modes on both rectangular and ellipti-
 249 cal cracks. The eigenmodes can be straightforwardly classified as longitudinal (variation
 250 only along the major crack axis), transverse (variation only along the minor crack axis),
 251 and mixed modes for a rectangular crack, but less so for an elliptical crack. Since the
 252 method by Shauer et al. (2021) discretizes the problem in time and, therefore, does not
 253 readily provide resonant frequencies, we ran their code to excite the fluid oscillation on
 254 the crack with $C_L = 100$ by a point injection source and then extract the resonant fre-
 255 quencies from the spectral peaks of the pressure records at a few receiving points. We
 256 use a Gaussian time function for the injection source $f(t) = \exp\left(-\frac{(t-t_c)^2}{T^2}\right)$ with
 257 $t_c = 0.5$, $T = 0.1$, to ensure a smooth start and a sufficiently wide spectrum to cover
 258 enough eigenmodes. Note that if either excitation or receiving points are placed on the
 259 nodal line, the eigenmode can not be excited or recorded. Therefore, not all eigenmodes
 260 are excited in the time domain simulation and we also only compare selective modes with
 261 Shauer et al. (2021), which is sufficient for verification purposes. The detailed geome-
 262 tries and simulation data are presented in Appendix B. Notably, the code of Shauer et
 263 al. (2021) has the capability of both considering (fully dynamic, FD) or neglecting the
 264 solid inertia (quasi-static, QS), allowing to investigate the impact of the solid inertia on
 265 crack wave resonant frequencies.

266 Tables 2 and 3 show the comparison of dimensionless resonant frequencies of se-
 267 lective eigenmodes from the GFEM program by Shauer et al. (2021) with those by our
 268 method for a rectangular and elliptical crack, respectively, with an aspect ratio of 0.5,
 269 major axis length of 1, and C_L of 100. The relative difference between our results and
 270 those from Shauer et al. (2021) are near 2% or less, with or without solid inertia. This
 271 close agreement not only demonstrates the validity of our approach but also reassures
 272 that the quasi-static solid response is a very good approximation when computing the

Table 2. Resonant frequencies by BEM+FVM and GFEM with or without inertia (FD or QS), rectangular crack

Mode	Resonant frequencies detected at receiving points by GFEM					BEM+FVM	Error FD (%)	Error QS (%)	
	(-0.5, 0)		(-0.2, 0.25)		(0, 0.25)				
	FD	QS	FD	QS	FD				QS
1	1.236	1.236	1.236	1.236		1.210	2.15	2.15	
2	2.727	2.691				2.662	2.44	1.09	
3			2.890	2.873	2.818	2.782	2.835	1.94	1.34
4			3.453	3.418			3.373	2.37	1.33
5	4.454	4.400	4.436	4.382			4.385	1.57	0.34
6					4.526	4.491	4.466	1.34	0.56
7			6.035	5.964			5.980	0.92	0.27
8	6.399	6.273			6.344	6.236	6.330	1.09	0.90

The bold values are used for error calculation. We use a of CL=100 and aspect ratio of 0.5
 Mode eigenfunctions are shown in Figure 2.

Table 3. Resonant frequencies by BEM+FVM and GFEM without inertia (QS), elliptical crack

Mode	The resonant frequencies can be detected at detection points			BEM+FVM	Error (%)
	(-0.5, 0)	(0, 0.25)	(0, 0)		
1	1.527			1.518	0.59
2	3.027		3.090	3.050	0.75
3		3.290		3.241	1.51
5	4.890			4.816	1.54
7	6.890	6.853	6.944	6.771	1.76
8		7.308	7.235	7.107	1.80

The bold values are used for error calculation. We use a of CL=100 and aspect ratio of 0.5
 Mode eigenfunctions are shown in Figure 3.

273 crack wave resonant frequencies, at least for a C_L of 100. A similar conclusion has also
 274 been reached by Shauer et al. (2021). Since we assume a quasi-static solid response, it
 275 is reasonable that our results have a better agreement to those by GFEM without in-
 276 ertia.

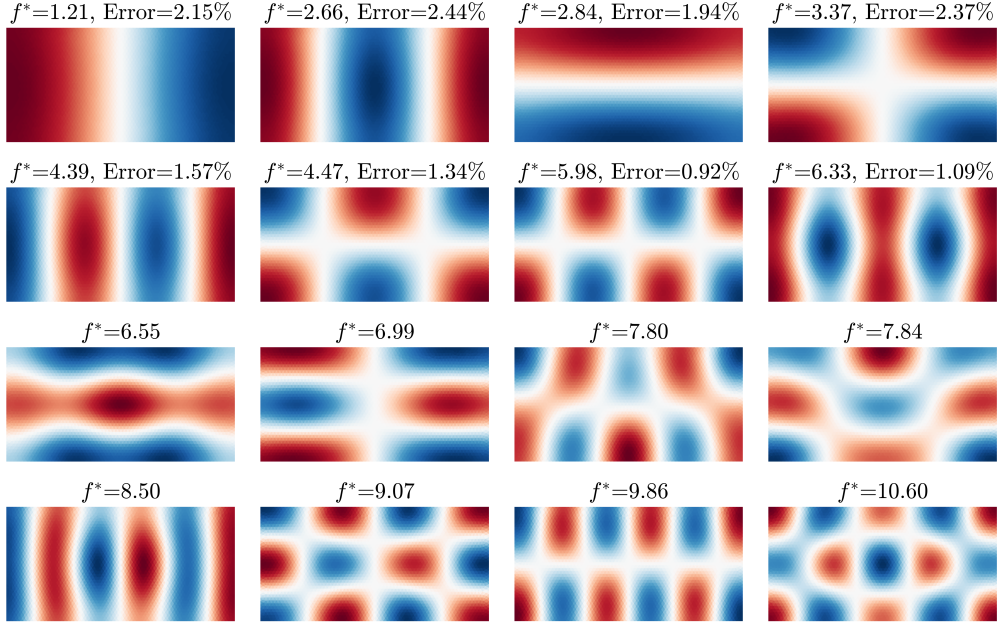


Figure 2. Dimensionless frequencies and eigenfunctions of the first 16 resonant modes (numbered in an ascending order in frequencies) of a rectangular crack with $C_L=100$ and aspect ratio of 0.5 calculated by BEM+FVM. The errors of selective resonant frequencies between the BEM+FVM and GFEM without inertia are shown in Table 2. The white color indicates the nodal lines.

277 The pressure eigenfunctions of the first 16 resonant modes are displayed in Figure
 278 2 for a rectangular crack and Figure 3 for an elliptical crack, showing a rich spectrum
 279 of spatial variations including longitudinal, transverse, and mixed modes. Different modes
 280 can produce different near and far field radiation patterns, that may be detectable in real
 281 seismic data (e.g., Liang et al., 2020).

282 The dimensionless frequencies of the first 9 longitudinal modes for rectangular cracks
 283 by various methods with different crack stiffness ratios are shown in Figure 4. The re-
 284 sults of Shauer et al. (2021) are only computed for a C_L of 100. For ease of comparison,
 285 we convert dimensionless frequencies f^* in our studies to those in B. Chouet (1986) f_C^* ,

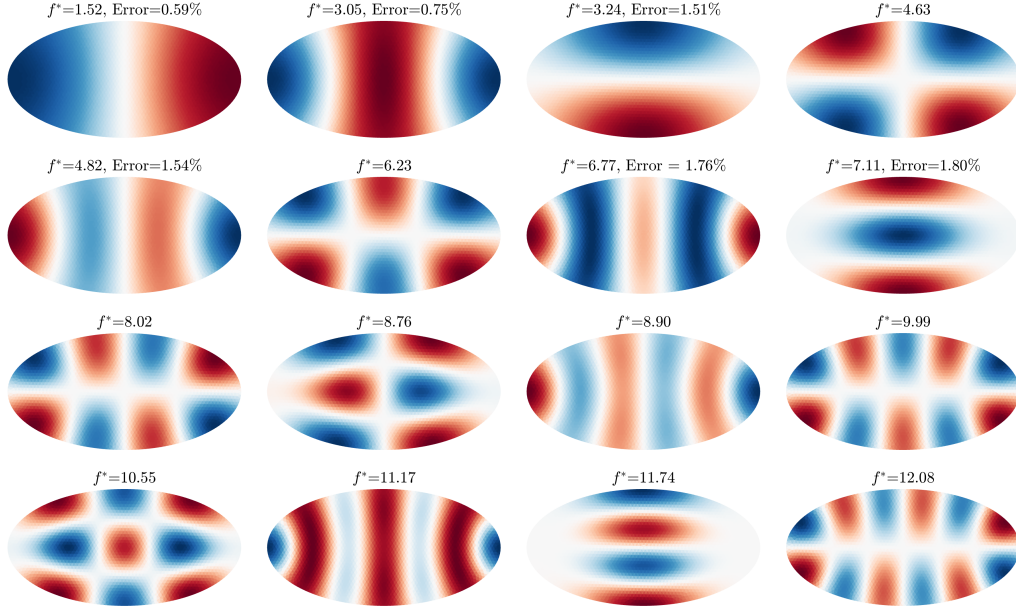


Figure 3. Same as Figure 2 but for an elliptical crack.

286 which are related by $f_C^* = f^* c_l / c_P$. Overall, our results match well with those by Shauer
 287 et al. (2021) (relative error < 3%) and also qualitatively well with those by B. Chouet
 288 (1986) and Maeda and Kumagai (2017). However, there are quantitative discrepancies
 289 between our results and those by B. Chouet (1986) (relative error 8.83-23.43%) and Maeda
 290 and Kumagai (2017) (relative error 2.72-16.63%, see the supporting information for tab-
 291 ulated errors). Particularly, both B. Chouet (1986) and Maeda and Kumagai (2017) sys-
 292 tematically give lower frequencies than those by our method and Shauer et al. (2021).
 293 We suspect these discrepancies are likely due to differences in spatial and temporal sam-
 294 pling, or domain sizes used in the FDM code in B. Chouet (1986) and Maeda and Ku-
 295 magai (2017). Particularly, a truncated domain in the FDM results in a more compli-
 296 ant solid response (Korneev et al., 2014), which in turn results in a lower crack wave speed
 297 and resonant frequencies. Our method uses boundary elements and thus an infinite do-
 298 main is directly satisfied. For this reason, when comparing results with Shauer et al. (2021),
 299 we deliberately used a very large domain (10 times the length of the crack) in the GFEM
 300 code to minimize its boundary effect using an unstructured grid, coarsening in regions
 301 far from the crack.

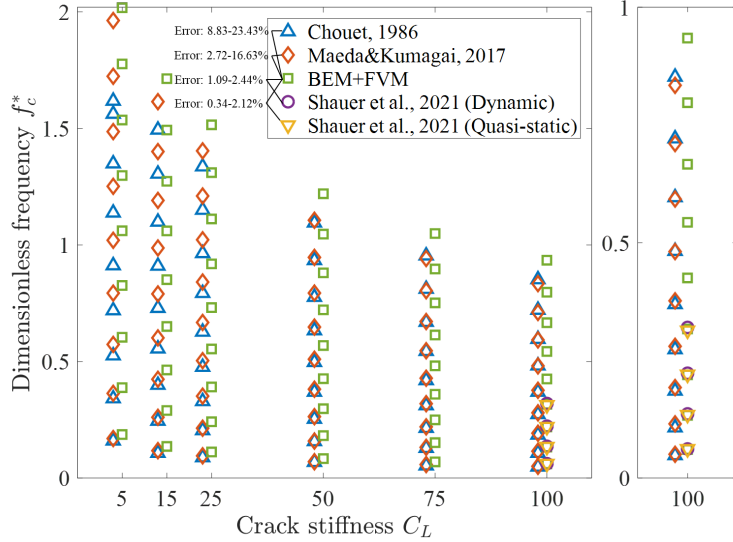


Figure 4. Dimensionless frequencies f_C^* of longitudinal modes for rectangular cracks with different C_L (5, 15, 25, 50, 75, 100) by various methods, and a zoom-in view of the case $C_L = 100$ on the right panel. Results by B. Chouet (1986) and Maeda and Kumagai (2017) are slightly shifted in the horizontal axis to avoid overcrowding the figure.

302

3.3 An example of intersecting cracks

303

304

305

306

307

308

309

310

311

312

313

314

315

316

We now apply our method to one example of intersecting cracks, one full ellipse with a half-elliptical branch, and obtain the first 16 eigenmodes, shown in Figure 5. Interactions between multiple cracks result in more complex resonant modes than in single cracks (shown in Figures 3 and 4). For example, the fundamental mode now involves fluid exchange between the major crack and the branch, and has a lower frequency than the fundamental mode of the major crack (the second mode in this case). When nodal lines coincide with the intersecting edge, resonances can be isolated on the major crack, such as modes 2, 7, 8, 13 and 16. Temporal manifestation of these modes requires a more peculiar condition: the excitation must not be located in the branch. One can certainly add more complexities in the crack network, such as asymmetries, non-planarity or more intricate coupling, and expect to encounter richer eigenmodes. However, such modeling only becomes meaningful when more compelling observations exist and require. We will demonstrate later how a particular crack shape can explain the ratio of the first two spectral peaks in the VLP seismic data at the Fani Maoré, Mayotte submarine volcano. Ex-

317 cept for that, we decide to leave the analysis of eigenmodes of a more complex crack net-
 318 work for future investigation.

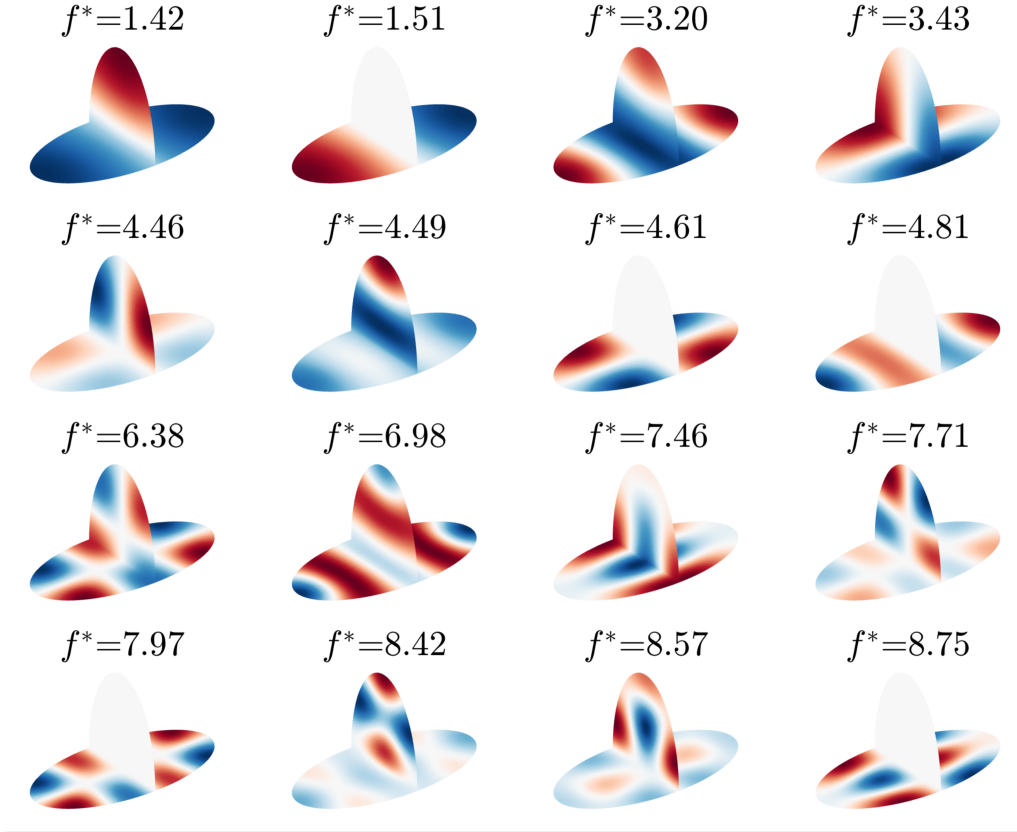


Figure 5. The first 16 eigenmodes of a simple two-intersecting-cracks geometry: a half ellipse intersecting a full ellipse (aspect ratio 0.5) along its minor axis. The major axis length of the full elliptical crack is chosen as L for the non-dimensionalisation.

319 **4 Effect of aspect ratio α and crack stiffness ratio C_L**

320 In this section, we present the effect of α and C_L on the resonant frequencies of rect-
 321 angular and elliptical cracks, with major and minor axes in the x - and y -directions,
 322 respectively. Maeda and Kumagai (2017) presented a similar analysis for rectangular cracks,
 323 but only on longitudinal and transverse modes. Here, we include the mixed modes and
 324 the results for elliptical cracks. We fixed $C_L = 100$ when varying α (from 0.05 to 1.00
 325 with an increment of 0.05) and fix $\alpha = 0.5$ when varying C_L (from 5 to 100 with an
 326 increment of 5). The frequencies of the first 16 eigenmodes are tabulated in the Support-

327 ing information. Here, we select 9 representative modes and visualize them in Figures
 328 6-9. For rectangular cracks, we associate to each mode a pair of numbers (i, j) that de-
 329 note the number of half wavelengths in the x - and y -directions. For instance, the fun-
 330 damental mode $(1, 0)$ is a longitudinal mode with one half wavelength pressure variation
 331 in the x -direction and quasi-uniform in the y -direction. Such numbering becomes less
 332 obvious for elliptical cracks, especially when the aspect ratio approaches 1, for which the
 333 eigenfunctions are better characterized by radial and circumferential variations. Nonethe-
 334 less, for the ease of comparing results with rectangular cracks, we still number the rep-
 335 resentative modes in Figures 7 and 9 approximately into longitudinal, transverse, and
 336 mixed modes.

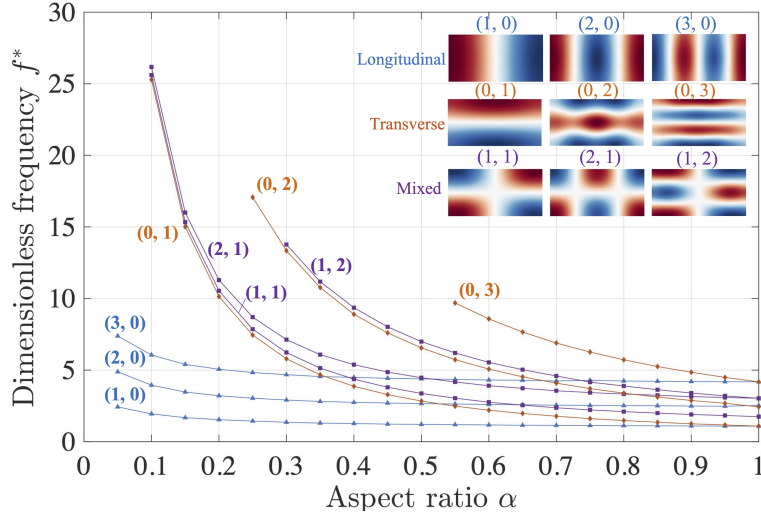


Figure 6. Dimensionless resonant frequencies of representative modes of rectangular cracks as a function of the aspect ratio α . C_L is fixed to 100. The eigenfunctions displayed are for an aspect ratio of 0.55. Certain high order mixed and transverse modes rank outside of the first 16 eigenmodes that we store, which causes the apparent absence of data at low aspect ratios.

337 4.1 Effect of aspect ratio

338 The variation of resonant frequencies with aspect ratio is shown in Figure 6 and
 339 7 for rectangular and elliptical cracks, respectively. For both cases, decreasing the as-
 340 pect ratio increases the crack stiffness from the transverse direction and results in higher
 341 resonant frequencies for all the modes. This effect is relatively mild for longitudinal modes
 342 but rather steep for transverse and mixed modes. For instance, when α of a rectangu-

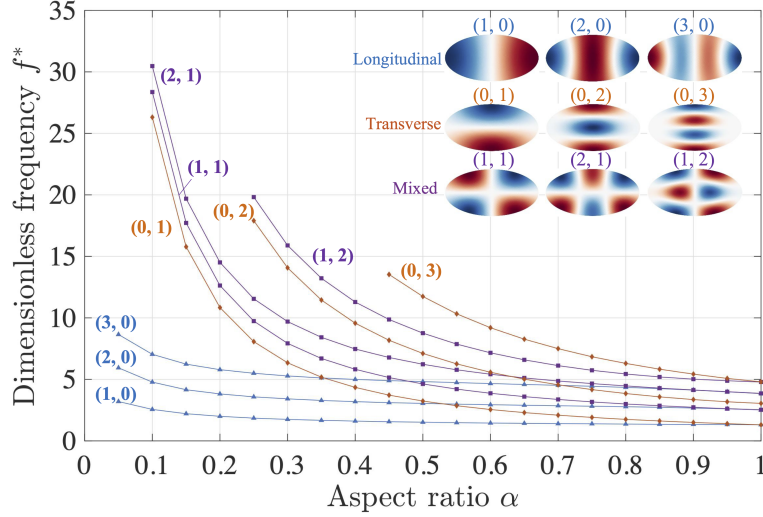


Figure 7. Same as Figure 6 but for elliptical cracks. Note that the mode numbers (i, j) are not strictly valid for an elliptical crack but are useful for our interpretation (more explanation in the main text).

lar crack decreases from 1.0 to 0.1, the frequency of the fundamental mode $(1, 0)$ increases by ~ 1.8 fold while the frequency of the mixed mode $(1, 1)$ increases by ~ 14.6 fold. As a result, the first few resonant modes are predominantly longitudinal for both rectangular and elliptical cracks at low aspect ratios (below 0.2). For a similar mode, the resonant frequency of an elliptical crack is consistently higher than that of the rectangular crack. This is expected as the elliptical crack is narrower in the transverse direction and thus stiffer than a rectangular crack of the same length and aspect ratio.

Another clear feature, for both rectangular and elliptical cracks, is that frequencies of modes with same wavelengths in the transverse direction converge as α decreases. For instance, frequencies of mixed modes $(1, 1)$ and $(2, 1)$ converge to the values of transverse mode $(0, 1)$. Similar convergence also exists for modes $(0, 2)$ and $(1, 2)$. This is expected because the crack wave speed, in the limit of low aspect ratio, is primarily controlled by the short wavelength in the transverse direction. As α increases, the frequencies of different modes become more intermingled and mode degeneration occurs, where modes with distinct eigenfunctions share the same frequency. It is well known that mode degeneration occurs at $\alpha = 1$ due to the geometric symmetry of a square or circle. What we show here is that mode degeneration also occurs at intermediate aspect ratios. For

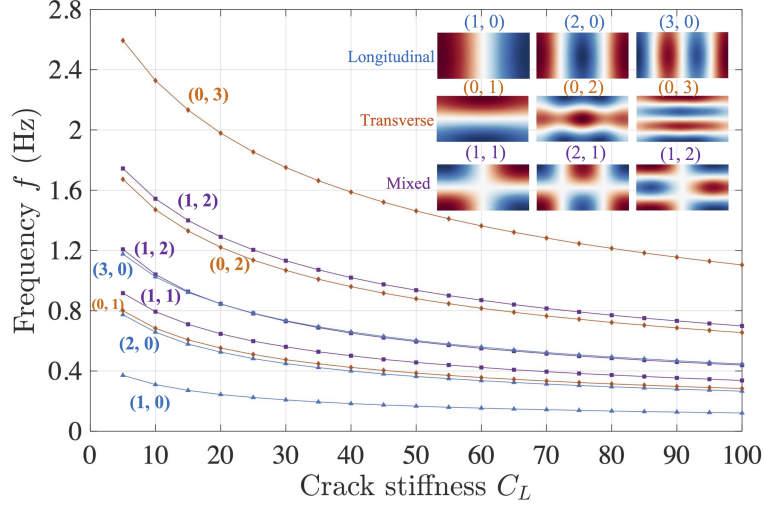


Figure 8. Resonant frequencies of representative modes of rectangular cracks as a function of the crack stiffness C_L . The aspect ratio α is set as 0.5

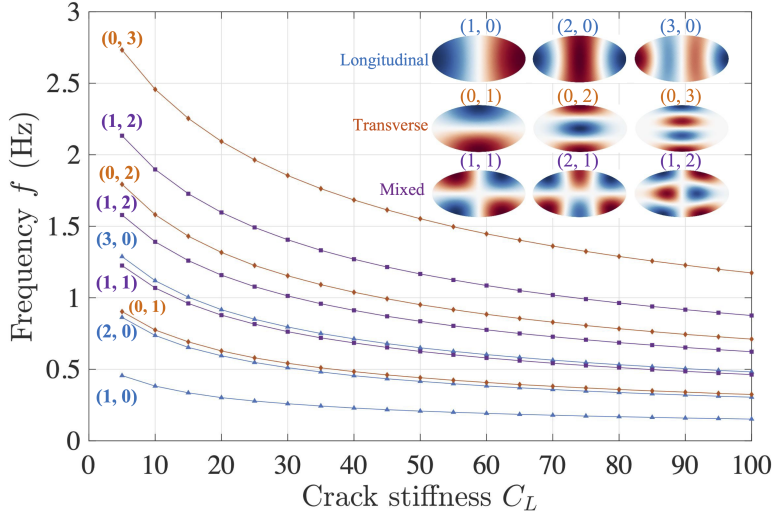


Figure 9. Same as Figure 8 but for elliptical cracks

360 instance, modes $(3, 0)$ and $(0, 1)$ for both a rectangular and elliptical crack share sim-
 361 ilar frequencies when $\alpha \approx 0.35$.

362 4.2 Effect of crack stiffness ratio

363 Since the normalization constant $(c_f/\sqrt{C_L})/L$ for frequency changes with C_L , we
 364 visualize the actual resonant frequency f , instead of f^* . We use $c_f = 1$ m/s and $L =$
 365 1 m to scale f^* to f . C_L is the key dimensionless parameter that controls the crack wave

366 propagation: the higher the value of C_L , the lower the phase velocity (e.g., B. Chouet,
 367 1986; Maeda & Kumagai, 2017). As a result, the resonant frequencies of all modes for
 368 both rectangular (Figure 8) and elliptical cracks (Figure 9) decrease continuously as C_L
 369 increases. Again, for a similar mode, the resonant frequencies of an elliptical crack is con-
 370 sistentlly higher than those of a rectangular crack given the same axial lengths.

371 5 Energy dissipation

372 Since we currently focus on computing crack resonant frequencies in complex crack
 373 geometries, we assume both an inviscid fluid and a quasi-static solid and we do not con-
 374 sider energy dissipation, from either fluid viscosity or seismic radiation. When damp-
 375 ing exists, the resonant frequency becomes complex and the rate of decay is quantified
 376 by the quality factor

$$Q = \frac{\text{Re}(f)}{2\text{Im}(f)}, \quad (24)$$

377 which is also the number of cycles for an oscillation's energy to fall off to $e^{-2\pi} \sim 0.2\%$
 378 of its original value. The effect of viscous damping has been investigated analytically with
 379 fully dynamic (Korneev, 2008) and quasi-static solid response (Lipovsky & Dunham, 2015)
 380 on an infinite crack. However, the applicability of the Q formula on a finite crack has
 381 not yet been tested. In addition, the convoluted derivation in Korneev (2008) makes it
 382 difficult to quantify the relative contribution of different dissipative sources to the to-
 383 tal energy loss. On the other hand, numerical studies on rectangular cracks (e.g., Ku-
 384 magai & Chouet, 2000) have investigated the Q caused by seismic radiation but adopted
 385 a simplistic treatment of the fluid viscosity, either an inviscid or fully-developed flow. In
 386 this section, we offer a semi-analytical discussion of energy dissipation under a few as-
 387 sumptions and attempt to address two questions: (1) does the formula of Q developed
 388 by Lipovsky and Dunham (2015) for an infinite crack also apply to a finite crack? (2)
 389 which of the two sources of energy dissipation, fluid viscosity and seismic radiation, is
 390 more significant?

391 5.1 The applicability of Q formula from dispersion to a finite crack

392 We consider a viscous fluid with kinematic viscosity μ . To focus on the effect of
 393 the finite geometry, we compare analytical solutions by Lipovsky and Dunham (2015)
 394 to numerical solutions by Liang et al. (2020) for a rectangular crack, both of which as-

395 sume a quasi-static solid response. For simplicity, we focus on the boundary layer limit

$$\zeta = w_0/\sqrt{4\nu/\omega} \gg 1, \quad (25)$$

396 where the crack aperture w_0 is much larger than the thickness of the viscous boundary
 397 layer $\sqrt{4\nu/\omega}$. In this limit, Q is high and ω can be well approximated by the inviscid
 398 solution. The analytical formula of Q for crack waves with real wavenumber is given by
 399 equation (80) in Lipovsky and Dunham (2015) and, after neglecting the small imaginary
 400 part of phase velocity when $\zeta \gg 1$, we have:

$$Q = \sqrt{2}\zeta. \quad (26)$$

401 The hypothesis is that this expression for Q also holds, at least approximately for a fi-
 402 nite rectangular crack, regardless of its geometric shape, as long as w_0 , μ and ω are known.
 403 We perform numerical simulations using the program by Liang et al. (2020), who em-
 404 ployed a finite difference method on a stretched grid to deal with the narrow viscous bound-
 405 ary layer. We set $L = 100$ m, $K_f = 1$ Pa, $G = 1$ Pa, $w_0 = 1$ m, which results in a C_L
 406 of 100, and solve for the inviscid resonant angular frequencies ω of rectangular cracks
 407 of two aspect ratios, 0.5 and 1.0. We then adjust μ so that ζ takes the values of 10, 20,
 408 40, 60, 80, 100 and 200. We consider the first two modes of the crack with aspect ratio
 409 of 0.5 and the fundamental mode of the square crack to represent different mode types
 410 and crack shapes. The Q values of viscous cases are obtained using the methodology by
 411 Liang et al. (2020) and the comparison to equation (26) is shown in Figure 10.

412 As shown in Figure 10, the prediction by the analytical formula in Lipovsky and
 413 Dunham (2015) matches well the numerical solutions. The agreement gets better at large
 414 ζ , where the assumption of boundary layer limit becomes more accurate. The differences
 415 between the numerical and analytical solutions are less than 5% at $Q > 40$, while the
 416 difference at $Q = 10$ is $\sim 14\%$. Another encouraging finding is that aspect ratios and
 417 mode numbers of rectangular cracks have a negligible impact on the value of Q as long
 418 as ζ is the same. We thus postulate that the Q formula is likely to hold also for other
 419 crack shapes or even a crack network. We further propose that one may first approxi-
 420 mate the resonant frequency ω of complex shaped cracks using the inviscid solution ef-
 421 ficiently determined by our method, and then directly estimate Q using the analytical
 422 formula. However, future numerical studies considering both complex crack geometry
 423 and fluid viscosity are necessary to rigorously test this hypothesis.

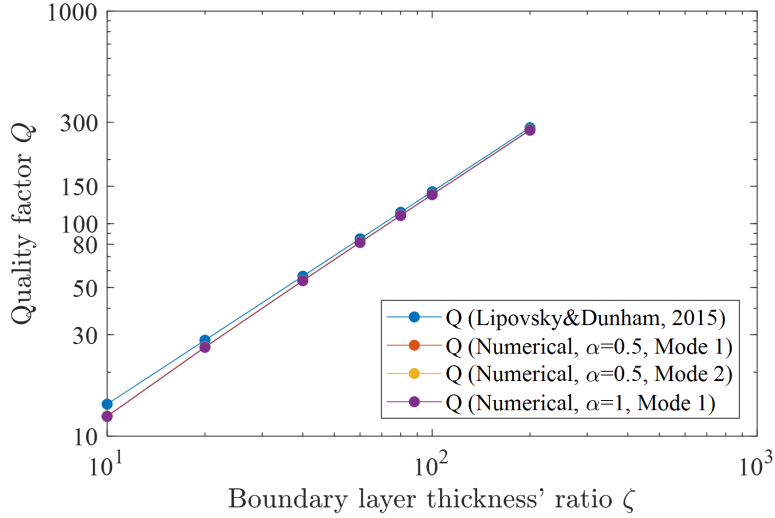


Figure 10. Quality factor of various resonant modes of rectangular cracks as a function of the boundary layer thickness ratio ζ .

424

5.2 The competition between radiation and viscous damping

425

426

427

428

429

430

431

432

433

434

435

436

Instead of considering the fully dynamic solid response (e.g., Korneev, 2008), we assume a quasi-dynamic solid response (e.g., Rice, 1993; Geubelle & Rice, 1995), which allows to explicit extract the instantaneous long wavelength emission perpendicular to the crack surface, the radiation damping (*RD*) term. We also consider an infinite crack in two dimensions for the ease of theoretical treatment following Lipovsky and Dunham (2015). By neglecting the wave mediated stresses and the seismic diffraction at the finite crack tips, the radiation we consider is an underestimate, but it is still useful for understanding the relative importance of various dissipation sources. Since resonances tend to be overdamped in the fully developed flow limit $\zeta \gg 40$ (Korneev, 2008; Lipovsky & Dunham, 2015), we continue to focus on the boundary layer limit $\zeta \ll 40$. We explicitly identify the radiation and viscous damping terms in the governing equation and then compute the ratio of their magnitudes.

437

438

439

The width-averaged crack wave equation considering viscous wall traction is obtained by combining the mass and momentum balance equations in Lipovsky and Dunham (2015),

$$\frac{\rho_f}{K_f} \frac{\partial^2 p}{\partial t^2} + \frac{\rho_f}{w_0} \frac{\partial^2 w}{\partial t^2} - \frac{\partial^2 p}{\partial x^2} - \frac{2}{w_0} \frac{\partial \tau}{\partial x} = 0, \quad (27)$$

440 where τ is the wall shear traction. We introduce the double Fourier transform of an ar-
 441 bitrary function $F(x, t)$ as

$$\hat{F}(k, \omega) = \int_{-\infty}^{+\infty} \int_{-\infty}^{+\infty} F(x, t) e^{-i(kx - \omega t)} dt dx. \quad (28)$$

442 Applying it to equation (27) leading to

$$-\omega^2 \rho_f \left(\frac{\hat{p}}{K_f} + \frac{\hat{w}}{w_0} \right) + k^2 \hat{p} - ik \frac{2}{w_0} \hat{\tau} = 0. \quad (29)$$

443 Using equation (38) in Lipovsky and Dunham (2015) and neglecting horizontal wall mo-
 444 tion, the wall shear traction is related to fluid pressure by

$$\hat{\tau} = -ikw_0\Omega\hat{p}/2, \quad (30)$$

445 where

$$\Omega = \left(\sqrt{i}/\zeta \right) \tanh \left(\zeta/\sqrt{i} \right), \quad (31)$$

446 and tends to \sqrt{i}/ζ in the boundary layer limit. Therefore, the viscous damping (*VD*)
 447 term in the equation is

$$VD = k^2\Omega\hat{p}. \quad (32)$$

448 Applying the quasi-dynamic solid response (Geubelle & Rice, 1995), the fluid pressure
 449 and crack opening are related by

$$\hat{p} = \frac{Gk\hat{w}}{2(1 - \nu_s)} - i\omega\eta_R\hat{w}, \quad (33)$$

450 where the two terms on the right hand side are the quasi-static response and radiation
 451 damping (*RD*), respectively, and $\eta_R = \rho_s c_p/2$ is the radiation damping coefficient. The
 452 ratio between the *QS* and *RD* terms is approximately $c_s^2/(c_p c)$ (dropping terms involv-
 453 ing Poisson's ratio), where $c = \omega/k$ is the crack wave phase velocity. In the low-frequency
 454 limit, which we are interested in, the crack wave speed is much smaller than the speeds
 455 of the solid body waves, $c \ll c_s \sim c_p$, and thus the *RD* term is much smaller than the
 456 *QS* term. Substituting equation (33) into (29) and approximating \hat{w}/\hat{p} using the *QS* part,
 457 we obtain the *RD* term in equation (29) as

$$RD = i\omega^3 \frac{\rho_f n_R}{K_f} \hat{w} \approx i\omega^3 \frac{\rho_f n_R}{K_f} \frac{2(1 - \nu_s)}{Gk} \hat{p}. \quad (34)$$

458 The ratio between *RD* and *VD* is

$$\frac{RD}{VD} = i c^3 \frac{\rho_f n_R}{K_f} \frac{2(1 - \nu_s)}{G\Omega} = i \frac{c_p c^3 (1 - \nu_s)}{c_f^2 c_s^2 \Omega}. \quad (35)$$

459 In the boundary layer limit, the magnitude of this ratio becomes

$$\left| \frac{RD}{VD} \right| = \frac{c_p c^3}{c_f^2 c_s^2} \zeta (1 - v_s). \quad (36)$$

460 When the overall damping is small, the crack wave phase velocity as a function of wave-
461 length λ is well approximated by the inviscid dispersion relation:

$$c = \sqrt{\frac{2\pi G w_0}{\lambda \rho_f (1 - v_s)}} \sim c_f / \text{sqrt} C_\lambda, \quad (37)$$

462 where $C_\lambda = K_f \lambda / G w_0$ is a crack stiffness ratio similar to C_L but replacing L by λ . Fi-
463 nally, we obtain RD/VD , which scales as

$$\left| \frac{RD}{VD} \right| \sim \frac{c_p c_f}{c_s^2} \frac{\zeta}{C_\lambda^{3/2}} = \frac{c_p c_s}{c_f^2} \zeta \left(\frac{w_0 \rho_s}{\lambda \rho_f} \right)^{3/2}, \quad (38)$$

464 after dropping small constants such as 2, π and μ_s . $|RD/VD|$ is governed by three di-
465 mensionless parameters: $\frac{c_p c_f}{c_s^2}$, C_λ and ζ . The first parameter one is controlled by the body
466 wave speeds of the solid and fluid and is not related to the crack geometry. For a typ-
467 ical crustal rock and liquid fluid, for instance with $c_f = 1500$ m/s, $c_p = 4500$ m/s, and
468 $c_s = 2500$ m/s, $\frac{c_p c_f}{c_s^2}$ is near unity. However, exsolved gases in liquid fluid, common in
469 shallow volcanic or geothermal environments (e.g., Kumagai & Chouet, 1999, 2001), can
470 significantly decrease the sound speed of the mixture, resulting in a much smaller $\frac{c_p c_f}{c_s^2}$.
471 The trade-off between C_λ and ζ in controlling $|RD/VD|$ is displayed in Figure 11. In
472 the regime of high ζ and low C_λ , seismic radiation dominates over viscous damping, while
473 in the regime of low ζ and high C_λ vice versa. Note that increasing λ or decreasing fre-
474 quency ω while fixing other parameters increases C_λ and simultaneously decreases ζ , both
475 of which lead to a lower percentage of damping in radiation.

476 **6 Application to VLP seismic signals during the Mayotte volcano-seismic** 477 **crisis**

478 Since 10 May 2018, an unprecedented submarine volcano-seismic crisis occurred
479 30 km east of Mayotte Island (France), featuring a lithosphere-scale dyke intrusion and
480 drainage ($\sim 5 \text{ km}^3$) of deep magma reservoirs and producing exceptionally deep seismic-
481 ity and substantial surface deformation (Cesca, Letort, et al., 2020; Feuillet et al., 2021;
482 Saurel et al., 2021; Mittal et al., 2022; Mercury et al., 2022; Retailleau et al., 2022). By
483 mid June of 2018, sustained long duration and highly oscillatory VLP seismic signals (see
484 an example in Figure 12a) have been observed and persist since, which are associated
485 with resonances of magma-filled cracks excited by nearby volcano-tectonic (VT) events

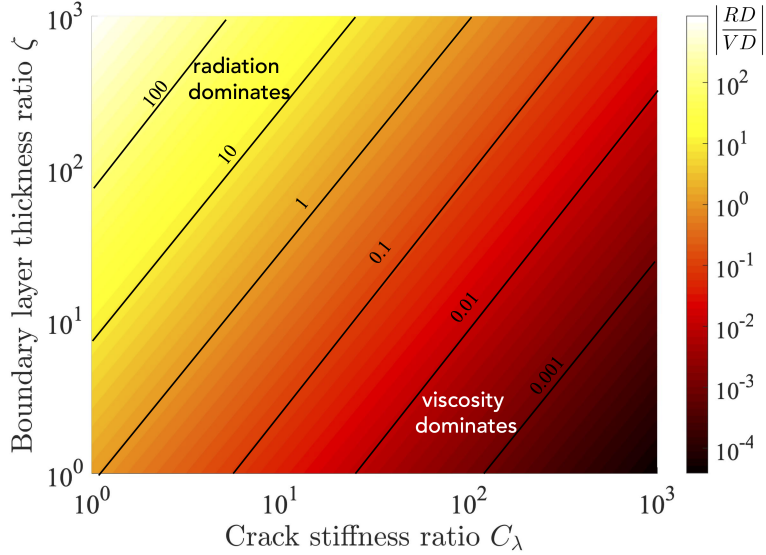


Figure 11. $|RD/VD|$ as a function of the crack stiffness ratio C_λ and the boundary layer thickness ratio ζ . Parameters used are $c_f = 1500$ m/s, $c_p = 4500$ m/s, and $c_s = 2500$ m/s.

486 or possible piston collapse movements (Cesca, Letort, et al., 2020; Feuillet et al., 2021).
 487 The stack of spectra of multiple VLP events reveals multiple resonant modes, among which
 488 the fundamental mode with period ~ 15.5 s is present in all events, but not all higher modes
 489 are manifested in each event, probably due to differences in the excitation. The funda-
 490 mental frequency can be readily explained by the crack model upon choosing a proper
 491 crack length and aperture (Cesca, Letort, et al., 2020). However, as shown in Figure 12b,
 492 the uneven spacing between resonant modes implies additional complexity in the source.
 493 Particularly, the ratio between the first higher mode and the fundamental mode is $f_2/f_1 \approx$
 494 2.5. As shown in Figures 6 and 7, this value can not be explained by a simple rectan-
 495 gular or elliptical crack. Here, we show this observation can be explained by a dumbbell-
 496 shaped crack (Figure 12c). This crack shape is compatible with the f_2/f_1 data, but might
 497 still differ from the real crack geometry in Mayotte as we have not made a systematic
 498 attempt to also match the frequencies of other higher modes. However, this example is
 499 sufficient to demonstrate the potential application of the developed method. One pro-
 500 found question is perhaps whether one can reconstruct the topology of the crack given
 501 the information of all the resonant frequencies. Mark Kac also asked a similar question
 502 “Can one hear the shape of a drum?” (Kac, 1966). Unfortunately, the answer is nega-
 503 tive: there exist multiple isospectral geometries that share the same resonant frequen-

504 cies, as mathematically proven by Gordon et al. (1992). However, these isospectral ge-
 505 ometries are rare even though they do exist and one can still decipher the shape of the
 506 resonator given additional constraints of the vibration pattern, which in practice requires
 507 dense geophysical observation particularly in the near field. A formal inversion proce-
 508 dure would need to be developed in the future to find the optimal crack geometry or topol-
 509 ogy of interconnected crack networks that best explains all the observed resonant fre-
 quencies and other geophysical constraints.

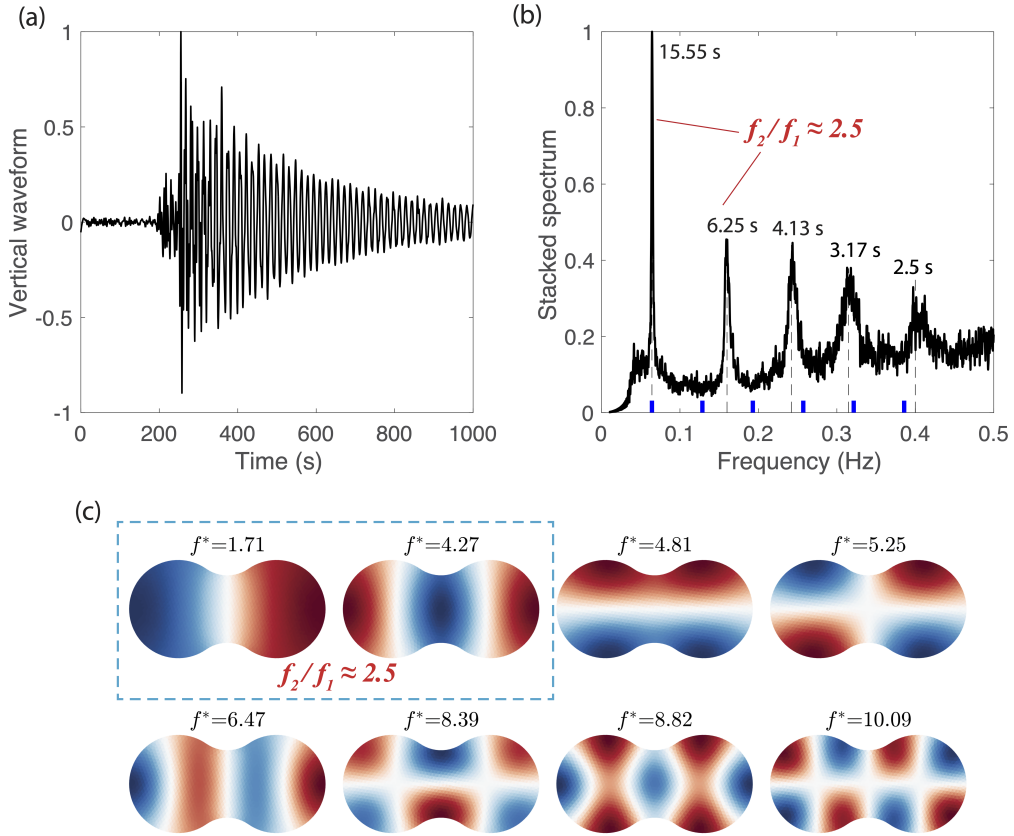


Figure 12. (a) Normalized vertical acceleration waveform of an representative VLP event (on 11 November 2018, bandpass filtered to 0.02-0.1 Hz) at the nearest broadband seismic station YTMZ on land, during the volcano-seismic crisis near Mayotte. (b) Stacked spectrum of 21 strong VLP signals compiled by Cesca, Letort, et al. (2020), highlighting multiple unevenly spaced resonant modes (dashed lines). Particularly, the frequency ratio between the first two modes $f_2/f_1 \approx 2.5$. The blue ticks indicate the integer multiples of the fundamental frequency. (c) Eigenmodes of a possible crack shape that satisfies $f_2/f_1 \approx 2.5$.

511 7 Summary

512 We have developed a hybrid method that couples the boundary element and finite
 513 volume method to efficiently compute the resonant modes of fluid-filled cracks with com-
 514 plex geometry. Particularly, the BEM reduces three dimensional cracks to 2D surfaces,
 515 substantially decreasing the number of degrees of freedom. By performing eigenmode
 516 analysis in the frequency domain, we avoid errors from both the time discretization and
 517 spectral analysis of the time domain data. We solve the problem in dimensionless form
 518 so that the results can be conveniently scaled to other crack sizes. After proper verifi-
 519 cation, we apply our method to an example of a crack network, revealing distinct res-
 520 onant frequencies and vibration patterns, which may be utilized to infer more accurately
 521 crack shapes from seismic data.

522 We then systematically analyze the influence of crack aspect ratio and crack stiff-
 523 ness on the resonant frequencies for both rectangular and elliptical cracks, which are com-
 524 mon models for interpreting real data. In general, rectangular and elliptical cracks share
 525 similar eigenmode types and frequencies, while the elliptical crack has slightly higher re-
 526 sonance frequencies due to the reduced length of the minor axis. At a high aspect ratio,
 527 the frequencies of various mode types (longitudinal, transverse and mixed) are intermin-
 528 gled and mode degeneration occurs. Reducing the aspect ratio increases the frequencies
 529 of all the modes, but more intensely for transverse and mixed modes than for longitu-
 530 dinal modes. In addition, at low aspect ratio, frequencies of modes (transverse or mixed)
 531 with the same wavelengths in the transverse direction converge and differentiating them
 532 requires additional knowledge of their vibration patterns. On the other hand, increas-
 533 ing C_L results in a decrease in resonant frequencies for all modes, regardless of the crack
 534 geometry, which is primarily due to the decrease in crack wave propagation speed.

535 The major part of this work does not consider fluid viscosity or seismic radiation,
 536 and thus cannot be used to directly compute the quality factor Q . However, by making
 537 a few assumptions, we offer additional theoretical discussion on the energy dissipation.
 538 First, by comparing numerical to analytical solutions, we confirm that the simple for-
 539 mula $Q = \sqrt{2}\zeta$ derived by Lipovsky and Dunham (2015) is a rather good approxima-
 540 tion for a rectangular crack when the thickness of the viscous boundary layer is much
 541 smaller than the crack width, regardless of crack aspect ratio or vibrational mode. This
 542 is an encouraging finding that suggests one may first obtain the inviscid resonant fre-

543 frequencies using our method and then apply analytical formula to compute Q . Note that
 544 this formula still does not consider seismic radiation. We then derived the relative ra-
 545 tio of the radiation damping to viscous damping, assuming a quasi-dynamic solid response
 546 on an infinite crack. We show that this ratio is primarily controlled by three dimension-
 547 less parameters: $c_p c_f / c_s^2$, C_λ and ζ . Particularly, in the limit of high ζ and low C_λ , seis-
 548 mic radiation dominates over viscous damping while the opposite is true in the limit of
 549 low ζ and high C_λ . Note that the seismic radiation considered here is a lower bound as
 550 we neglected the wave-mediated stresses and the seismic radiation at the finite crack tip.
 551 However, our theoretical development still offers a valuable insight into the partition of
 552 damping in crack waves.

553 Finally, we obtain one possible crack shape, a “dumbbell”, that successfully explains
 554 the ratio of frequencies of the first two modes in the VLP seismic data during the 2018
 555 Fani Maoré, Mayotte submarine volcanic eruption. This shape is one possibility and may
 556 be updated when additional higher modes and geophysical constraints are integrated into
 557 the analysis. In addition, the method developed here can be directly applied to other
 558 scenarios, such as unconventional oil and gas fields and glacier hydraulics. Future work
 559 requires a rigorous treatment of fluid viscosity, elastodynamics, and coupling to other
 560 geometries such as conduits and equidimensional chambers.

561 **8 Acknowledgments**

562 This work is funded by the early career research grant by the National Science Fun-
 563 dation of China (NSFC) with grant No. 42204059 and the Fundamental Research Funds
 564 for the Central Universities disseminated by IDMR at Sichuan University. It was also
 565 supported by the French government, through the UCAJEDI Investments in the Future
 566 project (ANR-15-IDEX-01) managed by the National Research Agency (ANR).

567 **9 Data Availability Statement**

568 The source code and the input files associated with the simulation cases are included
 569 in the Zenodo data repository at Liang et al. (2023). The VLP catalog of the Mayotte
 570 crisis is provided by Cesca, Heimann, et al. (2020) and is freely available online.

571 **References**

- 572 Aki, K., Fehler, M., & Das, S. (1977). Source mechanism of volcanic tremor: Fluid-
 573 driven crack models and their application to the 1963 Kilauea eruption. *Journal of Volcanology and Geothermal Research*, *2*(3), 259–287. doi: 10.1016/0377-
 574 0273(77)90003-8
- 575
- 576 Aster, R. C. (2019). Interrogating a surging glacier with seismic interferometry. *Geophysical Research Letters*, *46*(14), 8162–8165. doi: 10.1029/2019GL084286
- 577
- 578 Berre, I., Doster, F., & Keilegavlen, E. (2019). Flow in fractured porous media:
 579 A review of conceptual models and discretization approaches. *Transport in Porous Media*, *130*(1), 215–236. doi: 10.1007/s11242-018-1171-6
- 580
- 581 Cao, H., Medici, E., & Askari, R. (2021). Physical modeling of fluid-filled fractures
 582 using the dynamic photoelasticity technique. *Geophysics*, *86*(1), T33–T43. doi:
 583 10.1190/geo2020-0037.1
- 584 Cesca, S., Heimann, S., Letort, J., Razafindrakoto, H., Dahm, T., & Cotton, F.
 585 (2020). *Seismic catalogues of the 2018–2019 volcano-seismic crisis offshore*
 586 *mayotte, comoro islands. v. 1.0 (october 2019). available at gfz data ser-*
 587 *vices*. Retrieved from <https://doi.org/10.5880/GFZ.2.1.2019.004> doi:
 588 10.5880/GFZ.2.1.2019.004
- 589 Cesca, S., Letort, J., Razafindrakoto, H. N., Heimann, S., Rivalta, E., Isken, M. P.,
 590 ... others (2020). Drainage of a deep magma reservoir near mayotte inferred
 591 from seismicity and deformation. *Nature Geoscience*, *13*(1), 87–93. doi:
 592 10.1038/s41561-019-0505-5
- 593 Chouet, B. (1986). Dynamics of a fluid-driven crack in three dimensions by the finite
 594 difference method. *Journal of Geophysical Research: Solid Earth*, *91*(B14),
 595 13967–13992. doi: 10.1029/JB091iB14p13967
- 596 Chouet, B. A., Page, R. A., Stephens, C. D., Lahr, J. C., & Power, J. A. (1994).
 597 Precursory swarms of long-period events at redoubt volcano (1989–1990),
 598 alaska: their origin and use as a forecasting tool. *Journal of Volcanology and*
 599 *Geothermal Research*, *62*(1-4), 95–135. doi: 10.1016/0377-0273(94)90030-2
- 600 Cruz, F. G., & Chouet, B. A. (1997). Long-period events, the most characteristic
 601 seismicity accompanying the emplacement and extrusion of a lava dome in
 602 galeras volcano, colombia, in 1991. *Journal of Volcanology and Geothermal*
 603 *Research*, *77*(1-4), 121–158. doi: 10.1016/S0377-0273(96)00091-1

- 604 Durran, D. R. (2013). *Numerical methods for wave equations in geophysical fluid dy-*
605 *namics* (Vol. 32). Springer Science & Business Media.
- 606 Fehler, M., & Aki, K. (1978). Numerical study of diffraction of plane elas-
607 tic waves by a finite crack with application to location of a magma lens.
608 *Bulletin of the Seismological Society of America*, *68*(3), 573–598. doi:
609 10.1785/BSSA0680030573
- 610 Ferrazzini, V., & Aki, K. (1987). Slow waves trapped in a fluid-filled infinite crack:
611 Implication for volcanic tremor. *Journal of Geophysical Research: Solid Earth*,
612 *92*(B9), 9215–9223. doi: 10.1029/JB092iB09p09215
- 613 Feuillet, N., Jorry, S., Crawford, W. C., Deplus, C., Thinon, I., Jacques, E.,
614 ... others (2021). Birth of a large volcanic edifice offshore mayotte via
615 lithosphere-scale dyke intrusion. *Nature Geoscience*, *14*(10), 787–795. doi:
616 10.1038/s41561-021-00809-x
- 617 Frehner, M. (2013). Krauklis wave initiation in fluid-filled fractures by a passing
618 body wave. In *Poromechanics v: Proceedings of the fifth biot conference on*
619 *poromechanics* (pp. 92–100). doi: 10.1061/9780784412992.011
- 620 Frehner, M., & Schmalholz, S. M. (2010). Finite-element simulations of stoneley
621 guided-wave reflection and scattering at the tips of fluid-filled fractures. *Geo-*
622 *physics*, *75*(2), T23–T36. doi: 10.1190/1.3340361
- 623 Fujita, E., & Ida, Y. (2003). Geometrical effects and low-attenuation reso-
624 nance of volcanic fluid inclusions for the source mechanism of long-period
625 earthquakes. *Journal of Geophysical Research: Solid Earth*, *108*(B2). doi:
626 10.1029/2002JB001806
- 627 Geubelle, P. H., & Rice, J. R. (1995). A spectral method for three-dimensional elas-
628 todynamic fracture problems. *Journal of the Mechanics and Physics of Solids*,
629 *43*(11), 1791–1824. doi: 10.1016/0022-5096(95)00043-I
- 630 Gordon, C., Webb, D. L., & Wolpert, S. (1992). One cannot hear the shape of a
631 drum. *Bulletin of the American Mathematical Society*, *27*(1), 134–138. doi: 10
632 .1090/S0273-0979-1992-00289-6
- 633 Gräff, D., Walter, F., & Lipovsky, B. P. (2019). Crack wave resonances within the
634 basal water layer. *Annals of Glaciology*, *60*(79), 158–166. doi: 10.1017/aog
635 .2019.8
- 636 Henry, F., Fokkema, J., & De Pater, C. (2002). Experiments on stoneley wave prop-

- 637 agation in a borehole intersected by a finite horizontal fracture. In *64th eage*
638 *conference & exhibition* (pp. cp-5). doi: 10.3997/2214-4609-pdb.5.P143
- 639 Jin, Y., Zheng, Y., Huang, L., & Ehlig-Economides, C. (2022). Characterizing
640 hydraulic fractures using the transient pressure surge effect. In *Spe/aapg/seg*
641 *unconventional resources technology conference* (p. D021S028R002). doi:
642 10.15530/urtec-2022-3718981
- 643 Kac, M. (1966). Can one hear the shape of a drum? *The american mathematical*
644 *monthly*, *73*(4P2), 1–23. doi: 10.1080/00029890.1966.11970915
- 645 Karimi-Fard, M., Durlofsky, L. J., & Aziz, K. (2004). An efficient discrete-fracture
646 model applicable for general-purpose reservoir simulators. *SPE journal*, *9*(02),
647 227–236. doi: 10.2118/88812-PA
- 648 Kawakatsu, H., Kaneshima, S., Matsubayashi, H., Ohminato, T., Sudo, Y., Tsutsui,
649 T., . . . Legrand, D. (2000). Aso94: Aso seismic observation with broadband
650 instruments. *Journal of Volcanology and Geothermal Research*, *101*(1-2),
651 129–154. doi: 10.1016/S0377-0273(00)00166-9
- 652 Korneev, V. (2008). Slow waves in fractures filled with viscous fluid. *Geophysics*,
653 *73*(1), N1–N7. doi: 10.1190/1.2802174
- 654 Korneev, V., Danilovskaya, L., Nakagawa, S., & Moridis, G. (2014). Krauklis wave
655 in a trilayer. *Geophysics*, *79*(4), L33–L39. doi: 10.1190/geo2013-0216.1
- 656 Krauklis, P. V. (1962). On some low-frequency oscillations of a fluid layer in an elas-
657 tic medium. *Prikl. Mat. Mekh.*, *26*(6), 1111–1115. doi: 10.1016/0021-8928(63)
658 90084-4
- 659 Kumagai, H., & Chouet, B. A. (1999). The complex frequencies of long-period seis-
660 mic events as probes of fluid composition beneath volcanoes. *Geophysical Jour-*
661 *nal International*, *138*(2), F7–F12. doi: 10.1046/j.1365-246X.1999.00911.x
- 662 Kumagai, H., & Chouet, B. A. (2000). Acoustic properties of a crack containing
663 magmatic or hydrothermal fluids. *Journal of Geophysical Research: Solid*
664 *Earth*, *105*(B11), 25493–25512. doi: 10.1029/2000JB900273
- 665 Kumagai, H., & Chouet, B. A. (2001). The dependence of acoustic properties of
666 a crack on the resonance mode and geometry. *Geophysical research letters*,
667 *28*(17), 3325–3328. doi: 10.1029/2001GL013025
- 668 Kumagai, H., Miyakawa, K., Negishi, H., Inoue, H., Obara, K., & Suetsugu, D.
669 (2003). Magmatic dike resonances inferred from very-long-period seismic

- 670 signals. *Science*, *299*(5615), 2058–2061. Retrieved from <http://science>
671 [.sciencemag.org/content/299/5615/2058](http://science.sciencemag.org/content/299/5615/2058) doi: 10.1126/science.1081195
- 672 Li, L., & Lee, S. H. (2008). Efficient field-scale simulation of black oil in a nat-
673 urally fractured reservoir through discrete fracture networks and homoge-
674 nized media. *SPE Reservoir evaluation & engineering*, *11*(04), 750–758. doi:
675 10.2118/103901-PA
- 676 Liang, C., Karlstrom, L., & Dunham, E. M. (2020). Magma oscillations in a
677 conduit-reservoir system, application to very long period (vlp) seismicity at
678 basaltic volcanoes: 1. theory. *Journal of Geophysical Research: Solid Earth*,
679 *125*(1), e2019JB017437. doi: 10.1029/2019JB017437
- 680 Liang, C., O’Reilly, O., Dunham, E. M., & Moos, D. (2017). Hydraulic fracture di-
681 agnostics from krauklis-wave resonance and tube-wave reflections. *Geophysics*,
682 *82*(3), D171–D186. doi: 10.1190/geo2016-0480.1
- 683 Liang, C., Peng, J., Ampuero, J.-P., Shauer, N., & Dai, K. (2023, August). *Dataset*
684 *for "Resonances in fluid-filled cracks of complex geometry and application*
685 *to very long period (VLP) seismic signals at Mayotte submarine volcano"*.
686 Zenodo. Retrieved from <https://doi.org/10.5281/zenodo.8275079> doi:
687 10.5281/zenodo.8275079
- 688 Lipovsky, B. P., & Dunham, E. M. (2015). Vibrational modes of hydraulic frac-
689 tures: Inference of fracture geometry from resonant frequencies and attenua-
690 tion. *Journal of Geophysical Research: Solid Earth*, *120*(2), 1080–1107. doi:
691 10.1002/2014JB011286
- 692 Lokmer, I., Saccorotti, G., Di Lieto, B., & Bean, C. J. (2008). Temporal evolution
693 of long-period seismicity at etna volcano, italy, and its relationships with the
694 2004–2005 eruption. *Earth and Planetary Science Letters*, *266*(1-2), 205–220.
695 doi: 10.1016/j.epsl.2007.11.017
- 696 Maeda, Y., & Kumagai, H. (2013). An analytical formula for the longitudinal res-
697 onance frequencies of a fluid-filled crack. *Geophysical Research Letters*, *40*(19),
698 5108–5112. doi: 10.1002/grl.51002
- 699 Maeda, Y., & Kumagai, H. (2017). A generalized equation for the resonance fre-
700 quencies of a fluid-filled crack. *Geophysical Journal International*, *209*(1), 192–
701 201. doi: 10.1093/gji/ggx019
- 702 McQuillan, M., & Karlstrom, L. (2021). Fluid resonance in elastic-walled englacial

- 703 transport networks. *Journal of Glaciology*, 67(266), 999–1012. doi: 10.1017/jog
704 .2021.48
- 705 Mercury, N., Lemoine, A., Doubre, C., Bertil, D., van Der Woerd, J., Hoste-
706 Colomer, R., & Battaglia, J. (2022). Onset of a submarine eruption east of
707 mayotte, comoros archipelago: the first ten months seismicity of the seismo-
708 volcanic sequence (2018–2019). *Comptes Rendus. Géoscience*, 354(S2), 105–
709 136. doi: 10.5802/crgeos.191
- 710 Métaxian, J.-P., Araujo, S., Mora, M., & Lesage, P. (2003). Seismicity related to the
711 glacier of cotopaxi volcano, ecuador. *Geophysical Research Letters*, 30(9). doi:
712 10.1029/2002GL016773
- 713 Mittal, T., Jordan, J. S., Retailleau, L., Beauducel, F., & Peltier, A. (2022). May-
714 otte 2018 eruption likely sourced from a magmatic mush. *Earth and Planetary
715 Science Letters*, 590, 117566. doi: 10.1016/j.epsl.2022.117566
- 716 Moifar, A., Varavei, A., Sepehrnoori, K., & Johns, R. T. (2013, 07). Develop-
717 ment of an Efficient Embedded Discrete Fracture Model for 3D Compositional
718 Reservoir Simulation in Fractured Reservoirs. *SPE Journal*, 19(02), 289-303.
719 doi: 10.2118/154246-PA
- 720 Nakagawa, S., Nakashima, S., & Korneev, V. A. (2016). Laboratory measurements
721 of guided-wave propagation within a fluid-saturated fracture. *Geophysical
722 Prospecting*, 64(1), 143–156. doi: 10.1111/1365-2478.12223
- 723 Nakano, M., & Kumagai, H. (2005). Response of a hydrothermal system to
724 magmatic heat inferred from temporal variations in the complex frequen-
725 cies of long-period events at kusatsu-shirane volcano, japan. *Journal of
726 volcanology and geothermal research*, 147(3-4), 233–244. doi: 10.1016/
727 j.jvolgeores.2005.04.003
- 728 Nikkhoo, M., & Walter, T. R. (2015). Triangular dislocation: an analytical, artefact-
729 free solution. *Geophysical Journal International*, 201(2), 1119–1141. doi: 10
730 .1093/gji/ggv035
- 731 Niu, J., & Song, T.-R. A. (2020). Real-time and in-situ assessment of conduit
732 permeability through diverse long-period tremors beneath aso volcano,
733 japan. *Journal of Volcanology and Geothermal Research*, 401, 106964. doi:
734 10.1016/j.jvolgeores.2020.106964
- 735 Okada, Y. (1985). Surface deformation due to shear and tensile faults in a half-

- 736 space. *Bulletin of the seismological society of America*, 75(4), 1135–1154.
- 737 Okada, Y. (1992). Internal deformation due to shear and tensile faults in a half-
738 space. *Bulletin of the Seismological Society of America*, 82(2), 1018–1040.
- 739 O'Reilly, O., Dunham, E. M., & Nordström, J. (2017). Simulation of wave propa-
740 gation along fluid-filled cracks using high-order summation-by-parts operators
741 and implicit-explicit time stepping. *SIAM Journal on Scientific Computing*,
742 39(4), B675–B702. Retrieved from <https://doi.org/10.1137/16M1097511>
743 doi: 10.1137/16M1097511
- 744 Paillet, F. L., & White, J. E. (1982, 08). Acoustic modes of propagation in
745 the borehole and their relationship to rock properties. *Geophysics*, 47(8),
746 1215–1228. Retrieved from <https://doi.org/10.1190/1.1441384> doi:
747 10.1190/1.1441384
- 748 Pointer, T., Liu, E., & Hudson, J. A. (1998). Numerical modelling of seismic
749 waves scattered by hydrofractures: application of the indirect boundary el-
750 ement method. *Geophysical Journal International*, 135(1), 289–303. doi:
751 10.1046/j.1365-246X.1998.00644.x
- 752 Retailleau, L., Saurel, J.-M., Laporte, M., Lavayssière, A., Ferrazzini, V., Zhu,
753 W., ... others (2022). Automatic detection for a comprehensive view of
754 mayotte seismicity. *Comptes Rendus. Géoscience*, 354(S2), 153–170. doi:
755 10.5802/crgeos.133
- 756 Rice, J. R. (1993). Spatio-temporal complexity of slip on a fault. *Journal of Geo-
757 physical Research: Solid Earth*, 98(B6), 9885–9907. doi: 10.1029/93JB00191
- 758 Rona, A. (2007). The acoustic resonance of rectangular and cylindrical cavities.
759 *Journal of Algorithms & Computational Technology*, 1(3), 329–356. doi:
760 10.1260/174830107782424110
- 761 Saurel, J.-M., Jacques, E., Aiken, C., Lemoine, A., Retailleau, L., Lavayssière, A.,
762 ... others (2021). Mayotte seismic crisis: building knowledge in near real-time
763 by combining land and ocean-bottom seismometers, first results. *Geophysical
764 Journal International*, 228(2), 1281–1293. doi: 10.1093/gji/ggab392
- 765 Segall, P. (2010). *Earthquake and volcano deformation*. Princeton University Press.
766 doi: 10.1515/9781400833856
- 767 Shauer, N., Desmond, K. W., Gordon, P. A., Liu, F., & Duarte, C. A. (2021). A
768 three-dimensional generalized finite element method for the simulation of wave

- 769 propagation in fluid-filled fractures. *Computer Methods in Applied Mechanics*
770 *and Engineering*, 386, 114136. doi: 10.1016/j.cma.2021.114136
- 771 Stuart, G., Murray, T., Brisbourne, A., Styles, P., & Toon, S. (2005). Seismic emis-
772 sions from a surging glacier: Bakaninbreen, svalbard. *Annals of Glaciology*, 42,
773 151–157. doi: 10.3189/172756405781812538
- 774 Sun, F., Gong, Y., & Dong, C. (2020). A novel fast direct solver for 3d elas-
775 tic inclusion problems with the isogeometric boundary element method.
776 *Journal of Computational and Applied Mathematics*, 377, 112904. doi:
777 10.1016/j.cam.2020.112904
- 778 Tang, X., & Cheng, C. (1988). Wave propagation in a fluid-filled fracture—an exper-
779 imental study. *Geophysical Research Letters*, 15(13), 1463–1466. doi: 10.1029/
780 GL015i013p01463
- 781 Tang, X., & Cheng, C. (1989). A dynamic model for fluid flow in open borehole frac-
782 tures. *Journal of Geophysical Research: Solid Earth*, 94(B6), 7567–7576. doi:
783 10.1029/JB094iB06p07567
- 784 Tary, J.-B., Van der Baan, M., & Eaton, D. W. (2014). Interpretation of
785 resonance frequencies recorded during hydraulic fracturing treatments.
786 *Journal of Geophysical Research: Solid Earth*, 119(2), 1295–1315. doi:
787 10.1002/2013JB010904
- 788 Xu, Y., Cavalcante Filho, J., Yu, W., & Sepehrnoori, K. (2017). Discrete-
789 fracture modeling of complex hydraulic-fracture geometries in reservoir sim-
790 ulators. *SPE Reservoir Evaluation & Engineering*, 20(02), 403–422. doi:
791 10.2118/183647-PA
- 792 Yamamoto, M., & Kawakatsu, H. (2008). An efficient method to compute the
793 dynamic response of a fluid-filled crack. *Geophysical Journal International*,
794 174(3), 1174–1186. doi: 10.1111/j.1365-246X.2008.03871.x
- 795 Zheng, Y., Malallah, A. H., Fehler, M. C., & Hu, H. (2016). 2d full-waveform model-
796 ing of seismic waves in layered karstic media. *Geophysics*, 81(2), T25–T34. doi:
797 10.1190/geo2015-0307.1

798 **Appendix A Matrices \mathbf{D} and \mathbf{T} for a simple crack intersection**

799 In this section, we show step by step how to construct matrices \mathbf{D} and \mathbf{T} for a sim-
800 ple crack intersection shown in Figure A1. The element number and positive flux direc-

801 tion of each active connection as labeled. The boundary edges have zero flux and they
 802 do not contribute to \mathbf{D} and \mathbf{T} . Thus, we have five elements and five active connections
 803 numbered as $\{2 \rightarrow 1, 3 \rightarrow 2, 4 \rightarrow 2, 5 \rightarrow 2, 5 \rightarrow 4\}$, where $i \rightarrow j$ defines the positive flux
 direction. The size of both \mathbf{D} and \mathbf{T} are 5 by 5.

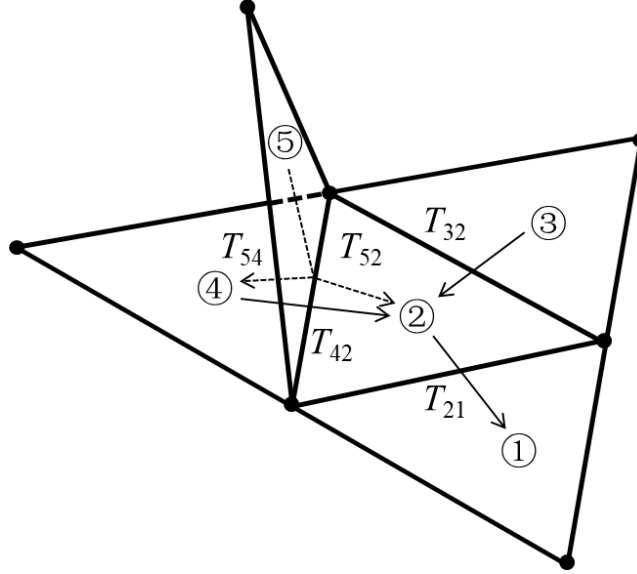


Figure A1. Geometry of a simple crack intersection. The element number and the positive flow direction of each active connection (non-zero flux) are indicated by the circled number and arrow, respectively. The scalar transmissibilities are labeled near each connection.

804

805 Let's first consider the matrix \mathbf{D} , which sums the flux from active connections to
 806 obtain the net out-flux from each element. We consider the first row of \mathbf{D} as an exam-
 807 ple, relevant for element 1. The only connection that contributes to the net out-flux of
 808 element 1 is connection 1 with the positive direction of $2 \rightarrow 1$, the opposite to the out-
 809 flux direction. Thus, $D(1, 1) = -1$ and other entries of the first row are zeros. How-
 810 ever, for element 2, the positive flux of connection 1 aligns with the outflux direction,
 811 which leads to $D(2, 1) = 1$. Similarly, other entries of matrix \mathbf{D} can be determined and
 812 the matrix \mathbf{D} is:

$$\mathbf{D} = \begin{bmatrix} -1 & 0 & 0 & 0 & 0 \\ 1 & -1 & -1 & -1 & 0 \\ 0 & 1 & 0 & 0 & 0 \\ 0 & 0 & 1 & 0 & -1 \\ 0 & 0 & 0 & 1 & 1 \end{bmatrix}. \quad (\text{A1})$$

813 We now proceed to construct the matrix \mathbf{T} , which computes the flux on each active con-
 814 nection from the pressure on each cell. Note that we only store the flux in the positive
 815 direction. For instance, the flux on the first connection is $Q_{2 \rightarrow 1} = T_{21} (p_2 - p_1)$, which
 816 means $T(1, 2) = -T(1, 1) = T_{21}$. Similarly, other entries of the matrix \mathbf{T} can be com-
 817 puted and the full expression of \mathbf{T} is:

$$\mathbf{T} = \begin{bmatrix} -T_{21} & T_{21} & 0 & 0 & 0 \\ 0 & -T_{32} & T_{32} & 0 & 0 \\ 0 & -T_{42} & 0 & T_{42} & 0 \\ 0 & -T_{52} & 0 & 0 & T_{52} \\ 0 & 0 & 0 & -T_{54} & T_{54} \end{bmatrix}. \quad (\text{A2})$$

818 **Appendix B Resonant frequencies from time domain results by GFEM**

819 In this section, we explain the procedure to obtain selective resonant frequencies
 820 from the time domain simulation results using the GFEM code developed by Shauer et
 821 al. (2021). As shown in Figure B1, we apply injection sources with a gaussian source time
 822 function on the certain position on the crack (red stars), obtain the pressure time series
 823 (duration of 50 s) on three receiving points (blue triangles), and then extract the res-
 824 onant frequencies at spectral peaks. For the rectangular crack, we place one source at
 825 the upperleft corner, which manages to excite all the first eight modes, and three receivers
 826 (R1, R2, and R3) at $(-0.5, 0)$, $(-0.20, 0.25)$, and $(0, 0.25)$, respectively. Different receivers
 827 sample different eigenmodes. For instance, receiver R1 samples modes 1, 2, 5, and 8 as
 828 shown in Figure B1-c. The modes sampled by R2 and R3 are shown in Table 2. We make
 829 this choice to selectively sample closely-spaced modes, for instance mode 2 and 3, at dif-
 830 ferent receivers to avoid ambiguity.

831 For the elliptical crack, we place two sources at the leftmost and uppermost ends,
 832 and three receivers at $(-0.5, 0)$, $(0, 0.25)$, $(0, 0)$ respectively. Due to the excitation and
 833 monitoring geometry, we focus only sampling the longitudinal and transverse modes, which
 834 are clearly seperated peaks in the spectrum. The eigenmodes sampled by different re-
 835 ceivers are shown in Figure B1-f and Table 3.

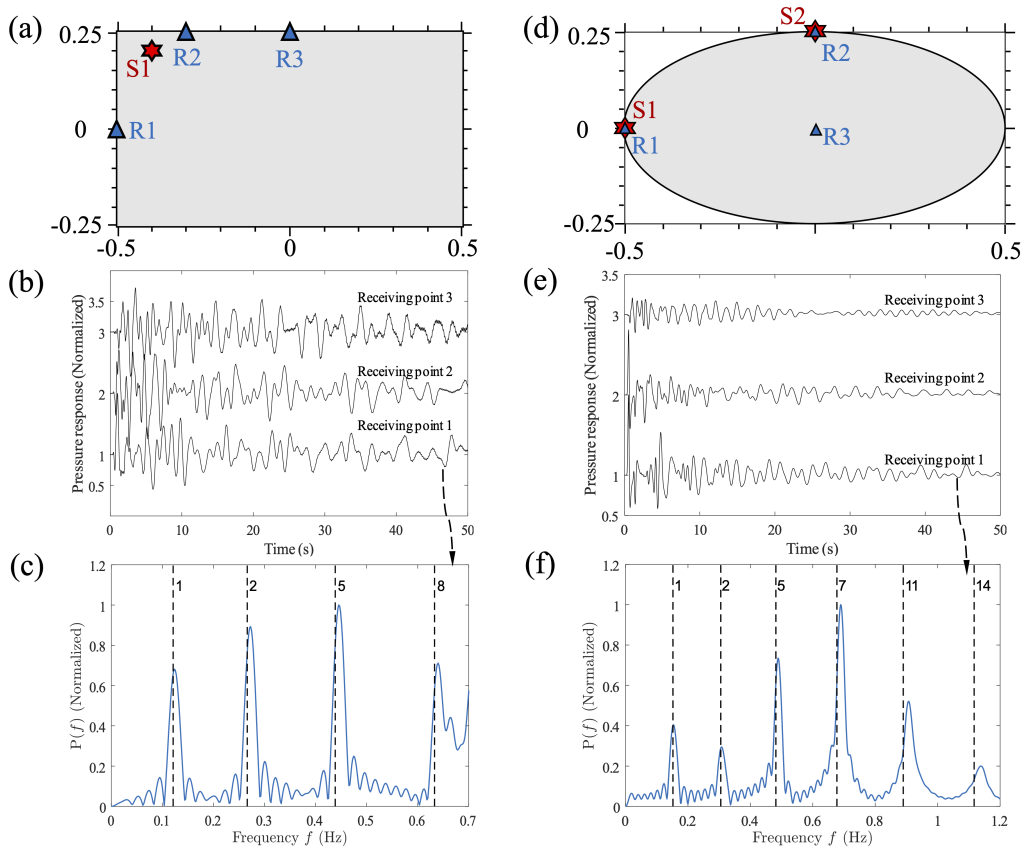


Figure B1. (a, d) The source and receiver positions. (b, e) Pressure time series at three receivers. (c, f) The normalized spectral amplitude of data at receiver R1. The vertical black dashed lines are the resonant frequencies (with mode number labelled) computed by BEM+FVM method.

1 **Resonances in fluid-filled cracks of complex geometry**
2 **and application to very long period (VLP) seismic**
3 **signals at Mayotte submarine volcano**

4 **Chao Liang**¹, **Junjun Peng**¹, **Jean-Paul Ampuero**², **Nathan Shauer**³,
5 **Kaoshan Dai**¹

6 ¹Institute for Disaster Management and Reconstruction (IDMR), Sichuan University, 610207, Chengdu,
7 China

8 ²Géoazur, Université Côte d'Azur (UCA), IRD, CNRS, Observatoire de la Côte d'Azur, 06560, Valbonne,
9 France

10 ³LabMeC-FECFAU-State University of Campinas, R. Josiah Willard Gibbs 85, Cidade Universitaria,
11 Campinas, 13083-839, SP, Brazil

12 **Key Points:**

- 13 • Hybrid method combining BEM and FVM efficiently computes resonant frequen-
14 cies of complex-shaped fluid-filled cracks
- 15 • Elliptical crack shares similar modes with rectangular crack but a crack network
16 produces more complex resonances
- 17 • A dumbbell-shaped crack explains ratio of first two modes (~ 2.5) in the VLP seis-
18 mic signal at Mayotte submarine volcano

Corresponding author: Chao Liang, chao.liang@scu.edu.cn

Corresponding author: Kaoshan Dai, kdai@scu.edu.cn

Abstract

Fluid-filled cracks sustain a slow guided wave (Krauklis wave or crack wave) whose resonant frequencies are widely used for interpreting long period (LP) and very long period (VLP) seismic signals at active volcanoes. Significant efforts have been made to model this process using analytical developments along an infinite crack or numerical methods on simple crack geometries. In this work, we develop an efficient hybrid numerical method for computing resonant frequencies of complex-shaped fluid-filled cracks and networks of cracks and apply it to explain the ratio of spectral peaks in the VLP signals from the Fani Maoré submarine volcano that formed in Mayotte in 2018. By coupling triangular boundary elements and the finite volume method, we successfully handle complex geometries and achieve computational efficiency by discretizing solely the crack surfaces. The resonant frequencies are directly determined through eigenvalue analysis. After proper verification, we systematically analyze the resonant frequencies of rectangular and elliptical cracks, quantifying the effect of aspect ratio and crack stiffness ratio. We then discuss theoretically the contribution of fluid viscosity and seismic radiation to energy dissipation. Finally, we obtain a crack geometry that successfully explains the characteristic ratio between the first two modes of the VLP seismic signals from the Fani Maoré submarine volcano in Mayotte. Our work not only reveals rich eigenmodes in complex-shaped cracks but also contributes to illuminating the subsurface plumbing system of active volcanoes. The developed model is readily applicable to crack wave resonances in other geological settings, such as glacier hydrology and hydrocarbon reservoirs.

1 Introduction

Slow guided waves that propagate along fluid-filled cracks, named crack waves or Krauklis waves, can be used for inferring the geometries of subsurface cracks and the fluid properties in a wide range of geological settings (Krauklis, 1962; Ferrazzini & Aki, 1987; Paillet & White, 1982; B. Chouet, 1986; Korneev, 2008; Tang & Cheng, 1989; Lipovsky & Dunham, 2015). In volcanology, crack wave resonances along magma-filled sills and dikes have been used for interpreting long period (LP, 0.5-2 s) and very long period (VLP, 2 to 100 s) seismic signals at many volcanos, including Mount Redoubt (B. A. Chouet et al., 1994), Aso (Kawakatsu et al., 2000; Niu & Song, 2020), Galeras (Cruz & Chouet, 1997), Asama (Fujita & Ida, 2003), Kusatsi-Shirane (Kumagai et al., 2003; Nakano & Kumagai, 2005), Etna (Lokmer et al., 2008), and Erebus (Aster, 2019). Crack waves (and

51 their induced tube waves in wellbores) are used for diagnosing the fracture geometries
 52 in unconventional hydrocarbon reservoirs (Henry et al., 2002; Tary et al., 2014; Lipovsky
 53 & Dunham, 2015; Liang et al., 2017). The resonating or humming signals in glaciers have
 54 also been attributed to crack waves (Métaxian et al., 2003; Stuart et al., 2005; Gräff et
 55 al., 2019; McQuillan & Karlstrom, 2021). Natural cracks in the subsurface are complex
 56 in shape and usually form an inter-connected network. Therefore, efficient methods for
 57 computing resonant modes of single cracks and networks of cracks are necessary for in-
 58 terpreting frequencies measured in the field.

59 Since its first discovery by Krauklis (1962), crack waves have been studied analytically
 60 (Aki et al., 1977; Ferrazzini & Aki, 1987; Korneev, 2008; Lipovsky & Dunham, 2015),
 61 experimentally (Tang & Cheng, 1988; Nakagawa et al., 2016; Cao et al., 2021), and nu-
 62 merically by various methods (e.g., B. Chouet, 1986; Yamamoto & Kawakatsu, 2008;
 63 Frehner & Schmalholz, 2010; O’Reilly et al., 2017; Liang et al., 2020; Shauer et al., 2021;
 64 Jin et al., 2022). Analytically derived dispersion relations are useful for understanding
 65 the propagation behavior but are meant for an infinitely long crack and do not account
 66 for the restriction of the finite crack tip. The finite difference method (FDM) is normally
 67 based on cartesian grids in 2D (Fehler & Aki, 1978) or 3D (B. Chouet, 1986; Liang et
 68 al., 2020) and limited to a tabular crack shape. Maeda and Kumagai (2013) and Maeda
 69 and Kumagai (2017) performed a large number of numerical simulations on rectangu-
 70 lar cracks using a FDM simulator developed by B. Chouet (1986). With that, they ob-
 71 tained a set of empirical fitting formulas for resonant frequencies given the crack aspect
 72 ratio α and stiffness ratio $C_L = K_f L / (G w_0)$, where K_f is the fluid bulk modulus, G
 73 the solid shear modulus, L the crack length and w_0 the crack aperture. However, such
 74 relations only apply to longitudinal or transverse modes on rectangular cracks (Maeda
 75 & Kumagai, 2013, 2017). Notably, O’Reilly et al. (2017) simulated a non-planar fluid-
 76 filled crack using FDM on a curvilinear grid and adopted a lubrication-type approxima-
 77 tion in the fluid (Lipovsky & Dunham, 2015), neglecting fluid acoustics in the crack width
 78 direction while resolving the narrow viscous boundary layer close to the crack wall. This
 79 treatment removes the time step restriction introduced by extremely fine mesh size in
 80 the crack width direction and accelerates the computation. However, their work was lim-
 81 ited to 2D geometries. The finite element method (FEM) is more flexible for handling
 82 complex crack geometries and has been used to study crack waves in 2D (Frehner & Schmal-
 83 holz, 2010; Frehner, 2013) and 3D (Shauer et al., 2021). Particularly, Shauer et al. (2021)

84 produced the first simulation of an elliptical fluid-filled crack using the generalized finite
85 element method (GFEM). However, similar to FDM, FEM needs to discretize the vol-
86 ume, which results in a large number of elements and high computational cost. On the
87 other hand, the boundary element method (BEM) reduces the simulation space from a
88 domain to boundary surfaces, drastically decreasing the number of degrees of freedom,
89 and has been used to study waves in fluid-filled cracks (Yamamoto & Kawakatsu, 2008;
90 Pointer et al., 1998; Jin et al., 2022) and other inclusions (Zheng et al., 2016; Sun et al.,
91 2020). However, previous BEM simulations are either in two dimensions or focus on the
92 wave diffraction instead of analyzing the resonant frequencies. Currently, the study of
93 resonant frequencies of complex-shaped fluid-filled cracks and crack networks in three
94 dimensions remain unknown.

95 In this work, we propose an efficient hybrid numerical method to simulate crack
96 wave resonance in complex-shaped cracks or crack networks filled with an inviscid fluid,
97 by coupling the boundary element method (BEM) for the solid response and the finite
98 volume method (FVM) for acoustics in the fluid. By using triangular elements in both
99 BEM and FVM on the crack surfaces, we successfully handle complex crack shapes and
100 intersections. We restrict our attention to the low frequency limit where the crack wave
101 is much slower than the solid body waves, such that the solid response can be approx-
102 imated as quasi-static (Korneev, 2008; Lipovsky & Dunham, 2015; Liang et al., 2020).
103 An eigenvalue analysis is performed to extract the resonant modes directly in the fre-
104 quency domain, circumventing errors from time discretization and spectral analysis of
105 the time domain simulation data. We first verify our method by comparing results with
106 analytical solutions in the rigid wall limit and with numerical solutions from existing meth-
107 ods for both a rectangular (B. Chouet, 1986; Maeda & Kumagai, 2017) and elliptical cracks
108 (Shauer et al., 2021). An example is then provided to demonstrate the simulation ca-
109 pability for intersecting cracks. The effect of crack aspect ratio and stiffness ratio on res-
110 onant frequencies (longitudinal, transverse, and mixed modes) is systematically inves-
111 tigated for both rectangular and elliptical cracks. Although our current model does not
112 include viscous or radiation loss, we provide some theoretical discussion on these effects
113 under simple assumptions (boundary layer limit and quasi-dynamic approximation). Fi-
114 nally, we present a crack shape compatible with the first two spectral peaks of VLP seis-
115 mic signals from the Fani Maoré, Mayotte submarine volcano and discuss the potential
116 of the methodology for future applications in volcanology and other geological settings.

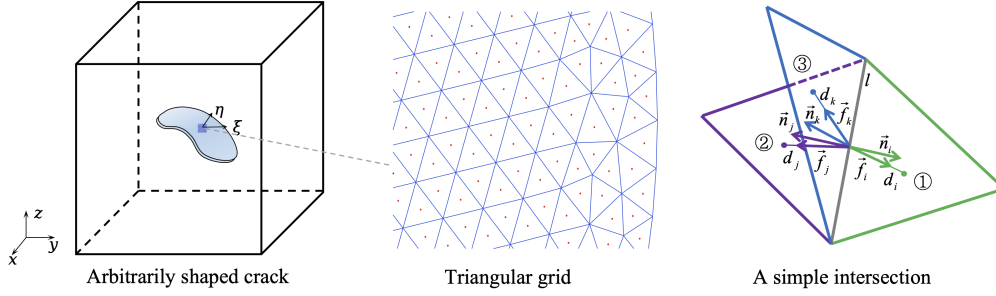


Figure 1. Schematics of an arbitrarily-shaped fluid-filled crack, its spatial discretization (with unknown variables placed in the element centroids, red dots), and a zoom-in view at an intersection between two cracks.

2 Methods

In this section, we present the governing equations, discretization, and eigenmode analysis for computing the resonant frequencies.

2.1 Governing equations

We consider the oscillation of inviscid fluids in complex-shaped thin cracks embedded in a 3D homogeneous linear elastic solid (Figure 1). The initial opening of the crack is w_0 , which is assumed to be a constant and much smaller than the wavelength λ . We adopt a similar lubrication approximation as B. Chouet (1986), Yamamoto and Kawakatsu (2008) and O'Reilly et al. (2017), and treat the fluid pressure and velocities as uniform in the crack thickness direction, reducing the crack from a 3D body to a 2D surface S . Following O'Reilly et al. (2017), we consider a small crack curvature so that its effect on the fluid momentum balance is negligible. Thus, the mass and momentum balance of the fluid on the crack surface are written as

$$\frac{1}{w_0} \frac{\partial w}{\partial t} + \frac{1}{K_f} \frac{\partial p}{\partial t} + \frac{\partial v_\xi}{\partial \xi} + \frac{\partial v_\eta}{\partial \eta} = 0, \quad (1)$$

$$\rho_f \frac{\partial v_\xi}{\partial t} + \frac{\partial p}{\partial \xi} = 0, \quad (2)$$

$$\rho_f \frac{\partial v_\eta}{\partial t} + \frac{\partial p}{\partial \eta} = 0, \quad (3)$$

where ρ_f and K_f are fluid density and bulk modulus, w is the crack opening perturbation, p is the fluid pressure perturbation, t is time, and ξ and η are two locally perpen-

134 dicular coordinates tangent to the crack surface, v_ξ and v_η are the fluid velocities in the
 135 ξ and η directions, respectively. Eliminating v_ξ and v_η in (1) using (2)-(3), we have

$$\rho_f \left(\frac{1}{w_0} \frac{\partial^2 w}{\partial t^2} + \frac{1}{K_f} \frac{\partial^2 p}{\partial t^2} \right) - \Delta p = 0, \quad (4)$$

136 where $\Delta = \frac{\partial^2}{\xi^2} + \frac{\partial^2}{\eta^2}$ is the tangential Laplace operator along the crack surface. The
 137 coupling between fluid and solid is encapsulated in the relation between the crack open-
 138 ing perturbation w and pressure perturbation p , which must balance the solid normal
 139 stress perturbation σ_n on the crack wall (assumed positive in compression). Since we fo-
 140 cus on the low frequency limit, the solid response is approximately quasi-static (Korneev,
 141 2008; Lipovsky & Dunham, 2015; Liang et al., 2020), and p for a linear elastic solid can
 142 be expressed as (Segall, 2010):

$$p(x) = \int_S K(x, \xi) w(\xi) dA, \quad (5)$$

143 where $K(x, \xi)$ is the Green's function that relates a unit open dislocation impulse at ξ
 144 to the normal stress change at x . The expressions of K in an elastic whole space and half
 145 space are available analytically for a uniform dislocation on both rectangular elements
 146 (Okada, 1985, 1992) and triangular elements (Nikkhoo & Walter, 2015).

147 **2.2 Discretization**

148 We discretize the crack surfaces into N_e triangular elements. The unknown aver-
 149 age pressures $\bar{\mathbf{p}}$ and openings $\bar{\mathbf{w}}$, placed at element centroids (as shown in Figure 1), are
 150 related by

$$\bar{\mathbf{p}} = \mathbf{K}\bar{\mathbf{w}}, \quad (6)$$

151 where \mathbf{K} is a N_e by N_e matrix and $K(i, j)$ denotes the fluid pressure (or solid normal
 152 stress) change at the centroid of the i -th element caused by a unit open dislocation on
 153 the j -th element. We use the full space Green's function in this study but one can also
 154 use the half space solution.

155 We then discretize the tangential Laplacian operator by a finite volume scheme with
 156 a two-point flux (TPF) approximation following Karimi-Fard et al. (2004), which has
 157 been widely used for diffusive flows through a discrete fracture network in hydrocarbon
 158 reservoirs (e.g., Li & Lee, 2008; Moinfar et al., 2013; Xu et al., 2017; Berre et al., 2019).
 159 This scheme is only first-order accurate and is thus rarely used in wave propagation prob-
 160 lems due to the strong numerical diffusion in time domain simulations (e.g., Durran, 2013).

161 However, it is a sufficient scheme for our problem as we focus on resolving only the spa-
 162 tial distribution of eigenmodes in the frequency domain and the low order of accuracy
 163 can be remedied by using more elements. Here, we briefly present the key derivation steps
 164 and the readers are referred to Karimi-Fard et al. (2004) for a detailed description.

165 We consider an arbitrary planar triangular element i with a surface S_i and bound-
 166 ary edges l_{ij} , where j is the index of the neighboring elements. Each i and j pair forms
 167 a hydraulic connection. When multiple cracks intersect, multiple connections share the
 168 same edge. We integrate equation (4) over each element i 's surface, leading to:

$$\rho_f A_i \left[\frac{1}{w_0} \frac{\partial^2 \bar{w}_i}{\partial t^2} + \frac{1}{K_f} \frac{\partial^2 \bar{p}_i}{\partial t^2} \right] = \int_{S_i} \Delta p ds, \quad (7)$$

169 where

$$\bar{p}_i = \frac{1}{A_i} \int_{S_i} p ds, \quad (8)$$

170

$$\bar{w}_i = \frac{1}{A_i} \int_{S_i} w ds, \quad (9)$$

171 are the average pressure and opening of element i , respectively. Applying the divergence
 172 theorem to the right hand side of equation (7), we have:

$$\int_{S_i} \Delta p ds = \int_{S_i} \vec{\nabla} \cdot \vec{\nabla} p ds = \int_l \frac{\partial p}{\partial n} dl = - \sum_{j=1}^{n_c} D_{i \rightarrow j} Q_{i \rightarrow j}, \quad (10)$$

173 where $\partial p / \partial n$ is the pressure gradient normal to the boundary edges, n_c is the total num-
 174 ber of connections in contact with element i , $Q_{i \rightarrow j}$ is the flux going out from element
 175 i to element j . Since $Q_{i \rightarrow j} = -Q_{j \rightarrow i}$, we only store $Q_{i \rightarrow j}$ for each (i, j) pair and its
 176 positive flux direction is pre-defined by an indicator function $I_{i \rightarrow j} = -I_{j \rightarrow i} = 1$. $D_{i \rightarrow j}$
 177 is the discrete divergence operator and $D_{i \rightarrow j} = I_{i \rightarrow j} = 1$.

178 The assumption of the TPF scheme is to approximate the flux term in the follow-
 179 ing form (equation (7) in Karimi-Fard et al. (2004)):

$$Q_{i \rightarrow j} = I_{i \rightarrow j} T_{ij} (p_i - p_j), \quad (11)$$

180 where p_i and p_j are pressures defined at the centroids of the two neighboring elements.

181 T_{ij} is the scalar transmissibility and is expressed as

$$T_{ij} = \frac{\alpha_i \alpha_j}{\sum_{k=1}^{n_c} \alpha_k}, \quad (12)$$

182

$$\alpha_k = \frac{l_{ij}}{d_k} \vec{n}_k \cdot \vec{f}_k, \quad (13)$$

183 where l_{ij} is the length of the connecting edge, d_k and \vec{f}_k are the length and unit direc-
 184 tional vector from midpoint of the edge to the centroid of element k , \vec{n}_k is a unit nor-
 185 mal vector perpendicular to the edge and pointing towards element k , as shown in Fig-
 186 ure 1. Fluxes on the crack boundaries are set to zero. Combining equations (10) and (11),
 187 we have:

$$\int_{S_i} \Delta p ds = - \sum_{j=1}^{n_c} D_{i \rightarrow j} I_{i \rightarrow j} T_{ij} (p_i - p_j). \quad (14)$$

188 It is apparent that changing the positive flux direction from $i \rightarrow j$ to $j \rightarrow i$ flips the
 189 sign of both $D_{i \rightarrow j}$ and $I_{i \rightarrow j}$ and thus results in the same Laplacian term. Substituting
 190 equation (14) into equation (7) and rewriting in the matrix form, we have the spatially
 191 discretized equation without external forcing:

$$\rho_f \left(\frac{1}{w_0} \mathbf{K}^{-1} + \frac{1}{K_f} \right) \frac{\partial^2 \bar{\mathbf{p}}}{\partial t^2} = -\mathbf{A}^{-1} \mathbf{D} \mathbf{Q} = -\mathbf{A}^{-1} \mathbf{D} \mathbf{T} \bar{\mathbf{p}}, \quad (15)$$

192 where \mathbf{A} is a diagonal matrix of size N_e by N_e denoting the area of each element, $\mathbf{Q} =$
 193 $\mathbf{T} \bar{\mathbf{p}}$ is the flux vector whose size is the total number of connections N_c , \mathbf{T} is the trans-
 194 missibility matrix (including the indicator function) of size N_c by N_e that maps the vec-
 195 tor $\bar{\mathbf{p}}$ to \mathbf{Q} , and \mathbf{D} is the divergence matrix of size N_e by N_c that maps \mathbf{Q} to the net flux
 196 out of each element. The structure of matrices \mathbf{D} and \mathbf{T} for a system of three intersect-
 197 ing crack elements are described in Appendix A.

198 We further introduce the following dimensionless quantities:

$$\mathbf{K}^* = \mathbf{K}/(G/L), \mathbf{A}^* = \mathbf{A}/L^2, w = w^*/w_0, t^* = t/(L/c_l), \bar{\mathbf{p}}^* = \bar{\mathbf{p}}/(\rho_f c_l^2), \quad (16)$$

199 where G is the solid shear modulus, L is a representative length of the crack and $c_l =$
 200 $\sqrt{Gw_0}/(\rho_f L)$ is a representative crack wave speed. Different non-dimensionalization strate-
 201 gies exist, such as the one by B. Chouet (1986) which normalizes wave speeds by the solid
 202 compressional wave speed c_p . We choose c_l instead, because in the long wavelength limit,
 203 where compliance of the crack dominates, this choice conveniently results in a fundamen-
 204 tal frequency of the order of unity. The nondimensionalised equation is

$$\left(\frac{1}{C_L} \mathbf{I} + (\mathbf{K}^*)^{-1} \right) \frac{\partial^2 \bar{\mathbf{p}}^*}{\partial t^{*2}} = -\mathbf{A}^{*-1} \mathbf{D} \mathbf{T} \bar{\mathbf{p}}^*, \quad (17)$$

205 where $C_L = K_f L / G w_0$ is the key dimensionless parameter, named crack stiffness ra-
 206 tio by B. Chouet (1986). The crack wave limit is achieved with $C_L \gg 1$, where the crack
 207 is much more compliant than the fluid. C_L can be related to the representative crack
 208 wave speed c_l by $C_L = c_f^2 / c_l^2$, where c_f is the fluid acoustic wave speed. The crack topol-

209 ogy (for instance, the aspect ratio α for a rectangular or elliptical crack) and solid Pois-
 210 son's ratio ν_s are encapsulated into the dimensionless stiffness matrix \mathbf{K}^* . The solid Pois-
 211 son's ratio is set to 0.25 throughout this manuscript, unless otherwise mentioned.

212 **2.3 Eigenmode analysis**

213 We directly obtain the resonant frequencies through eigenmode analysis in the fre-
 214 quency domain. The spatially discretized dimensionless equation is written as

$$\frac{\partial^2 \bar{\mathbf{p}}^*}{\partial t^{*2}} = -\mathbf{B} \bar{\mathbf{p}}^*, \quad (18)$$

215 where

$$\mathbf{B} = \left(\frac{1}{C_L} \mathbf{I} + (\mathbf{K}^*)^{-1} \right)^{-1} \mathbf{A}^{*-1} \mathbf{D} \mathbf{T}. \quad (19)$$

216 The nondimensionalised Fourier transform is defined as

$$\hat{u}(\omega^*) = \int_{-\infty}^{+\infty} u(t^*) e^{i\omega^* t^*} dt^*, \quad (20)$$

217 where

$$\omega^* = \omega / (c_l / L), \quad (21)$$

218 is the dimensionless angular frequency. The dimensionless frequency is

$$f^* = \omega^* / (2\pi) = f / (c_l / L). \quad (22)$$

219 Taking the Fourier transform of equation (18), we have:

$$(\omega^*)^2 \hat{\mathbf{p}} = \mathbf{B} \hat{\mathbf{p}}, \quad (23)$$

220 where $(\omega^*)^2$ and $\hat{\mathbf{p}}$ are the eigenvalues and eigenvectors of the real matrix \mathbf{B} . Since we
 221 deal with inviscid fluids, we only seek real positive eigenvalues, which correspond to un-
 222 damped oscillatory modes. The resulting eigenvectors determine the spatial distribution
 223 of the pressure on the crack surface. Solving the resonant frequencies in dimensionless
 224 form is advantageous, because one can easily scale the solution to other parameters, such
 225 as crack length, crack width and solid stiffness, given the same dimensionless parame-
 226 ters, C_L , ν_s and crack topology.

227 **3 Verification and examples**

228 In this section, we first verify our implementation by comparing our results to an-
 229alytical solutions in the rigid solid limit and numerical solutions from existing studies.

230 We then present an example of simple intersecting crack geometry to demonstrate the
 231 utility of our method.

Table 1. The error between the theoretical and numerical resonant frequencies for the first 16 modes

Mode	Theoretical value	Numerical value	Error (%)
1	0.5000	0.5004	0.074
2	0.8333	0.8325	0.105
3	0.9718	0.9706	0.127
4	1.0000	1.0008	0.078
5	1.3017	1.3018	0.009
6	1.5000	1.5010	0.066
7	1.6667	1.6647	0.118
8	1.7159	1.7172	0.072
9	1.7401	1.7370	0.175
10	1.9437	1.9413	0.122
11	2.0000	2.0014	0.068
12	2.1667	2.1693	0.123
13	2.2423	2.2409	0.060
14	2.5000	2.4954	0.184
15	2.5000	2.5010	0.042
16	2.5495	2.5426	0.270

232 3.1 Comparison with analytical solutions in a rigid solid

233 We compute the \mathbf{K} matrix using the subroutines developed by Nikkhoo and Wal-
 234 ter (2015), which have been extensively used by other studies. The bulk part that needs
 235 to be validated is the FVM discretization of the Laplacian term. For that, we set solid
 236 rigidity to infinity and compare the numerical results to the analytical solution of the
 237 resonant frequencies of linear acoustic waves in a 2D rectangular domain with zero-flux
 238 boundaries (Rona, 2007). The solution is in a dimensionless form with a rectangular do-
 239 main of size 1 by 0.5 and a wave speed of 1. The comparison results for the first 16 modes
 240 are tabulated in Table 1. The excellent agreement between our numerical results and the

analytical solutions, with relative differences smaller than 0.2%, verifies our FVM discretization of the Laplacian term.

3.2 Comparison to numerical solutions by existing studies

We compare solutions by our method (BEM+FVM) to those by B. Chouet (1986), Maeda and Kumagai (2017) and Shauer et al. (2021). With B. Chouet (1986) and Maeda and Kumagai (2017), we compare resonant frequencies of longitudinal modes for a rectangular crack for various values of C_L (5, 15, 25, 50, 75, 100). With the GFEM by Shauer et al. (2021), we compare solutions of multiple modes on both rectangular and elliptical cracks. The eigenmodes can be straightforwardly classified as longitudinal (variation only along the major crack axis), transverse (variation only along the minor crack axis), and mixed modes for a rectangular crack, but less so for an elliptical crack. Since the method by Shauer et al. (2021) discretizes the problem in time and, therefore, does not readily provide resonant frequencies, we ran their code to excite the fluid oscillation on the crack with $C_L = 100$ by a point injection source and then extract the resonant frequencies from the spectral peaks of the pressure records at a few receiving points. We use a Gaussian time function for the injection source $f(t) = \exp\left(-(t - t_c)^2/T^2\right)$ with $t_c = 0.5$, $T = 0.1$, to ensure a smooth start and a sufficiently wide spectrum to cover enough eigenmodes. Note that if either excitation or receiving points are placed on the nodal line, the eigenmode can not be excited or recorded. Therefore, not all eigenmodes are excited in the time domain simulation and we also only compare selective modes with Shauer et al. (2021), which is sufficient for verification purposes. The detailed geometries and simulation data are presented in Appendix B. Notably, the code of Shauer et al. (2021) has the capability of both considering (fully dynamic, FD) or neglecting the solid inertia (quasi-static, QS), allowing to investigate the impact of the solid inertia on crack wave resonant frequencies.

Tables 2 and 3 show the comparison of dimensionless resonant frequencies of selective eigenmodes from the GFEM program by Shauer et al. (2021) with those by our method for a rectangular and elliptical crack, respectively, with an aspect ratio of 0.5, major axis length of 1, and C_L of 100. The relative difference between our results and those from Shauer et al. (2021) are near 2% or less, with or without solid inertia. This close agreement not only demonstrates the validity of our approach but also reassures that the quasi-static solid response is a very good approximation when computing the

Table 2. Resonant frequencies by BEM+FVM and GFEM with or without inertia (FD or QS), rectangular crack

Mode	Resonant frequencies detected at receiving points by GFEM						BEM+FVM	Error FD (%)	Error QS (%)
	(-0.5, 0)		(-0.2, 0.25)		(0, 0.25)				
	FD	QS	FD	QS	FD	QS			
1	1.236	1.236	1.236	1.236			1.210	2.15	2.15
2	2.727	2.691					2.662	2.44	1.09
3			2.890	2.873	2.818	2.782	2.835	1.94	1.34
4			3.453	3.418			3.373	2.37	1.33
5	4.454	4.400	4.436	4.382			4.385	1.57	0.34
6					4.526	4.491	4.466	1.34	0.56
7			6.035	5.964			5.980	0.92	0.27
8	6.399	6.273			6.344	6.236	6.330	1.09	0.90

The bold values are used for error calculation. We use a of CL=100 and aspect ratio of 0.5
Mode eigenfunctions are shown in Figure 2.

Table 3. Resonant frequencies by BEM+FVM and GFEM without inertia (QS), elliptical crack

Mode	The resonant frequencies can be detected at detection points			BEM+FVM	Error (%)
	(-0.5, 0)	(0, 0.25)	(0, 0)		
1	1.527			1.518	0.59
2	3.027		3.090	3.050	0.75
3		3.290		3.241	1.51
5	4.890			4.816	1.54
7	6.890	6.853	6.944	6.771	1.76
8		7.308	7.235	7.107	1.80

The bold values are used for error calculation. We use a of CL=100 and aspect ratio of 0.5
Mode eigenfunctions are shown in Figure 3.

273 crack wave resonant frequencies, at least for a C_L of 100. A similar conclusion has also
 274 been reached by Shauer et al. (2021). Since we assume a quasi-static solid response, it
 275 is reasonable that our results have a better agreement to those by GFEM without in-
 276 ertia.

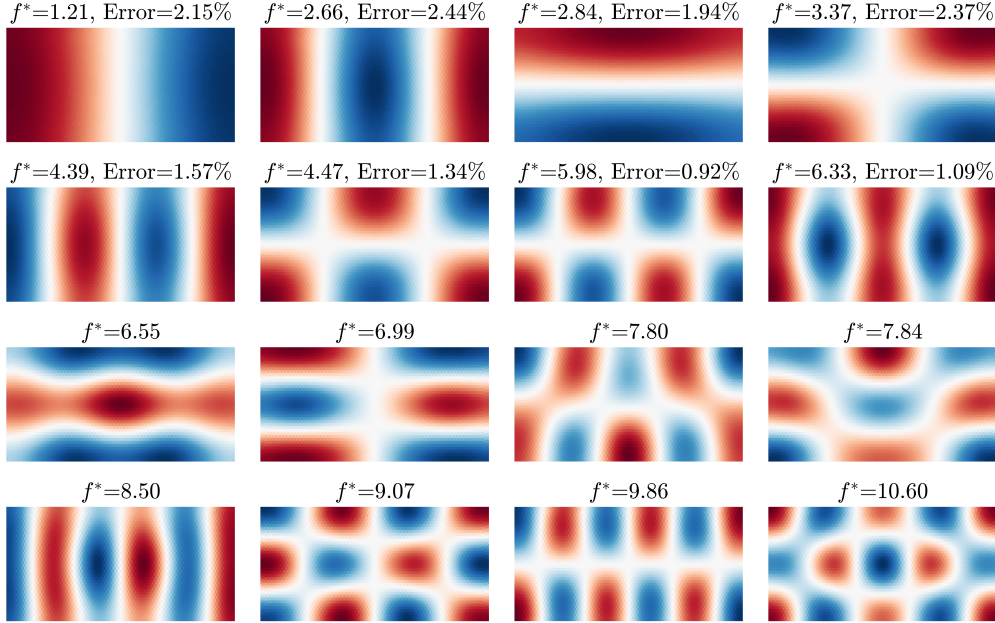


Figure 2. Dimensionless frequencies and eigenfunctions of the first 16 resonant modes (numbered in an ascending order in frequencies) of a rectangular crack with $C_L=100$ and aspect ratio of 0.5 calculated by BEM+FVM. The errors of selective resonant frequencies between the BEM+FVM and GFEM without inertia are shown in Table 2. The white color indicates the nodal lines.

277 The pressure eigenfunctions of the first 16 resonant modes are displayed in Figure
 278 2 for a rectangular crack and Figure 3 for an elliptical crack, showing a rich spectrum
 279 of spatial variations including longitudinal, transverse, and mixed modes. Different modes
 280 can produce different near and far field radiation patterns, that may be detectable in real
 281 seismic data (e.g., Liang et al., 2020).

282 The dimensionless frequencies of the first 9 longitudinal modes for rectangular cracks
 283 by various methods with different crack stiffness ratios are shown in Figure 4. The re-
 284 sults of Shauer et al. (2021) are only computed for a C_L of 100. For ease of comparison,
 285 we convert dimensionless frequencies f^* in our studies to those in B. Chouet (1986) f_C^* ,

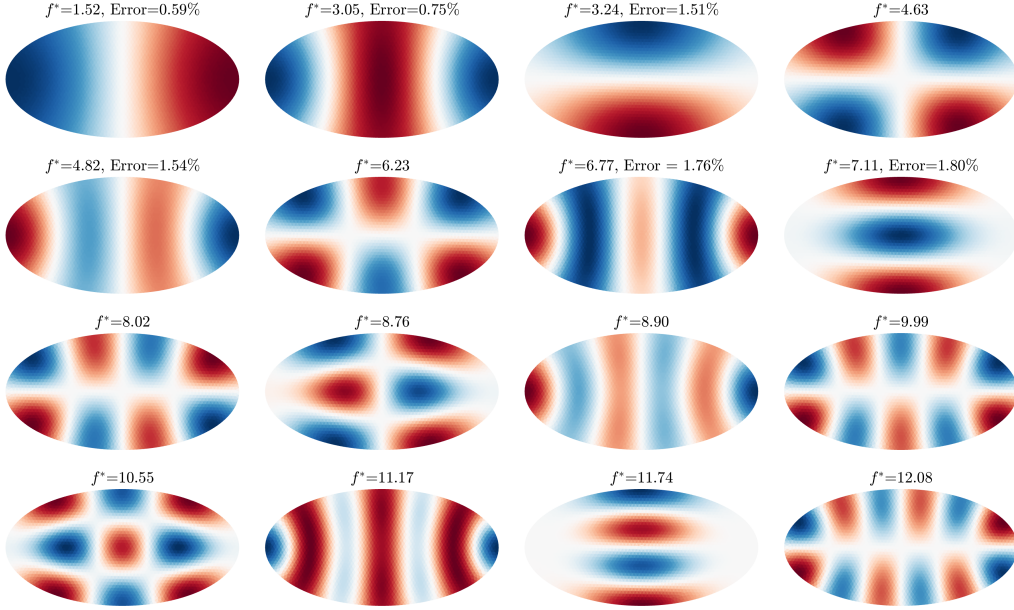


Figure 3. Same as Figure 2 but for an elliptical crack.

286 which are related by $f_C^* = f^* c_l / c_P$. Overall, our results match well with those by Shauer
 287 et al. (2021) (relative error < 3%) and also qualitatively well with those by B. Chouet
 288 (1986) and Maeda and Kumagai (2017). However, there are quantitative discrepancies
 289 between our results and those by B. Chouet (1986) (relative error 8.83-23.43%) and Maeda
 290 and Kumagai (2017) (relative error 2.72-16.63%, see the supporting information for tab-
 291 ulated errors). Particularly, both B. Chouet (1986) and Maeda and Kumagai (2017) sys-
 292 tematically give lower frequencies than those by our method and Shauer et al. (2021).
 293 We suspect these discrepancies are likely due to differences in spatial and temporal sam-
 294 pling, or domain sizes used in the FDM code in B. Chouet (1986) and Maeda and Ku-
 295 magai (2017). Particularly, a truncated domain in the FDM results in a more compli-
 296 ant solid response (Korneev et al., 2014), which in turn results in a lower crack wave speed
 297 and resonant frequencies. Our method uses boundary elements and thus an infinite do-
 298 main is directly satisfied. For this reason, when comparing results with Shauer et al. (2021),
 299 we deliberately used a very large domain (10 times the length of the crack) in the GFEM
 300 code to minimize its boundary effect using an unstructured grid, coarsening in regions
 301 far from the crack.

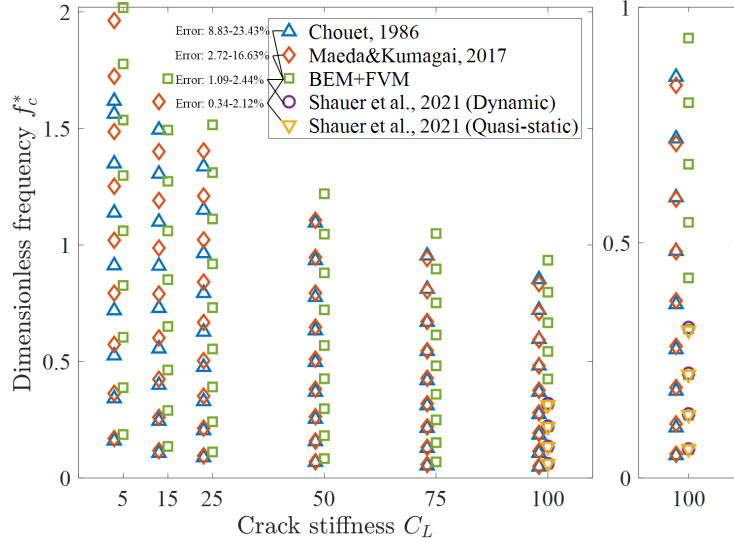


Figure 4. Dimensionless frequencies f_C^* of longitudinal modes for rectangular cracks with different C_L (5, 15, 25, 50, 75, 100) by various methods, and a zoom-in view of the case $C_L = 100$ on the right panel. Results by B. Chouet (1986) and Maeda and Kumagai (2017) are slightly shifted in the horizontal axis to avoid overcrowding the figure.

302

3.3 An example of intersecting cracks

303

304

305

306

307

308

309

310

311

312

313

314

315

316

We now apply our method to one example of intersecting cracks, one full ellipse with a half-elliptical branch, and obtain the first 16 eigenmodes, shown in Figure 5. Interactions between multiple cracks result in more complex resonant modes than in single cracks (shown in Figures 3 and 4). For example, the fundamental mode now involves fluid exchange between the major crack and the branch, and has a lower frequency than the fundamental mode of the major crack (the second mode in this case). When nodal lines coincide with the intersecting edge, resonances can be isolated on the major crack, such as modes 2, 7, 8, 13 and 16. Temporal manifestation of these modes requires a more peculiar condition: the excitation must not be located in the branch. One can certainly add more complexities in the crack network, such as asymmetries, non-planarity or more intricate coupling, and expect to encounter richer eigenmodes. However, such modeling only becomes meaningful when more compelling observations exist and require. We will demonstrate later how a particular crack shape can explain the ratio of the first two spectral peaks in the VLP seismic data at the Fani Maoré, Mayotte submarine volcano. Ex-

317 cept for that, we decide to leave the analysis of eigenmodes of a more complex crack net-
 318 work for future investigation.

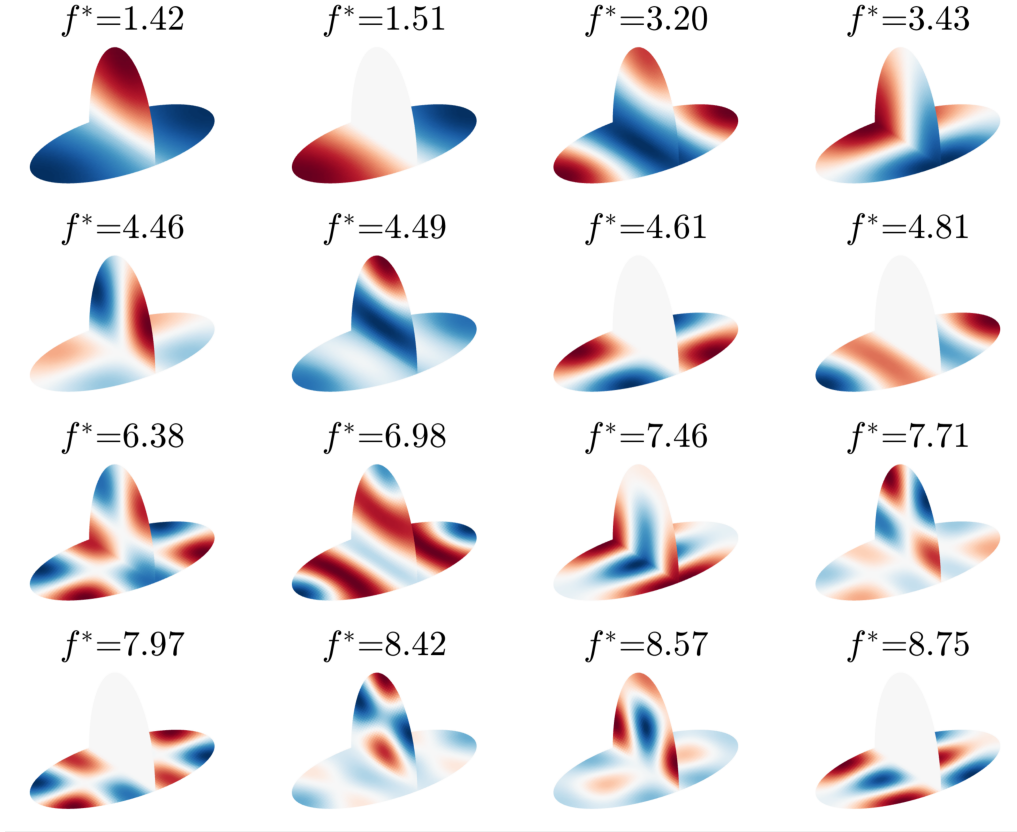


Figure 5. The first 16 eigenmodes of a simple two-intersecting-cracks geometry: a half ellipse intersecting a full ellipse (aspect ratio 0.5) along its minor axis. The major axis length of the full elliptical crack is chosen as L for the non-dimensionalisation.

319 **4 Effect of aspect ratio α and crack stiffness ratio C_L**

320 In this section, we present the effect of α and C_L on the resonant frequencies of rect-
 321 angular and elliptical cracks, with major and minor axes in the x - and y -directions,
 322 respectively. Maeda and Kumagai (2017) presented a similar analysis for rectangular cracks,
 323 but only on longitudinal and transverse modes. Here, we include the mixed modes and
 324 the results for elliptical cracks. We fixed $C_L = 100$ when varying α (from 0.05 to 1.00
 325 with an increment of 0.05) and fix $\alpha = 0.5$ when varying C_L (from 5 to 100 with an
 326 increment of 5). The frequencies of the first 16 eigenmodes are tabulated in the Support-

327 ing information. Here, we select 9 representative modes and visualize them in Figures
 328 6-9. For rectangular cracks, we associate to each mode a pair of numbers (i, j) that de-
 329 note the number of half wavelengths in the x - and y -directions. For instance, the fun-
 330 damental mode $(1, 0)$ is a longitudinal mode with one half wavelength pressure variation
 331 in the x -direction and quasi-uniform in the y -direction. Such numbering becomes less
 332 obvious for elliptical cracks, especially when the aspect ratio approaches 1, for which the
 333 eigenfunctions are better characterized by radial and circumferential variations. Nonethe-
 334 less, for the ease of comparing results with rectangular cracks, we still number the rep-
 335 resentative modes in Figures 7 and 9 approximately into longitudinal, transverse, and
 336 mixed modes.

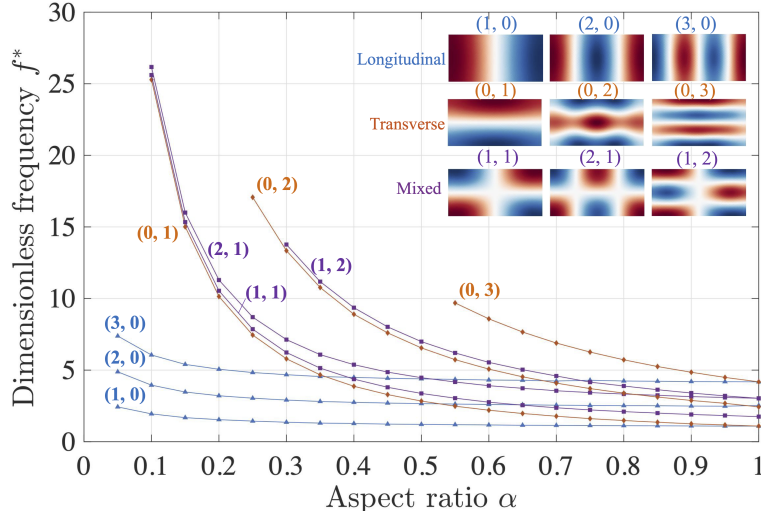


Figure 6. Dimensionless resonant frequencies of representative modes of rectangular cracks as a function of the aspect ratio α . C_L is fixed to 100. The eigenfunctions displayed are for an aspect ratio of 0.55. Certain high order mixed and transverse modes rank outside of the first 16 eigenmodes that we store, which causes the apparent absence of data at low aspect ratios.

337 4.1 Effect of aspect ratio

338 The variation of resonant frequencies with aspect ratio is shown in Figure 6 and
 339 7 for rectangular and elliptical cracks, respectively. For both cases, decreasing the as-
 340 pect ratio increases the crack stiffness from the transverse direction and results in higher
 341 resonant frequencies for all the modes. This effect is relatively mild for longitudinal modes
 342 but rather steep for transverse and mixed modes. For instance, when α of a rectangu-

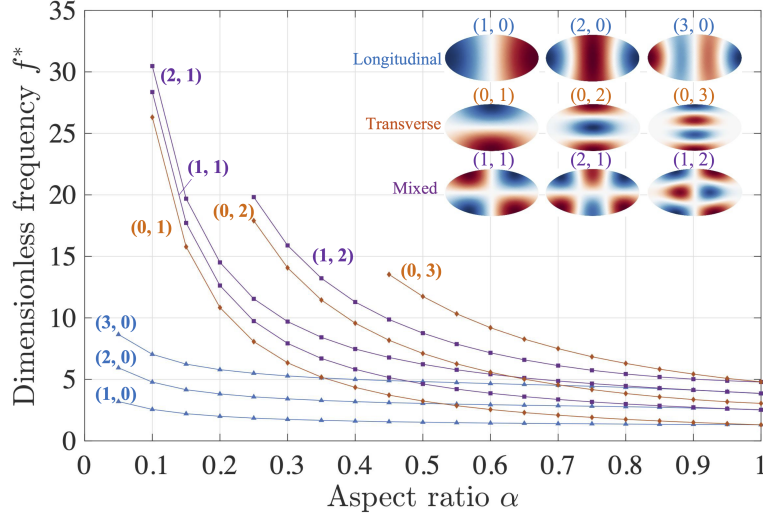


Figure 7. Same as Figure 6 but for elliptical cracks. Note that the mode numbers (i, j) are not strictly valid for an elliptical crack but are useful for our interpretation (more explanation in the main text).

lar crack decreases from 1.0 to 0.1, the frequency of the fundamental mode $(1, 0)$ increases by ~ 1.8 fold while the frequency of the mixed mode $(1, 1)$ increases by ~ 14.6 fold. As a result, the first few resonant modes are predominantly longitudinal for both rectangular and elliptical cracks at low aspect ratios (below 0.2). For a similar mode, the resonant frequency of an elliptical crack is consistently higher than that of the rectangular crack. This is expected as the elliptical crack is narrower in the transverse direction and thus stiffer than a rectangular crack of the same length and aspect ratio.

Another clear feature, for both rectangular and elliptical cracks, is that frequencies of modes with same wavelengths in the transverse direction converge as α decreases. For instance, frequencies of mixed modes $(1, 1)$ and $(2, 1)$ converge to the values of transverse mode $(0, 1)$. Similar convergence also exists for modes $(0, 2)$ and $(1, 2)$. This is expected because the crack wave speed, in the limit of low aspect ratio, is primarily controlled by the short wavelength in the transverse direction. As α increases, the frequencies of different modes become more intermingled and mode degeneration occurs, where modes with distinct eigenfunctions share the same frequency. It is well known that mode degeneration occurs at $\alpha = 1$ due to the geometric symmetry of a square or circle. What we show here is that mode degeneration also occurs at intermediate aspect ratios. For

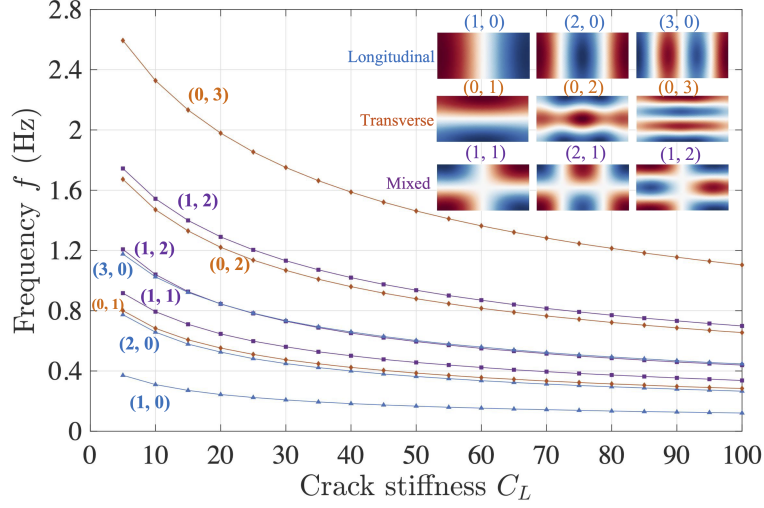


Figure 8. Resonant frequencies of representative modes of rectangular cracks as a function of the crack stiffness C_L . The aspect ratio α is set as 0.5

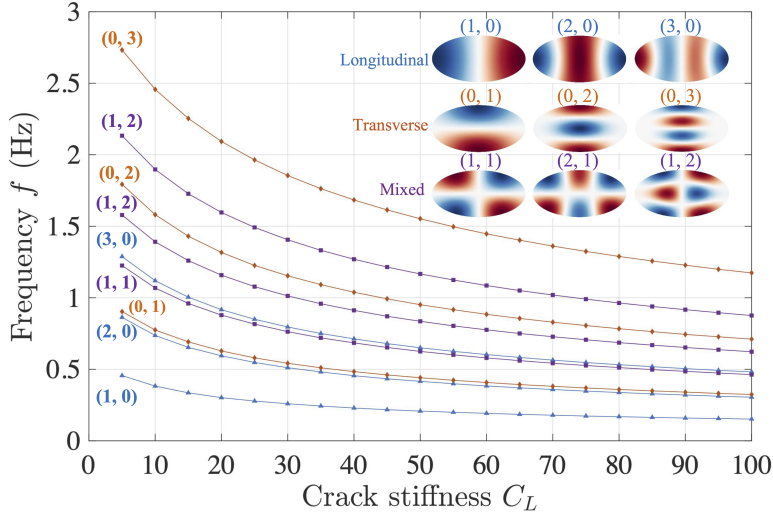


Figure 9. Same as Figure 8 but for elliptical cracks

360 instance, modes $(3, 0)$ and $(0, 1)$ for both a rectangular and elliptical crack share sim-
 361 ilar frequencies when $\alpha \approx 0.35$.

362 4.2 Effect of crack stiffness ratio

363 Since the normalization constant $(c_f/\sqrt{C_L})/L$ for frequency changes with C_L , we
 364 visualize the actual resonant frequency f , instead of f^* . We use $c_f = 1$ m/s and $L =$
 365 1 m to scale f^* to f . C_L is the key dimensionless parameter that controls the crack wave

366 propagation: the higher the value of C_L , the lower the phase velocity (e.g., B. Chouet,
 367 1986; Maeda & Kumagai, 2017). As a result, the resonant frequencies of all modes for
 368 both rectangular (Figure 8) and elliptical cracks (Figure 9) decrease continuously as C_L
 369 increases. Again, for a similar mode, the resonant frequencies of an elliptical crack is con-
 370 sistentally higher than those of a rectangular crack given the same axial lengths.

371 5 Energy dissipation

372 Since we currently focus on computing crack resonant frequencies in complex crack
 373 geometries, we assume both an inviscid fluid and a quasi-static solid and we do not con-
 374 sider energy dissipation, from either fluid viscosity or seismic radiation. When damp-
 375 ing exists, the resonant frequency becomes complex and the rate of decay is quantified
 376 by the quality factor

$$Q = \frac{\text{Re}(f)}{2\text{Im}(f)}, \quad (24)$$

377 which is also the number of cycles for an oscillation's energy to fall off to $e^{-2\pi} \sim 0.2\%$
 378 of its original value. The effect of viscous damping has been investigated analytically with
 379 fully dynamic (Korneev, 2008) and quasi-static solid response (Lipovsky & Dunham, 2015)
 380 on an infinite crack. However, the applicability of the Q formula on a finite crack has
 381 not yet been tested. In addition, the convoluted derivation in Korneev (2008) makes it
 382 difficult to quantify the relative contribution of different dissipative sources to the to-
 383 tal energy loss. On the other hand, numerical studies on rectangular cracks (e.g., Ku-
 384 magai & Chouet, 2000) have investigated the Q caused by seismic radiation but adopted
 385 a simplistic treatment of the fluid viscosity, either an inviscid or fully-developed flow. In
 386 this section, we offer a semi-analytical discussion of energy dissipation under a few as-
 387 sumptions and attempt to address two questions: (1) does the formula of Q developed
 388 by Lipovsky and Dunham (2015) for an infinite crack also apply to a finite crack? (2)
 389 which of the two sources of energy dissipation, fluid viscosity and seismic radiation, is
 390 more significant?

391 5.1 The applicability of Q formula from dispersion to a finite crack

392 We consider a viscous fluid with kinematic viscosity μ . To focus on the effect of
 393 the finite geometry, we compare analytical solutions by Lipovsky and Dunham (2015)
 394 to numerical solutions by Liang et al. (2020) for a rectangular crack, both of which as-

395 sume a quasi-static solid response. For simplicity, we focus on the boundary layer limit

$$\zeta = w_0/\sqrt{4\nu/\omega} \gg 1, \quad (25)$$

396 where the crack aperture w_0 is much larger than the thickness of the viscous boundary
 397 layer $\sqrt{4\nu/\omega}$. In this limit, Q is high and ω can be well approximated by the inviscid
 398 solution. The analytical formula of Q for crack waves with real wavenumber is given by
 399 equation (80) in Lipovsky and Dunham (2015) and, after neglecting the small imaginary
 400 part of phase velocity when $\zeta \gg 1$, we have:

$$Q = \sqrt{2}\zeta. \quad (26)$$

401 The hypothesis is that this expression for Q also holds, at least approximately for a fi-
 402 nite rectangular crack, regardless of its geometric shape, as long as w_0 , μ and ω are known.
 403 We perform numerical simulations using the program by Liang et al. (2020), who em-
 404 ployed a finite difference method on a stretched grid to deal with the narrow viscous bound-
 405 ary layer. We set $L = 100$ m, $K_f = 1$ Pa, $G = 1$ Pa, $w_0 = 1$ m, which results in a C_L
 406 of 100, and solve for the inviscid resonant angular frequencies ω of rectangular cracks
 407 of two aspect ratios, 0.5 and 1.0. We then adjust μ so that ζ takes the values of 10, 20,
 408 40, 60, 80, 100 and 200. We consider the first two modes of the crack with aspect ratio
 409 of 0.5 and the fundamental mode of the square crack to represent different mode types
 410 and crack shapes. The Q values of viscous cases are obtained using the methodology by
 411 Liang et al. (2020) and the comparison to equation (26) is shown in Figure 10.

412 As shown in Figure 10, the prediction by the analytical formula in Lipovsky and
 413 Dunham (2015) matches well the numerical solutions. The agreement gets better at large
 414 ζ , where the assumption of boundary layer limit becomes more accurate. The differences
 415 between the numerical and analytical solutions are less than 5% at $Q > 40$, while the
 416 difference at $Q = 10$ is $\sim 14\%$. Another encouraging finding is that aspect ratios and
 417 mode numbers of rectangular cracks have a negligible impact on the value of Q as long
 418 as ζ is the same. We thus postulate that the Q formula is likely to hold also for other
 419 crack shapes or even a crack network. We further propose that one may first approxi-
 420 mate the resonant frequency ω of complex shaped cracks using the inviscid solution ef-
 421 ficiently determined by our method, and then directly estimate Q using the analytical
 422 formula. However, future numerical studies considering both complex crack geometry
 423 and fluid viscosity are necessary to rigorously test this hypothesis.

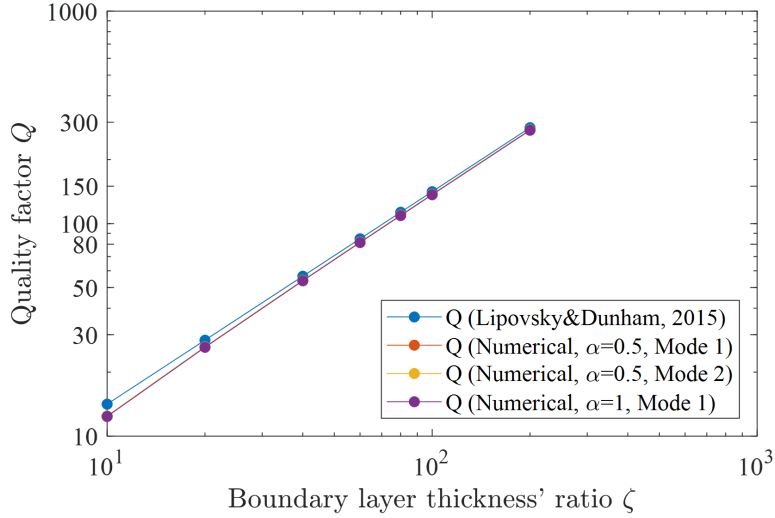


Figure 10. Quality factor of various resonant modes of rectangular cracks as a function of the boundary layer thickness ratio ζ .

424

5.2 The competition between radiation and viscous damping

425

426

427

428

429

430

431

432

433

434

435

436

Instead of considering the fully dynamic solid response (e.g., Korneev, 2008), we assume a quasi-dynamic solid response (e.g., Rice, 1993; Geubelle & Rice, 1995), which allows to explicit extract the instantaneous long wavelength emission perpendicular to the crack surface, the radiation damping (*RD*) term. We also consider an infinite crack in two dimensions for the ease of theoretical treatment following Lipovsky and Dunham (2015). By neglecting the wave mediated stresses and the seismic diffraction at the finite crack tips, the radiation we consider is an underestimate, but it is still useful for understanding the relative importance of various dissipation sources. Since resonances tend to be overdamped in the fully developed flow limit $\zeta \gg 40$ (Korneev, 2008; Lipovsky & Dunham, 2015), we continue to focus on the boundary layer limit $\zeta \ll 40$. We explicitly identify the radiation and viscous damping terms in the governing equation and then compute the ratio of their magnitudes.

437

438

439

The width-averaged crack wave equation considering viscous wall traction is obtained by combining the mass and momentum balance equations in Lipovsky and Dunham (2015),

$$\frac{\rho_f}{K_f} \frac{\partial^2 p}{\partial t^2} + \frac{\rho_f}{w_0} \frac{\partial^2 w}{\partial t^2} - \frac{\partial^2 p}{\partial x^2} - \frac{2}{w_0} \frac{\partial \tau}{\partial x} = 0, \quad (27)$$

440 where τ is the wall shear traction. We introduce the double Fourier transform of an ar-
 441 bitrary function $F(x, t)$ as

$$\hat{F}(k, \omega) = \int_{-\infty}^{+\infty} \int_{-\infty}^{+\infty} F(x, t) e^{-i(kx - \omega t)} dt dx. \quad (28)$$

442 Applying it to equation (27) leading to

$$-\omega^2 \rho_f \left(\frac{\hat{p}}{K_f} + \frac{\hat{w}}{w_0} \right) + k^2 \hat{p} - ik \frac{2}{w_0} \hat{\tau} = 0. \quad (29)$$

443 Using equation (38) in Lipovsky and Dunham (2015) and neglecting horizontal wall mo-
 444 tion, the wall shear traction is related to fluid pressure by

$$\hat{\tau} = -ikw_0\Omega\hat{p}/2, \quad (30)$$

445 where

$$\Omega = \left(\sqrt{i}/\zeta \right) \tanh \left(\zeta/\sqrt{i} \right), \quad (31)$$

446 and tends to \sqrt{i}/ζ in the boundary layer limit. Therefore, the viscous damping (*VD*)
 447 term in the equation is

$$VD = k^2\Omega\hat{p}. \quad (32)$$

448 Applying the quasi-dynamic solid response (Geubelle & Rice, 1995), the fluid pressure
 449 and crack opening are related by

$$\hat{p} = \frac{Gk\hat{w}}{2(1 - \nu_s)} - i\omega\eta_R\hat{w}, \quad (33)$$

450 where the two terms on the right hand side are the quasi-static response and radiation
 451 damping (*RD*), respectively, and $\eta_R = \rho_s c_p/2$ is the radiation damping coefficient. The
 452 ratio between the *QS* and *RD* terms is approximately $c_s^2/(c_p c)$ (dropping terms involv-
 453 ing Poisson's ratio), where $c = \omega/k$ is the crack wave phase velocity. In the low-frequency
 454 limit, which we are interested in, the crack wave speed is much smaller than the speeds
 455 of the solid body waves, $c \ll c_s \sim c_p$, and thus the *RD* term is much smaller than the
 456 *QS* term. Substituting equation (33) into (29) and approximating \hat{w}/\hat{p} using the *QS* part,
 457 we obtain the *RD* term in equation (29) as

$$RD = i\omega^3 \frac{\rho_f n_R}{K_f} \hat{w} \approx i\omega^3 \frac{\rho_f n_R}{K_f} \frac{2(1 - \nu_s)}{Gk} \hat{p}. \quad (34)$$

458 The ratio between *RD* and *VD* is

$$\frac{RD}{VD} = i c^3 \frac{\rho_f n_R}{K_f} \frac{2(1 - \nu_s)}{G\Omega} = i \frac{c_p c^3 (1 - \nu_s)}{c_f^2 c_s^2 \Omega}. \quad (35)$$

459 In the boundary layer limit, the magnitude of this ratio becomes

$$\left| \frac{RD}{VD} \right| = \frac{c_p c^3}{c_f^2 c_s^2} \zeta (1 - v_s). \quad (36)$$

460 When the overall damping is small, the crack wave phase velocity as a function of wave-
461 length λ is well approximated by the inviscid dispersion relation:

$$c = \sqrt{\frac{2\pi G w_0}{\lambda \rho_f (1 - v_s)}} \sim c_f / \text{sqrt} C_\lambda, \quad (37)$$

462 where $C_\lambda = K_f \lambda / G w_0$ is a crack stiffness ratio similar to C_L but replacing L by λ . Fi-
463 nally, we obtain RD/VD , which scales as

$$\left| \frac{RD}{VD} \right| \sim \frac{c_p c_f}{c_s^2} \frac{\zeta}{C_\lambda^{3/2}} = \frac{c_p c_s}{c_f^2} \zeta \left(\frac{w_0 \rho_s}{\lambda \rho_f} \right)^{3/2}, \quad (38)$$

464 after dropping small constants such as 2, π and μ_s . $|RD/VD|$ is governed by three di-
465 mensionless parameters: $\frac{c_p c_f}{c_s^2}$, C_λ and ζ . The first parameter one is controlled by the body
466 wave speeds of the solid and fluid and is not related to the crack geometry. For a typ-
467 ical crustal rock and liquid fluid, for instance with $c_f = 1500$ m/s, $c_p = 4500$ m/s, and
468 $c_s = 2500$ m/s, $\frac{c_p c_f}{c_s^2}$ is near unity. However, exsolved gases in liquid fluid, common in
469 shallow volcanic or geothermal environments (e.g., Kumagai & Chouet, 1999, 2001), can
470 significantly decrease the sound speed of the mixture, resulting in a much smaller $\frac{c_p c_f}{c_s^2}$.
471 The trade-off between C_λ and ζ in controlling $|RD/VD|$ is displayed in Figure 11. In
472 the regime of high ζ and low C_λ , seismic radiation dominates over viscous damping, while
473 in the regime of low ζ and high C_λ vice versa. Note that increasing λ or decreasing fre-
474 quency ω while fixing other parameters increases C_λ and simultaneously decreases ζ , both
475 of which lead to a lower percentage of damping in radiation.

476 **6 Application to VLP seismic signals during the Mayotte volcano-seismic** 477 **crisis**

478 Since 10 May 2018, an unprecedented submarine volcano-seismic crisis occurred
479 30 km east of Mayotte Island (France), featuring a lithosphere-scale dyke intrusion and
480 drainage ($\sim 5 \text{ km}^3$) of deep magma reservoirs and producing exceptionally deep seismic-
481 ity and substantial surface deformation (Cesca, Letort, et al., 2020; Feuillet et al., 2021;
482 Saurel et al., 2021; Mittal et al., 2022; Mercury et al., 2022; Retailleau et al., 2022). By
483 mid June of 2018, sustained long duration and highly oscillatory VLP seismic signals (see
484 an example in Figure 12a) have been observed and persist since, which are associated
485 with resonances of magma-filled cracks excited by nearby volcano-tectonic (VT) events

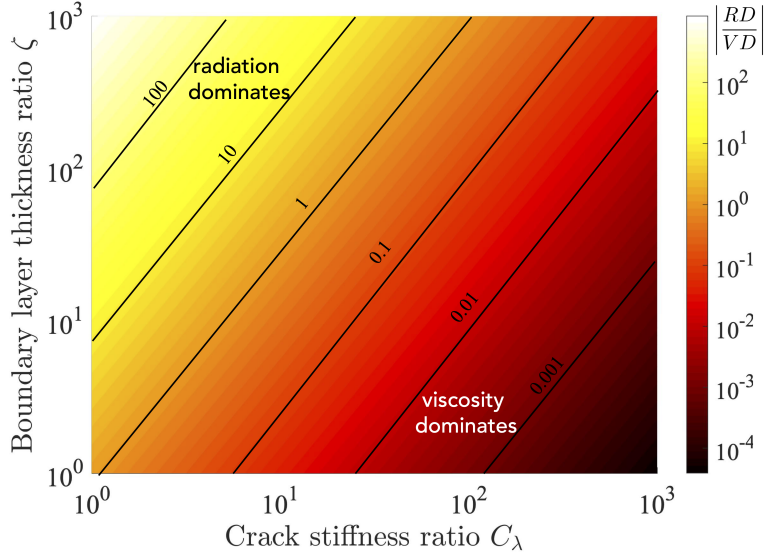


Figure 11. $|RD/VD|$ as a function of the crack stiffness ratio C_λ and the boundary layer thickness ratio ζ . Parameters used are $c_f = 1500$ m/s, $c_p = 4500$ m/s, and $c_s = 2500$ m/s.

486 or possible piston collapse movements (Cesca, Letort, et al., 2020; Feuillet et al., 2021).
 487 The stack of spectra of multiple VLP events reveals multiple resonant modes, among which
 488 the fundamental mode with period ~ 15.5 s is present in all events, but not all higher modes
 489 are manifested in each event, probably due to differences in the excitation. The funda-
 490 mental frequency can be readily explained by the crack model upon choosing a proper
 491 crack length and aperture (Cesca, Letort, et al., 2020). However, as shown in Figure 12b,
 492 the uneven spacing between resonant modes implies additional complexity in the source.
 493 Particularly, the ratio between the first higher mode and the fundamental mode is $f_2/f_1 \approx$
 494 2.5. As shown in Figures 6 and 7, this value can not be explained by a simple rectan-
 495 gular or elliptical crack. Here, we show this observation can be explained by a dumbbell-
 496 shaped crack (Figure 12c). This crack shape is compatible with the f_2/f_1 data, but might
 497 still differ from the real crack geometry in Mayotte as we have not made a systematic
 498 attempt to also match the frequencies of other higher modes. However, this example is
 499 sufficient to demonstrate the potential application of the developed method. One pro-
 500 found question is perhaps whether one can reconstruct the topology of the crack given
 501 the information of all the resonant frequencies. Mark Kac also asked a similar question
 502 “Can one hear the shape of a drum?” (Kac, 1966). Unfortunately, the answer is nega-
 503 tive: there exist multiple isospectral geometries that share the same resonant frequen-

504 cies, as mathematically proven by Gordon et al. (1992). However, these isospectral ge-
 505 ometries are rare even though they do exist and one can still decipher the shape of the
 506 resonator given additional constraints of the vibration pattern, which in practice requires
 507 dense geophysical observation particularly in the near field. A formal inversion proce-
 508 dure would need to be developed in the future to find the optimal crack geometry or topol-
 509 ogy of interconnected crack networks that best explains all the observed resonant fre-
 quencies and other geophysical constraints.

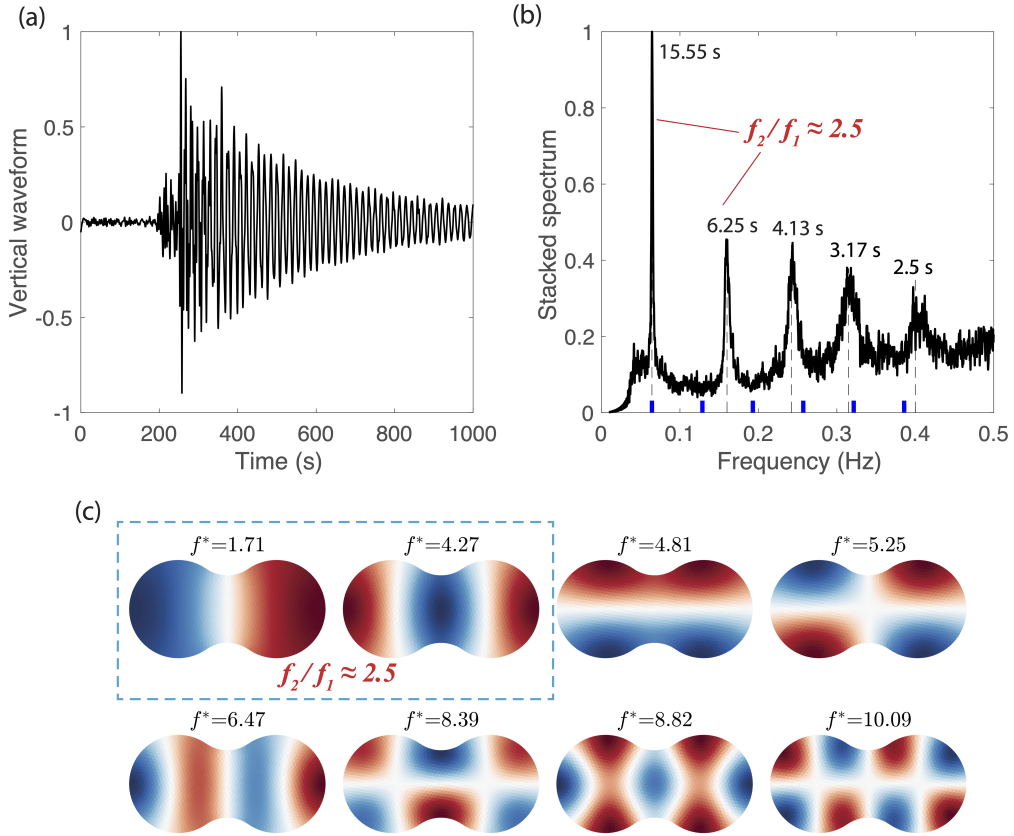


Figure 12. (a) Normalized vertical acceleration waveform of an representative VLP event (on 11 November 2018, bandpass filtered to 0.02-0.1 Hz) at the nearest broadband seismic station YTMZ on land, during the volcano-seismic crisis near Mayotte. (b) Stacked spectrum of 21 strong VLP signals compiled by Cesca, Letort, et al. (2020), highlighting multiple unevenly spaced resonant modes (dashed lines). Particularly, the frequency ratio between the first two modes $f_2/f_1 \approx 2.5$. The blue ticks indicate the integer multiples of the fundamental frequency. (c) Eigenmodes of a possible crack shape that satisfies $f_2/f_1 \approx 2.5$.

511 7 Summary

512 We have developed a hybrid method that couples the boundary element and finite
 513 volume method to efficiently compute the resonant modes of fluid-filled cracks with com-
 514 plex geometry. Particularly, the BEM reduces three dimensional cracks to 2D surfaces,
 515 substantially decreasing the number of degrees of freedom. By performing eigenmode
 516 analysis in the frequency domain, we avoid errors from both the time discretization and
 517 spectral analysis of the time domain data. We solve the problem in dimensionless form
 518 so that the results can be conveniently scaled to other crack sizes. After proper verifi-
 519 cation, we apply our method to an example of a crack network, revealing distinct res-
 520 onant frequencies and vibration patterns, which may be utilized to infer more accurately
 521 crack shapes from seismic data.

522 We then systematically analyze the influence of crack aspect ratio and crack stiff-
 523 ness on the resonant frequencies for both rectangular and elliptical cracks, which are com-
 524 mon models for interpreting real data. In general, rectangular and elliptical cracks share
 525 similar eigenmode types and frequencies, while the elliptical crack has slightly higher re-
 526 sonance frequencies due to the reduced length of the minor axis. At a high aspect ratio,
 527 the frequencies of various mode types (longitudinal, transverse and mixed) are intermin-
 528 gled and mode degeneration occurs. Reducing the aspect ratio increases the frequencies
 529 of all the modes, but more intensely for transverse and mixed modes than for longitu-
 530 dinal modes. In addition, at low aspect ratio, frequencies of modes (transverse or mixed)
 531 with the same wavelengths in the transverse direction converge and differentiating them
 532 requires additional knowledge of their vibration patterns. On the other hand, increas-
 533 ing C_L results in a decrease in resonant frequencies for all modes, regardless of the crack
 534 geometry, which is primarily due to the decrease in crack wave propagation speed.

535 The major part of this work does not consider fluid viscosity or seismic radiation,
 536 and thus cannot be used to directly compute the quality factor Q . However, by making
 537 a few assumptions, we offer additional theoretical discussion on the energy dissipation.
 538 First, by comparing numerical to analytical solutions, we confirm that the simple for-
 539 mula $Q = \sqrt{2}\zeta$ derived by Lipovsky and Dunham (2015) is a rather good approxima-
 540 tion for a rectangular crack when the thickness of the viscous boundary layer is much
 541 smaller than the crack width, regardless of crack aspect ratio or vibrational mode. This
 542 is an encouraging finding that suggests one may first obtain the inviscid resonant fre-

543 frequencies using our method and then apply analytical formula to compute Q . Note that
 544 this formula still does not consider seismic radiation. We then derived the relative ra-
 545 tio of the radiation damping to viscous damping, assuming a quasi-dynamic solid response
 546 on an infinite crack. We show that this ratio is primarily controlled by three dimension-
 547 less parameters: $c_p c_f / c_s^2$, C_λ and ζ . Particularly, in the limit of high ζ and low C_λ , seis-
 548 mic radiation dominates over viscous damping while the opposite is true in the limit of
 549 low ζ and high C_λ . Note that the seismic radiation considered here is a lower bound as
 550 we neglected the wave-mediated stresses and the seismic radiation at the finite crack tip.
 551 However, our theoretical development still offers a valuable insight into the partition of
 552 damping in crack waves.

553 Finally, we obtain one possible crack shape, a “dumbbell”, that successfully explains
 554 the ratio of frequencies of the first two modes in the VLP seismic data during the 2018
 555 Fani Maoré, Mayotte submarine volcanic eruption. This shape is one possibility and may
 556 be updated when additional higher modes and geophysical constraints are integrated into
 557 the analysis. In addition, the method developed here can be directly applied to other
 558 scenarios, such as unconventional oil and gas fields and glacier hydraulics. Future work
 559 requires a rigorous treatment of fluid viscosity, elastodynamics, and coupling to other
 560 geometries such as conduits and equidimensional chambers.

561 **8 Acknowledgments**

562 This work is funded by the early career research grant by the National Science Fun-
 563 dation of China (NSFC) with grant No. 42204059 and the Fundamental Research Funds
 564 for the Central Universities disseminated by IDMR at Sichuan University. It was also
 565 supported by the French government, through the UCAJEDI Investments in the Future
 566 project (ANR-15-IDEX-01) managed by the National Research Agency (ANR).

567 **9 Data Availability Statement**

568 The source code and the input files associated with the simulation cases are included
 569 in the Zenodo data repository at Liang et al. (2023). The VLP catalog of the Mayotte
 570 crisis is provided by Cesca, Heimann, et al. (2020) and is freely available online.

References

- 571
- 572 Aki, K., Fehler, M., & Das, S. (1977). Source mechanism of volcanic tremor: Fluid-
 573 driven crack models and their application to the 1963 Kilauea eruption. *Journal of Volcanology and Geothermal Research*, *2*(3), 259–287. doi: 10.1016/0377-
 574 0273(77)90003-8
- 575
- 576 Aster, R. C. (2019). Interrogating a surging glacier with seismic interferometry. *Geophysical Research Letters*, *46*(14), 8162–8165. doi: 10.1029/2019GL084286
- 577
- 578 Berre, I., Doster, F., & Keilegavlen, E. (2019). Flow in fractured porous media:
 579 A review of conceptual models and discretization approaches. *Transport in Porous Media*, *130*(1), 215–236. doi: 10.1007/s11242-018-1171-6
- 580
- 581 Cao, H., Medici, E., & Askari, R. (2021). Physical modeling of fluid-filled fractures
 582 using the dynamic photoelasticity technique. *Geophysics*, *86*(1), T33–T43. doi:
 583 10.1190/geo2020-0037.1
- 584
- 585 Cesca, S., Heimann, S., Letort, J., Razafindrakoto, H., Dahm, T., & Cotton, F.
 586 (2020). *Seismic catalogues of the 2018–2019 volcano-seismic crisis offshore mayotte, comoro islands. v. 1.0 (october 2019). available at gfz data services*. Retrieved from <https://doi.org/10.5880/GFZ.2.1.2019.004> doi:
 587 10.5880/GFZ.2.1.2019.004
- 588
- 589 Cesca, S., Letort, J., Razafindrakoto, H. N., Heimann, S., Rivalta, E., Isken, M. P.,
 590 ... others (2020). Drainage of a deep magma reservoir near mayotte inferred
 591 from seismicity and deformation. *Nature Geoscience*, *13*(1), 87–93. doi:
 592 10.1038/s41561-019-0505-5
- 593
- 594 Chouet, B. (1986). Dynamics of a fluid-driven crack in three dimensions by the finite
 595 difference method. *Journal of Geophysical Research: Solid Earth*, *91*(B14),
 13967–13992. doi: 10.1029/JB091iB14p13967
- 596
- 597 Chouet, B. A., Page, R. A., Stephens, C. D., Lahr, J. C., & Power, J. A. (1994).
 598 Precursory swarms of long-period events at redoubt volcano (1989–1990),
 599 alaska: their origin and use as a forecasting tool. *Journal of Volcanology and
 Geothermal Research*, *62*(1-4), 95–135. doi: 10.1016/0377-0273(94)90030-2
- 600
- 601 Cruz, F. G., & Chouet, B. A. (1997). Long-period events, the most characteristic
 602 seismicity accompanying the emplacement and extrusion of a lava dome in
 603 galeras volcano, colombia, in 1991. *Journal of Volcanology and Geothermal
 Research*, *77*(1-4), 121–158. doi: 10.1016/S0377-0273(96)00091-1

- 604 Durran, D. R. (2013). *Numerical methods for wave equations in geophysical fluid dy-*
 605 *namics* (Vol. 32). Springer Science & Business Media.
- 606 Fehler, M., & Aki, K. (1978). Numerical study of diffraction of plane elas-
 607 tic waves by a finite crack with application to location of a magma lens.
 608 *Bulletin of the Seismological Society of America*, *68*(3), 573–598. doi:
 609 10.1785/BSSA0680030573
- 610 Ferrazzini, V., & Aki, K. (1987). Slow waves trapped in a fluid-filled infinite crack:
 611 Implication for volcanic tremor. *Journal of Geophysical Research: Solid Earth*,
 612 *92*(B9), 9215–9223. doi: 10.1029/JB092iB09p09215
- 613 Feuillet, N., Jorry, S., Crawford, W. C., Deplus, C., Thinon, I., Jacques, E.,
 614 ... others (2021). Birth of a large volcanic edifice offshore mayotte via
 615 lithosphere-scale dyke intrusion. *Nature Geoscience*, *14*(10), 787–795. doi:
 616 10.1038/s41561-021-00809-x
- 617 Frehner, M. (2013). Krauklis wave initiation in fluid-filled fractures by a passing
 618 body wave. In *Poromechanics v: Proceedings of the fifth biot conference on*
 619 *poromechanics* (pp. 92–100). doi: 10.1061/9780784412992.011
- 620 Frehner, M., & Schmalholz, S. M. (2010). Finite-element simulations of stoneley
 621 guided-wave reflection and scattering at the tips of fluid-filled fractures. *Geo-*
 622 *physics*, *75*(2), T23–T36. doi: 10.1190/1.3340361
- 623 Fujita, E., & Ida, Y. (2003). Geometrical effects and low-attenuation reso-
 624 nance of volcanic fluid inclusions for the source mechanism of long-period
 625 earthquakes. *Journal of Geophysical Research: Solid Earth*, *108*(B2). doi:
 626 10.1029/2002JB001806
- 627 Geubelle, P. H., & Rice, J. R. (1995). A spectral method for three-dimensional elas-
 628 todynamic fracture problems. *Journal of the Mechanics and Physics of Solids*,
 629 *43*(11), 1791–1824. doi: 10.1016/0022-5096(95)00043-I
- 630 Gordon, C., Webb, D. L., & Wolpert, S. (1992). One cannot hear the shape of a
 631 drum. *Bulletin of the American Mathematical Society*, *27*(1), 134–138. doi: 10
 632 .1090/S0273-0979-1992-00289-6
- 633 Gräff, D., Walter, F., & Lipovsky, B. P. (2019). Crack wave resonances within the
 634 basal water layer. *Annals of Glaciology*, *60*(79), 158–166. doi: 10.1017/aog
 635 .2019.8
- 636 Henry, F., Fokkema, J., & De Pater, C. (2002). Experiments on stoneley wave prop-

- 637 agation in a borehole intersected by a finite horizontal fracture. In *64th eage*
638 *conference & exhibition* (pp. cp-5). doi: 10.3997/2214-4609-pdb.5.P143
- 639 Jin, Y., Zheng, Y., Huang, L., & Ehlig-Economides, C. (2022). Characterizing
640 hydraulic fractures using the transient pressure surge effect. In *Spe/aapg/seg*
641 *unconventional resources technology conference* (p. D021S028R002). doi:
642 10.15530/urtec-2022-3718981
- 643 Kac, M. (1966). Can one hear the shape of a drum? *The american mathematical*
644 *monthly*, *73*(4P2), 1–23. doi: 10.1080/00029890.1966.11970915
- 645 Karimi-Fard, M., Durlofsky, L. J., & Aziz, K. (2004). An efficient discrete-fracture
646 model applicable for general-purpose reservoir simulators. *SPE journal*, *9*(02),
647 227–236. doi: 10.2118/88812-PA
- 648 Kawakatsu, H., Kaneshima, S., Matsubayashi, H., Ohminato, T., Sudo, Y., Tsutsui,
649 T., . . . Legrand, D. (2000). Aso94: Aso seismic observation with broadband
650 instruments. *Journal of Volcanology and Geothermal Research*, *101*(1-2),
651 129–154. doi: 10.1016/S0377-0273(00)00166-9
- 652 Korneev, V. (2008). Slow waves in fractures filled with viscous fluid. *Geophysics*,
653 *73*(1), N1–N7. doi: 10.1190/1.2802174
- 654 Korneev, V., Danilovskaya, L., Nakagawa, S., & Moridis, G. (2014). Krauklis wave
655 in a trilayer. *Geophysics*, *79*(4), L33–L39. doi: 10.1190/geo2013-0216.1
- 656 Krauklis, P. V. (1962). On some low-frequency oscillations of a fluid layer in an elas-
657 tic medium. *Prikl. Mat. Mekh.*, *26*(6), 1111–1115. doi: 10.1016/0021-8928(63)
658 90084-4
- 659 Kumagai, H., & Chouet, B. A. (1999). The complex frequencies of long-period seis-
660 mic events as probes of fluid composition beneath volcanoes. *Geophysical Jour-*
661 *nal International*, *138*(2), F7–F12. doi: 10.1046/j.1365-246X.1999.00911.x
- 662 Kumagai, H., & Chouet, B. A. (2000). Acoustic properties of a crack containing
663 magmatic or hydrothermal fluids. *Journal of Geophysical Research: Solid*
664 *Earth*, *105*(B11), 25493–25512. doi: 10.1029/2000JB900273
- 665 Kumagai, H., & Chouet, B. A. (2001). The dependence of acoustic properties of
666 a crack on the resonance mode and geometry. *Geophysical research letters*,
667 *28*(17), 3325–3328. doi: 10.1029/2001GL013025
- 668 Kumagai, H., Miyakawa, K., Negishi, H., Inoue, H., Obara, K., & Suetsugu, D.
669 (2003). Magmatic dike resonances inferred from very-long-period seismic

- 670 signals. *Science*, *299*(5615), 2058–2061. Retrieved from <http://science>
671 [.sciencemag.org/content/299/5615/2058](http://science.sciencemag.org/content/299/5615/2058) doi: 10.1126/science.1081195
- 672 Li, L., & Lee, S. H. (2008). Efficient field-scale simulation of black oil in a nat-
673 urally fractured reservoir through discrete fracture networks and homoge-
674 nized media. *SPE Reservoir evaluation & engineering*, *11*(04), 750–758. doi:
675 10.2118/103901-PA
- 676 Liang, C., Karlstrom, L., & Dunham, E. M. (2020). Magma oscillations in a
677 conduit-reservoir system, application to very long period (vlp) seismicity at
678 basaltic volcanoes: 1. theory. *Journal of Geophysical Research: Solid Earth*,
679 *125*(1), e2019JB017437. doi: 10.1029/2019JB017437
- 680 Liang, C., O’Reilly, O., Dunham, E. M., & Moos, D. (2017). Hydraulic fracture di-
681 agnostics from krauklis-wave resonance and tube-wave reflections. *Geophysics*,
682 *82*(3), D171–D186. doi: 10.1190/geo2016-0480.1
- 683 Liang, C., Peng, J., Ampuero, J.-P., Shauer, N., & Dai, K. (2023, August). *Dataset*
684 *for "Resonances in fluid-filled cracks of complex geometry and application*
685 *to very long period (VLP) seismic signals at Mayotte submarine volcano"*.
686 Zenodo. Retrieved from <https://doi.org/10.5281/zenodo.8275079> doi:
687 10.5281/zenodo.8275079
- 688 Lipovsky, B. P., & Dunham, E. M. (2015). Vibrational modes of hydraulic frac-
689 tures: Inference of fracture geometry from resonant frequencies and attenua-
690 tion. *Journal of Geophysical Research: Solid Earth*, *120*(2), 1080–1107. doi:
691 10.1002/2014JB011286
- 692 Lokmer, I., Saccorotti, G., Di Lieto, B., & Bean, C. J. (2008). Temporal evolution
693 of long-period seismicity at etna volcano, italy, and its relationships with the
694 2004–2005 eruption. *Earth and Planetary Science Letters*, *266*(1-2), 205–220.
695 doi: 10.1016/j.epsl.2007.11.017
- 696 Maeda, Y., & Kumagai, H. (2013). An analytical formula for the longitudinal res-
697 onance frequencies of a fluid-filled crack. *Geophysical Research Letters*, *40*(19),
698 5108–5112. doi: 10.1002/grl.51002
- 699 Maeda, Y., & Kumagai, H. (2017). A generalized equation for the resonance fre-
700 quencies of a fluid-filled crack. *Geophysical Journal International*, *209*(1), 192–
701 201. doi: 10.1093/gji/ggx019
- 702 McQuillan, M., & Karlstrom, L. (2021). Fluid resonance in elastic-walled englacial

- 703 transport networks. *Journal of Glaciology*, 67(266), 999–1012. doi: 10.1017/jog
704 .2021.48
- 705 Mercury, N., Lemoine, A., Doubre, C., Bertil, D., van Der Woerd, J., Hoste-
706 Colomer, R., & Battaglia, J. (2022). Onset of a submarine eruption east of
707 mayotte, comoros archipelago: the first ten months seismicity of the seismo-
708 volcanic sequence (2018–2019). *Comptes Rendus. Géoscience*, 354(S2), 105–
709 136. doi: 10.5802/crgeos.191
- 710 Métaxian, J.-P., Araujo, S., Mora, M., & Lesage, P. (2003). Seismicity related to the
711 glacier of cotopaxi volcano, ecuador. *Geophysical Research Letters*, 30(9). doi:
712 10.1029/2002GL016773
- 713 Mittal, T., Jordan, J. S., Retailleau, L., Beauducel, F., & Peltier, A. (2022). May-
714 otte 2018 eruption likely sourced from a magmatic mush. *Earth and Planetary
715 Science Letters*, 590, 117566. doi: 10.1016/j.epsl.2022.117566
- 716 Moifar, A., Varavei, A., Sepehrnoori, K., & Johns, R. T. (2013, 07). Develop-
717 ment of an Efficient Embedded Discrete Fracture Model for 3D Compositional
718 Reservoir Simulation in Fractured Reservoirs. *SPE Journal*, 19(02), 289-303.
719 doi: 10.2118/154246-PA
- 720 Nakagawa, S., Nakashima, S., & Korneev, V. A. (2016). Laboratory measurements
721 of guided-wave propagation within a fluid-saturated fracture. *Geophysical
722 Prospecting*, 64(1), 143–156. doi: 10.1111/1365-2478.12223
- 723 Nakano, M., & Kumagai, H. (2005). Response of a hydrothermal system to
724 magmatic heat inferred from temporal variations in the complex frequen-
725 cies of long-period events at kusatsu-shirane volcano, japan. *Journal of
726 volcanology and geothermal research*, 147(3-4), 233–244. doi: 10.1016/
727 j.jvolgeores.2005.04.003
- 728 Nikkhoo, M., & Walter, T. R. (2015). Triangular dislocation: an analytical, artefact-
729 free solution. *Geophysical Journal International*, 201(2), 1119–1141. doi: 10
730 .1093/gji/ggv035
- 731 Niu, J., & Song, T.-R. A. (2020). Real-time and in-situ assessment of conduit
732 permeability through diverse long-period tremors beneath aso volcano,
733 japan. *Journal of Volcanology and Geothermal Research*, 401, 106964. doi:
734 10.1016/j.jvolgeores.2020.106964
- 735 Okada, Y. (1985). Surface deformation due to shear and tensile faults in a half-

- 736 space. *Bulletin of the seismological society of America*, 75(4), 1135–1154.
- 737 Okada, Y. (1992). Internal deformation due to shear and tensile faults in a half-
738 space. *Bulletin of the Seismological Society of America*, 82(2), 1018–1040.
- 739 O’Reilly, O., Dunham, E. M., & Nordström, J. (2017). Simulation of wave propa-
740 gation along fluid-filled cracks using high-order summation-by-parts operators
741 and implicit-explicit time stepping. *SIAM Journal on Scientific Computing*,
742 39(4), B675–B702. Retrieved from <https://doi.org/10.1137/16M1097511>
743 doi: 10.1137/16M1097511
- 744 Paillet, F. L., & White, J. E. (1982, 08). Acoustic modes of propagation in
745 the borehole and their relationship to rock properties. *Geophysics*, 47(8),
746 1215–1228. Retrieved from <https://doi.org/10.1190/1.1441384> doi:
747 10.1190/1.1441384
- 748 Pointer, T., Liu, E., & Hudson, J. A. (1998). Numerical modelling of seismic
749 waves scattered by hydrofractures: application of the indirect boundary el-
750 ement method. *Geophysical Journal International*, 135(1), 289–303. doi:
751 10.1046/j.1365-246X.1998.00644.x
- 752 Retailleau, L., Saurel, J.-M., Laporte, M., Lavayssière, A., Ferrazzini, V., Zhu,
753 W., ... others (2022). Automatic detection for a comprehensive view of
754 mayotte seismicity. *Comptes Rendus. Géoscience*, 354(S2), 153–170. doi:
755 10.5802/crgeos.133
- 756 Rice, J. R. (1993). Spatio-temporal complexity of slip on a fault. *Journal of Geo-
757 physical Research: Solid Earth*, 98(B6), 9885–9907. doi: 10.1029/93JB00191
- 758 Rona, A. (2007). The acoustic resonance of rectangular and cylindrical cavities.
759 *Journal of Algorithms & Computational Technology*, 1(3), 329–356. doi:
760 10.1260/174830107782424110
- 761 Saurel, J.-M., Jacques, E., Aiken, C., Lemoine, A., Retailleau, L., Lavayssière, A.,
762 ... others (2021). Mayotte seismic crisis: building knowledge in near real-time
763 by combining land and ocean-bottom seismometers, first results. *Geophysical
764 Journal International*, 228(2), 1281–1293. doi: 10.1093/gji/ggab392
- 765 Segall, P. (2010). *Earthquake and volcano deformation*. Princeton University Press.
766 doi: 10.1515/9781400833856
- 767 Shauer, N., Desmond, K. W., Gordon, P. A., Liu, F., & Duarte, C. A. (2021). A
768 three-dimensional generalized finite element method for the simulation of wave

- 769 propagation in fluid-filled fractures. *Computer Methods in Applied Mechanics*
 770 *and Engineering*, 386, 114136. doi: 10.1016/j.cma.2021.114136
- 771 Stuart, G., Murray, T., Brisbourne, A., Styles, P., & Toon, S. (2005). Seismic emis-
 772 sions from a surging glacier: Bakaninbreen, svalbard. *Annals of Glaciology*, 42,
 773 151–157. doi: 10.3189/172756405781812538
- 774 Sun, F., Gong, Y., & Dong, C. (2020). A novel fast direct solver for 3d elas-
 775 tic inclusion problems with the isogeometric boundary element method.
 776 *Journal of Computational and Applied Mathematics*, 377, 112904. doi:
 777 10.1016/j.cam.2020.112904
- 778 Tang, X., & Cheng, C. (1988). Wave propagation in a fluid-filled fracture—an exper-
 779 imental study. *Geophysical Research Letters*, 15(13), 1463–1466. doi: 10.1029/
 780 GL015i013p01463
- 781 Tang, X., & Cheng, C. (1989). A dynamic model for fluid flow in open borehole frac-
 782 tures. *Journal of Geophysical Research: Solid Earth*, 94(B6), 7567–7576. doi:
 783 10.1029/JB094iB06p07567
- 784 Tary, J.-B., Van der Baan, M., & Eaton, D. W. (2014). Interpretation of
 785 resonance frequencies recorded during hydraulic fracturing treatments.
 786 *Journal of Geophysical Research: Solid Earth*, 119(2), 1295–1315. doi:
 787 10.1002/2013JB010904
- 788 Xu, Y., Cavalcante Filho, J., Yu, W., & Sepehrnoori, K. (2017). Discrete-
 789 fracture modeling of complex hydraulic-fracture geometries in reservoir sim-
 790 ulators. *SPE Reservoir Evaluation & Engineering*, 20(02), 403–422. doi:
 791 10.2118/183647-PA
- 792 Yamamoto, M., & Kawakatsu, H. (2008). An efficient method to compute the
 793 dynamic response of a fluid-filled crack. *Geophysical Journal International*,
 794 174(3), 1174–1186. doi: 10.1111/j.1365-246X.2008.03871.x
- 795 Zheng, Y., Malallah, A. H., Fehler, M. C., & Hu, H. (2016). 2d full-waveform model-
 796 ing of seismic waves in layered karstic media. *Geophysics*, 81(2), T25–T34. doi:
 797 10.1190/geo2015-0307.1

798 **Appendix A Matrices **D** and **T** for a simple crack intersection**

799 In this section, we show step by step how to construct matrices **D** and **T** for a sim-
 800 ple crack intersection shown in Figure A1. The element number and positive flux direc-

801 tion of each active connection as labeled. The boundary edges have zero flux and they
 802 do not contribute to \mathbf{D} and \mathbf{T} . Thus, we have five elements and five active connections
 803 numbered as $\{2 \rightarrow 1, 3 \rightarrow 2, 4 \rightarrow 2, 5 \rightarrow 2, 5 \rightarrow 4\}$, where $i \rightarrow j$ defines the positive flux
 direction. The size of both \mathbf{D} and \mathbf{T} are 5 by 5.

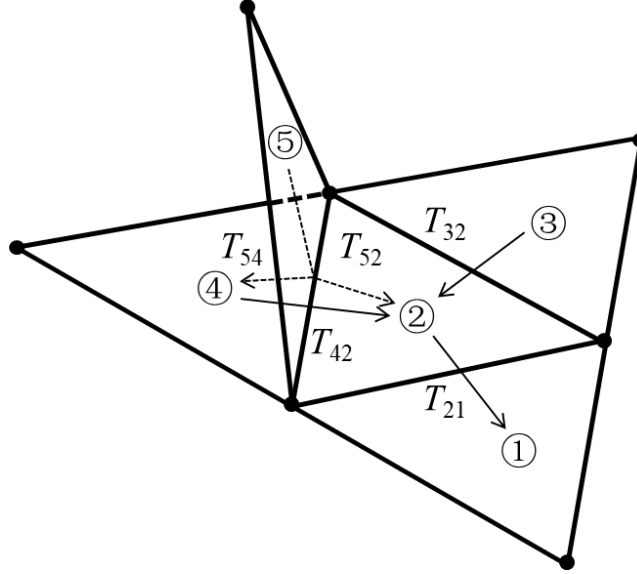


Figure A1. Geometry of a simple crack intersection. The element number and the positive flow direction of each active connection (non-zero flux) are indicated by the circled number and arrow, respectively. The scalar transmissibilities are labeled near each connection.

804

805 Let's first consider the matrix \mathbf{D} , which sums the flux from active connections to
 806 obtain the net out-flux from each element. We consider the first row of \mathbf{D} as an exam-
 807 ple, relevant for element 1. The only connection that contributes to the net out-flux of
 808 element 1 is connection 1 with the positive direction of $2 \rightarrow 1$, the opposite to the out-
 809 flux direction. Thus, $D(1, 1) = -1$ and other entries of the first row are zeros. How-
 810 ever, for element 2, the positive flux of connection 1 aligns with the outflux direction,
 811 which leads to $D(2, 1) = 1$. Similarly, other entries of matrix \mathbf{D} can be determined and
 812 the matrix \mathbf{D} is:

$$\mathbf{D} = \begin{bmatrix} -1 & 0 & 0 & 0 & 0 \\ 1 & -1 & -1 & -1 & 0 \\ 0 & 1 & 0 & 0 & 0 \\ 0 & 0 & 1 & 0 & -1 \\ 0 & 0 & 0 & 1 & 1 \end{bmatrix}. \quad (\text{A1})$$

813 We now proceed to construct the matrix \mathbf{T} , which computes the flux on each active con-
 814 nection from the pressure on each cell. Note that we only store the flux in the positive
 815 direction. For instance, the flux on the first connection is $Q_{2 \rightarrow 1} = T_{21} (p_2 - p_1)$, which
 816 means $T(1, 2) = -T(1, 1) = T_{21}$. Similarly, other entries of the matrix \mathbf{T} can be com-
 817 puted and the full expression of \mathbf{T} is:

$$\mathbf{T} = \begin{bmatrix} -T_{21} & T_{21} & 0 & 0 & 0 \\ 0 & -T_{32} & T_{32} & 0 & 0 \\ 0 & -T_{42} & 0 & T_{42} & 0 \\ 0 & -T_{52} & 0 & 0 & T_{52} \\ 0 & 0 & 0 & -T_{54} & T_{54} \end{bmatrix}. \quad (\text{A2})$$

818 **Appendix B Resonant frequencies from time domain results by GFEM**

819 In this section, we explain the procedure to obtain selective resonant frequencies
 820 from the time domain simulation results using the GFEM code developed by Shauer et
 821 al. (2021). As shown in Figure B1, we apply injection sources with a gaussian source time
 822 function on the certain position on the crack (red stars), obtain the pressure time series
 823 (duration of 50 s) on three receiving points (blue triangles), and then extract the res-
 824 onant frequencies at spectral peaks. For the rectangular crack, we place one source at
 825 the upperleft corner, which manages to excite all the first eight modes, and three receivers
 826 (R1, R2, and R3) at $(-0.5, 0)$, $(-0.20, 0.25)$, and $(0, 0.25)$, respectively. Different receivers
 827 sample different eigenmodes. For instance, receiver R1 samples modes 1, 2, 5, and 8 as
 828 shown in Figure B1-c. The modes sampled by R2 and R3 are shown in Table 2. We make
 829 this choice to selectively sample closely-spaced modes, for instance mode 2 and 3, at dif-
 830 ferent receivers to avoid ambiguity.

831 For the elliptical crack, we place two sources at the leftmost and uppermost ends,
 832 and three receivers at $(-0.5, 0)$, $(0, 0.25)$, $(0, 0)$ respectively. Due to the excitation and
 833 monitoring geometry, we focus only sampling the longitudinal and transverse modes, which
 834 are clearly seperated peaks in the spectrum. The eigenmodes sampled by different re-
 835 ceivers are shown in Figure B1-f and Table 3.

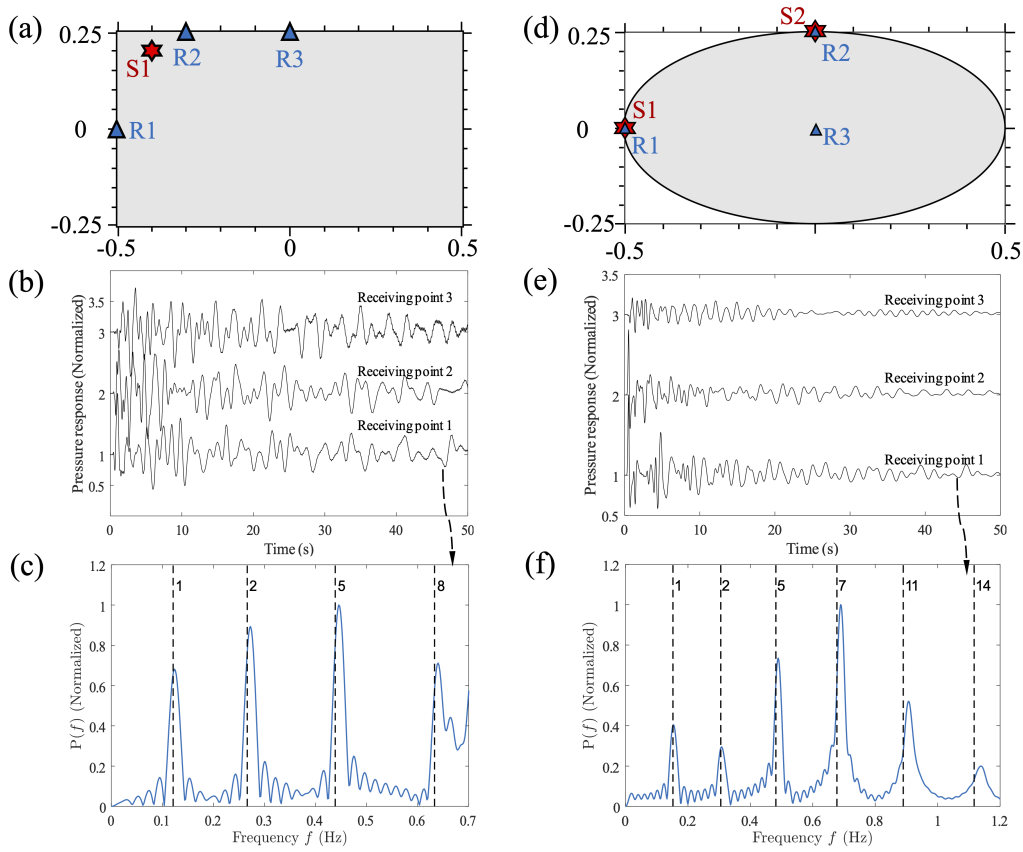


Figure B1. (a, d) The source and receiver positions. (b, e) Pressure time series at three receivers. (c, f) The normalized spectral amplitude of data at receiver R1. The vertical black dashed lines are the resonant frequencies (with mode number labelled) computed by BEM+FVM method.